

2000

Finite element modeling of current perturbation method of nondestructive evaluation application

Sunho Yang
Iowa State University

Follow this and additional works at: <https://lib.dr.iastate.edu/rtd>

 Part of the [Electrical and Electronics Commons](#)

Recommended Citation

Yang, Sunho, "Finite element modeling of current perturbation method of nondestructive evaluation application " (2000).
Retrospective Theses and Dissertations. 12666.
<https://lib.dr.iastate.edu/rtd/12666>

This Dissertation is brought to you for free and open access by the Iowa State University Capstones, Theses and Dissertations at Iowa State University Digital Repository. It has been accepted for inclusion in Retrospective Theses and Dissertations by an authorized administrator of Iowa State University Digital Repository. For more information, please contact digirep@iastate.edu.

INFORMATION TO USERS

This manuscript has been reproduced from the microfilm master. UMI films the text directly from the original or copy submitted. Thus, some thesis and dissertation copies are in typewriter face, while others may be from any type of computer printer.

The quality of this reproduction is dependent upon the quality of the copy submitted. Broken or indistinct print, colored or poor quality illustrations and photographs, print bleedthrough, substandard margins, and improper alignment can adversely affect reproduction.

In the unlikely event that the author did not send UMI a complete manuscript and there are missing pages, these will be noted. Also, if unauthorized copyright material had to be removed, a note will indicate the deletion.

Oversize materials (e.g., maps, drawings, charts) are reproduced by sectioning the original, beginning at the upper left-hand corner and continuing from left to right in equal sections with small overlaps.

Photographs included in the original manuscript have been reproduced xerographically in this copy. Higher quality 6" x 9" black and white photographic prints are available for any photographs or illustrations appearing in this copy for an additional charge. Contact UMI directly to order.

**Bell & Howell Information and Learning
300 North Zeeb Road, Ann Arbor, MI 48106-1346 USA
800-521-0600**

UMI[®]

**Finite element modeling of current perturbation method of nondestructive evaluation
application**

by

Sunho Yang

**A dissertation submitted to the graduate faculty
in partial fulfillment of the requirements for the degree of
DOCTOR OF PHILOSOPHY**

Major: Electrical Engineering (Electromagnetics)

Major Professors: Lalita Udpa and William Lord

Iowa State University

Ames, Iowa

2000

Copyright © Sunho Yang, 2000. All rights reserved.

UMI Number: 9962859

**Copyright 2000 by
Yang, Sunho**

All rights reserved.

UMI[®]

UMI Microform 9962859

Copyright 2000 by Bell & Howell Information and Learning Company.

**All rights reserved. This microform edition is protected against
unauthorized copying under Title 17, United States Code.**

**Bell & Howell Information and Learning Company
300 North Zeeb Road
P.O. Box 1346
Ann Arbor, MI 48106-1346**

Graduate College
Iowa State University

This is to certify that the Doctoral dissertation of

Sunho Yang

has met the dissertation requirements of Iowa State University

Signature was redacted for privacy.

Committee Member

Signature was redacted for privacy.

Committee Member

Signature was redacted for privacy.

Committee Member

Signature was redacted for privacy.

Committee Member

Signature was redacted for privacy.

Co-major Professor

Signature was redacted for privacy.

Co-major Professor

Signature was redacted for privacy.

For the Major Program

Signature was redacted for privacy.

For the Graduate College

TABLE OF CONTENTS

| | |
|---|------------|
| LIST OF FIGURES | vi |
| LIST OF TABLES | vii |
| ABSTRACT..... | ix |
| CHPATER I. INTRODUCTION..... | 1 |
| 1.1 Stress Corrosion Cracking | 2 |
| 1.2 Magnetic Flux Leakage (MFL) method..... | 2 |
| 1.3 Problem Statement..... | 7 |
| 1.2 Scope of the Dissertation | 12 |
| | |
| CHAPTER II. 2D AXISYMMETRIC MODEL | 13 |
| 2.1 Geometry..... | 13 |
| 2.2 Governing Equation..... | 13 |
| 2.3. Finite Element Formulation | 15 |
| 2.4. Numerical Results..... | 17 |
| | |
| CHAPTER III. VELOCITY EFFECTS AND MATERIAL NONLINEARTY | 23 |
| 3.1. Velocity Effect Anaysis | 24 |
| 3.1.1. Fields Transformation | 24 |
| 3.1.2. Governing Equation | 30 |
| 3.1.2. Transient Analysis..... | 31 |
| 3.2. Nonlinear Analysis | 34 |
| | |
| CHAPTER IV. MODELING OF CURRENT PERTURBATION METHOD | 43 |
| 4.1. Introduction..... | 43 |
| 4.2. Single Layer Source Model..... | 46 |

| | |
|---|------------|
| 4.2.1. Step 1. Calculation of Velocity Induced Currents | 46 |
| 4.2.2. Step 2. Calculation of Perturbation Current by SCC | 49 |
| 4.2.3. Step 3. Calculation of Current Perturbation Fields | 51 |
| 4.2.4. Step 4. Measurement of perturbation fields using a coil..... | 54 |
| 4.3. Double Layer Source Model | 54 |
| 4.3.1. Single Layer Charge Distribution | 55 |
| 4.3.2. Double Layer Charge Distribution..... | 57 |
| 4.3.3. Application of Double Layer Source Model to SCC in Pipe..... | 60 |
| 4.4. Substructure Method..... | 63 |
| CHAPTER V. RESULTS AND DISSCUSSION..... | 67 |
| 5.1. Single Layer Source Model..... | 67 |
| 5.1.1. Single SCC | 67 |
| 5.1.2. Multiple SCC by Superposition Method | 77 |
| 5.2. Double Layer Source Model | 82 |
| CHAPTER VI. CONCLUSIONS | 96 |
| 6.1. Summary of Accomplishments | 96 |
| 6.2. Future Work | 97 |
| APPENDIX. FINITE ELEMENT FORMULATION OF STEP 2..... | 99 |
| BIBLIOGRAPHY | 107 |
| ACKNOWLEDGMENTS..... | 111 |

LIST OF FIGURES

| | |
|---|----|
| Figure 1.1. Incidents related to natural gas pipeline | 1 |
| Figure 1.2. Example of stress corrosion crack colony | 3 |
| Figure 1.3. Steel billet bar with defect | 5 |
| Figure 1.4. Magnetic characteristic of billet bar | 5 |
| Figure 1.5. Dipole model..... | 6 |
| Figure 1.6. Schematic of pig and flux distribution in the pipe wall..... | 8 |
| Figure 1.7. Magnetic flux due to rotated single magnet..... | 9 |
| Figure 1.8. Motion-induced current | 10 |
| Figure 2.1. Cross section of typical MFL inspection tool..... | 13 |
| Figure 2.2. Detailed pig geometry..... | 18 |
| Figure 2.3. Example of mesh discretization with rectangular elements..... | 19 |
| Figure 2.4. Mesh discretization around the pig..... | 20 |
| Figure 2.5. Contour plot of flux lines with 8 cm long and 80% depth defect | 21 |
| Figure 2.6. Flux density plot of 8 cm long and 80% depth defect | 22 |
| Figure 3.1. Current induction process due to interaction of magnetizer and velocity | 23 |
| Figure 3.2. Two inertial coordinate system in relative motion..... | 26 |
| Figure 3.3. Example of 1D movement with a constant velocity..... | 29 |
| Figure 3.4. Velocity effect on the flux line..... | 35 |
| Figure 3.5. Induce current in the pipewall at velocity..... | 36 |
| Figure 3.6. MFL signal with velocity..... | 37 |

| | |
|--|----|
| Figure 3.7. B-H characteristic of pipewall | 38 |
| Figure 3.8. Operating point on the B-H curve | 39 |
| Figure 3.9. Flow chart of overall nonlinear procedure with time stepping | 41 |
| Figure 3.10. Current density plot in pipe-wall..... | 42 |
| Figure 4.1. Tight crack | 44 |
| Figure 4.2. Current decomposition..... | 45 |
| Figure 4.3. Geometry of step 1 | 47 |
| Figure 4.4. Motion induced current distribution in the pipe wall | 48 |
| Figure 4.5. Geometry of step 2 | 50 |
| Figure 4.6. Step 2 results, perturbation current..... | 52 |
| Figure 4.7. Fields of step 3 | 53 |
| Figure 4.8. Example of SCC colony | 55 |
| Figure 4.9. Field discontinuities along the single layer source..... | 56 |
| Figure 4.10. Double layer source distribution | 57 |
| Figure 4.11. Solid angle..... | 58 |
| Figure 4.12. Discontinuity of E_t around a double layer source..... | 59 |
| Figure 4.13. Double layer source model | 61 |
| Figure 4.14. Step 2 results using double layer source model | 62 |
| Figure 4.15. Sub-region Ω_I and Ω_{II} | 65 |
| Figure 5.1. Flow chart of four-step procedure | 68 |
| Figure 5.2. Geometry used for four-step procedure | 69 |
| Figure 5.3. Induced voltage measured for defects of different depths..... | 72 |

| | |
|---|----|
| Figure 5.4. Peak to peak value of induced voltage as a function of defect depths | 72 |
| Figure 5.5. Induced voltage measured for defects of different lengths (60% depth)..... | 73 |
| Figure 5.6. Peak to peak value of induced voltage as a function of defect lengths (60% depth) | 73 |
| Figure 5.7. Induced voltage measured at different circumferential coil position (60% depth) | 74 |
| Figure 5.8. Peak to peak value of induced voltage as a function of different coil position (60% depth) | 74 |
| Figure 5.9. Peak to peak value of induced voltage as a function of different axial coil Position (8 cm length, 60% depth)..... | 75 |
| Figure 5.10. Peak to peak value of induced voltage as a function of defect depth with velocity (3 m/s and 5 m/s) | 76 |
| Figure 5.11. Peak to peak value of induced voltage as a function of different circumferential coil position with velocity (3 m/s and 5 m/s)..... | 76 |
| Figure 5.12. Signal due to two parallel defects as a function of circumferential distance (8 cm long, 80% depth) | 79 |
| Figure 5.13. Signal due to two parallel defects with distance of both circumferential and axial (8 cm long, 80 % depth) | 79 |
| Figure 5.14. Case 1 defect profile and resulting signal | 80 |
| Figure 5.15. Case 2 defect profile and resulting signal | 81 |
| Figure 5.16. Case 3 defect profile and resulting signal | 82 |
| Figure 5.17. Comparison of symmetric model and double layer source model | 84 |
| Figure 5.18. Angle θ between the normal direction n to the parallel defect and normal direction n' to the angular defect | 85 |
| Figure 5.19. Mesh for angular defect | 85 |
| Figure 5.20. Induced voltage for parallel and angular defect | 86 |
| Figure 5.21. Induced voltage signals as a function of different angles | 86 |

| | |
|--|-----------|
| Figure 5.22. Comparison between superposition model and double layer source model with different circumferential distance | 88 |
| Figure 5.23. Mutual interaction effect between two parallel cracks | 89 |
| Figure 5.24. Case 1 defect profile and induced voltage signal | 92 |
| Figure 5.25. Case 2 defect profile and induced voltage signal | 93 |
| Figure 5.26. Case 3 defect profile and induced voltage signal | 94 |
| Figure 5.27. Case 4 defect profile and induced voltage signal | 95 |
| Figure 6.1. Defect under the fastener | 98 |

LIST OF TABLES

Table 5.1. Defect profile for each case of the superposition model..... 78

Table 5.1. Defect profile for each case of the double layer source model 91

ABSTRACT

Magnetic flux leakage (MFL) methods are used widely in the nondestructive evaluation (NDE) of natural gas transmission pipelines. In this technique, the pipe wall is magnetized in the axial direction and a circumferential array of Hall sensors is used to detect any leakage flux caused by the presence of defects in the pipe wall. In general, this tool generates an axially oriented magnetic field, which is sensitive to the presence of circumferential cracks. However, these inspection tools are insensitive to stress corrosion cracking (SCC) which are oriented largely in the axial direction.

A possible solution to this problem is to utilize the fields associated with the circumferential currents generated in the pipe-wall by the movement of the magnetizer relative to the pipe-wall. Since the motion of the tool inside the pipe is along the pipe axis, the motional emf due to the $\vec{v} \times \vec{B}$ term is negligible between the poles of the magnet. However, at the poles, the radially oriented magnetic fields generate a significant amount of circumferentially directed currents. The intersection of these motion-induced currents with the axial SCC results in a perturbation of the current distribution. The fields associated with the perturbation currents carry information relating to the presence of axial SCC.

The finite element modeling of the interaction between axial stress corrosion cracks and circumferential currents is a significant challenge in terms of both the computation time and memory requirements. The challenges arise due to the nonlinearity of material properties, the size of tight cracks relative to that of the magnetizer, and the time stepping involved in modeling velocity effects. An approach is presented to avoid these problems by

decomposing the overall task into four simpler subtasks that can be performed sequentially. The simulation results demonstrate the feasibility of detection of both single and symmetric SCC and SCC colonies of arbitrary orientation.

CHAPTER I. INTRODUCTION

Natural gas is transported to customer locations through a vast network of pipelines totaling over a million miles [1]. The development of NDE technology to ensure pipeline integrity is necessary for the safe and reliable operation of the pipelines [2]. Several causes of pipeline failures are shown in figure 1.1. The most recent concern in gas pipeline inspection is the detection and characterization of stress corrosion cracking (SCC). The first recognized case of pipeline stress corrosion cracking was recorded in 1965. Since then, much has been learned about the nature of SCC [3].

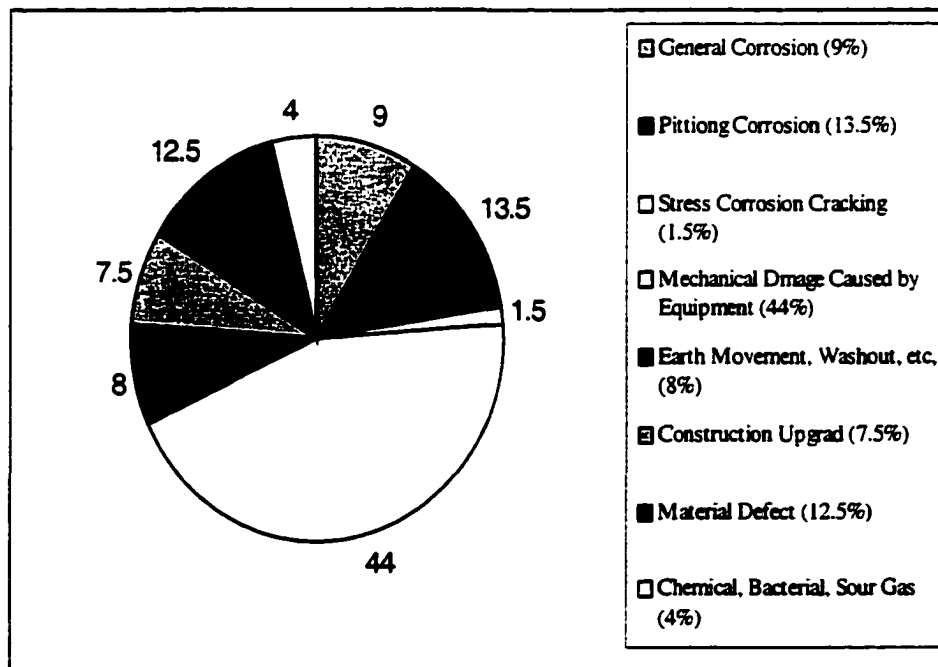


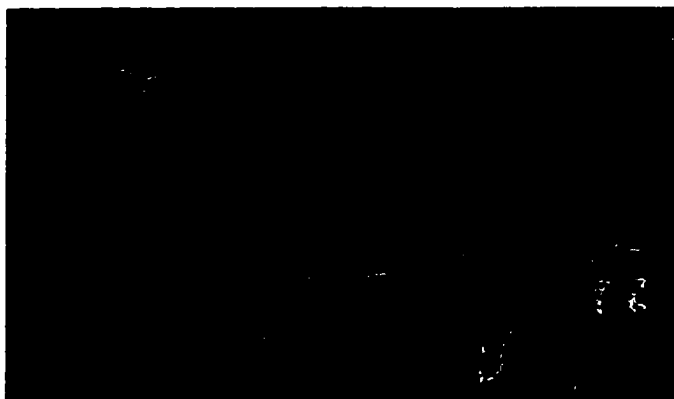
Figure 1.1. Incidents related to natural gas pipeline

1.1. Stress Corrosion Cracking

Stress corrosion cracking is a complex phenomenon that has caused several service and hydrostatic retest failures in gas and liquid pipelines [4]. SCC occurs at isolated locations and when a limited set of conditions is met. The exact mechanisms that lead to SCC and operating conditions that affect cracking are the subject of ongoing research. SCC results from the combined action of stress, a cracking environment, and temperature that causes cracks to initiate and grow in pipe steel. Individual cracks are generally oriented perpendicular to the maximum stress and parallel to the pipe axis. Groups of cracks usually occur in what is known as a “colony”. In extreme cases, these colonies may be several feet long and extend nearly around the circumference. An SCC colony is considered sparse if the cracks are far apart in the circumferential direction and dense if the cracks are circumferentially close together as shown in figure 1.2. Individual cracks can range in depth from “shallow” to “deep”. Many of the cracks in the middle of dense colonies have a depth less than ten percent of the wall thickness. In sparse colonies and in some dense colonies, the cracks can grow in a stable manner until they reach a depth that is nearly through the wall. The detection of these deeper cracks is of primary concern in inspections for evaluating pipeline integrity.

1.2. Magnetic Flux Leakage (MFL) method

MFL methods are used widely in the nondestructive evaluation (NDE) of natural gas transmission pipeline. When a ferromagnetic material is magnetized using a permanent magnet or current the presence of a defect in the magnetized ferromagnetic material results in



(a)



(b)

Figure 1.2. Example of stress corrosion crack colony, (a) sparse (b) dense [4]

a redistribution of the flux line in the vicinity, causing some of the flux lines to leak out into the surrounding medium [5][6]. The magnetic flux leakage NDE method is based on the detection of the leakage flux around the defect. The flux leakage phenomena can be explained by the change of permeability μ , and magnetic flux density \vec{B} in the presence of a defect. Consider a steel billet bar with a surface defect as shown in figure 1.3. Let the cross sectional area of the billet be A and the cross sectional area of the defect be 'a' so that the cross-sectional area of the billet with defect is $A'=A-a$. Suppose the billet is placed in a magnetizing field \vec{H} , and B_1 is the induced flux density in the bar at X shown in figure 1.3. The corresponding operating points are represented by P_1 and Q_1 respectively on the permeability and normal induction curve shown in 1.4. The total flux passing through the bar is given by B_1A . If a defect is now introduced in the cross-sectional area, the induced flux density at X is $B_2=B_1 (A/A')$ which is greater than the B_1 . Correspondingly the operating point Q_1 moves to Q_2 on the normal induction curve and P_1 moves to P_2 on the permeability curve. This results in conflicting demands in the vicinity of the defect. The increase of induced flux in the vicinity of the defect drives the permeability in the vicinity of the defect to a value less than that in the defect free area. Since flux lines follow the path of least reluctance, some of the flux leaks into the surrounding medium.

One of the first theoretical studies for calculation of the magnetic flux leakage fields was presented by Zatsepin and Schcherbinin [8] [9]. They modeled the defect surface by a distribution of magnetic dipoles and calculated the dipole magnetic field. The rectangular slot is modeled by the following assumptions. First, they assume that magnetic charges are uniformly distributed over the sides of the slots and the charge on the base of the slot does

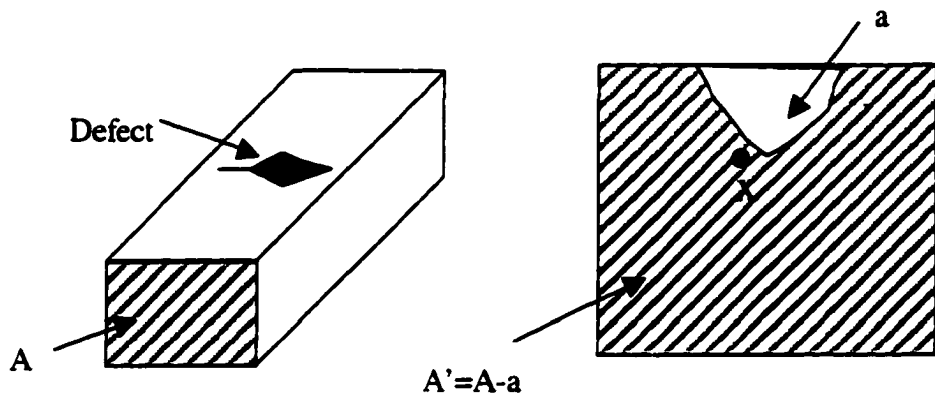


Figure 1.3. Steel billet bar with defect [7]

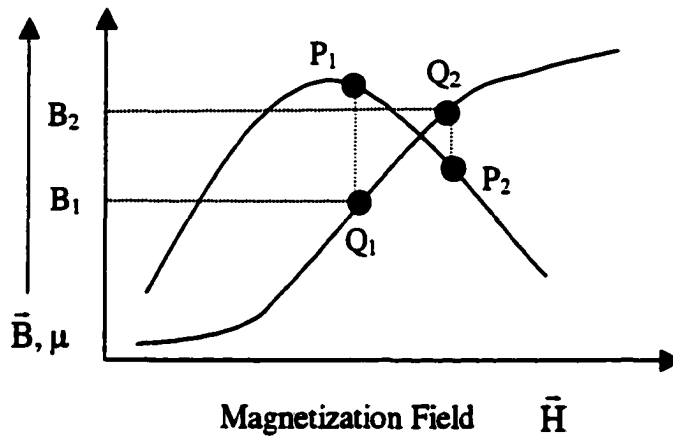


Figure 1.4. Magnetic characteristic of billet bar [7]

affect the leakage field. Using the above assumption, expressions were obtained for the normal and tangential components of the magnetic leakage fields due to an artificial rectangular slot as shown in figure 1.5.

$$H_x = 2\sigma_s \left[\operatorname{arctg} \frac{h(x+b)}{(x+b)^2 + y(y+h)} - \operatorname{arctg} \frac{h(x-b)}{(x-b)^2 + y(y+h)} \right]$$

$$H_y = \sigma_s \ln \frac{[(x+b)^2 + (y+h)^2][(x-b)^2 + y^2]}{[(x+b)^2 + y^2][(x-b)^2 + (y+h)^2]}$$

where σ_s is the linear density of magnetic charge. Subsequent papers [10] [11] based on the dipole method present the improvements in the model in terms of reducing the edge effect. In this model, they consider the charges are distributed not only on the edges of the flaw but also at the surface of component adjacent to the flaw. Although this approach approximates the leakage fields fairly well, it is limited to very simple and restricted geometries.

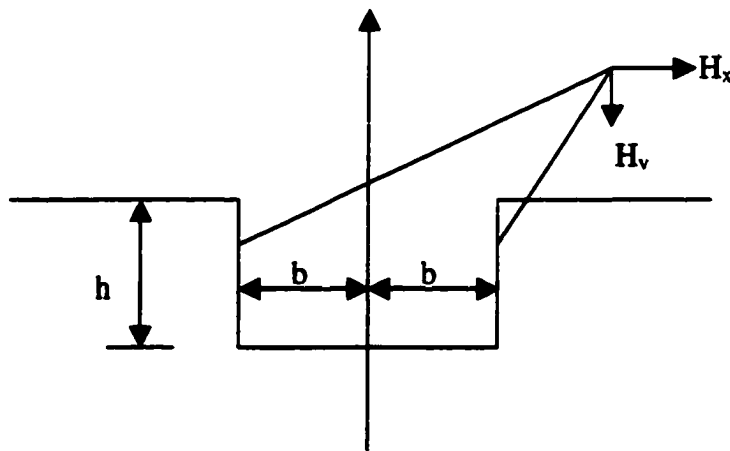


Figure 1.5. Dipole model

Significant progress in the calculation of leakage field was made by Hwang and Lord [12] using numerical methods based on finite element analysis showing the feasibility of the finite element method for defect detection and characterization. The application of the work is extended in [13][14], where the finite element method is applied to a variety of complicated defect shapes. Currently finite element methods are the most widely used numerical technique for solving many engineering problems including NDE.

1.3. Problem Statement

A schematic of the MFL inspection tool for the pipeline inspection, referred to as the pig, is shown in figure 1.6. The pig consists of three major parts, namely the magnetic circuit, the hall sensor array and data acquisition system [15]. The magnetic circuit consists of magnet assembly, backing iron and brushes. The permanent magnet magnetizes the pipewall between the brushes in the axial direction. In the presence of an outside diameter (OD) defect, the magnetic fields near the defect are redistributed and some magnetic fields leak out as shown in figure 1.6. The circumferential array of hall sensors is used to detect the flux leakage caused by the presence of the defect.

In general, the conventional MFL tool generates an axially oriented magnetic field, which is sensitive to the presence of circumferential cracks. However, these inspection tools are insensitive to stress corrosion cracks which are oriented largely in the axial direction. The detection of SCC in this incipient stage, therefore remains a major challenge to pipeline inspection companies.

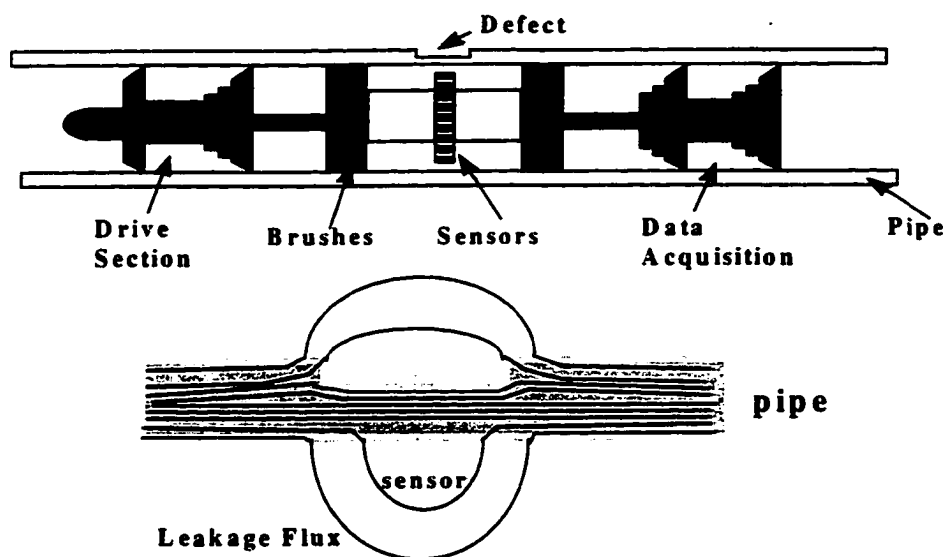


Figure 1.6. Schematic of pig and flux distribution in the pipe wall

A simple solution for addressing this problem is to rotate the magnet as shown in figure 1.7. In this case, the magnet generates a circumferentially oriented flux that will be sensitive to axially oriented SCC. However, with a single magnet, defects positioned at the points A or B cannot be detected.

One of the possible solutions to this problem is to generate a rotating magnetic field. The application of rotating magnetic field for detection of the axially oriented SCC in the pipe-wall is shown in [16]. The rotor placed in the pipe is excited to generate circumferentially oriented rotating magnetic fields in the pipe-wall. The interaction of rotating oriented defect results in perturbation of the magnetic field. Experimental and numerical results presented in [16][17] show the feasibility of the method.

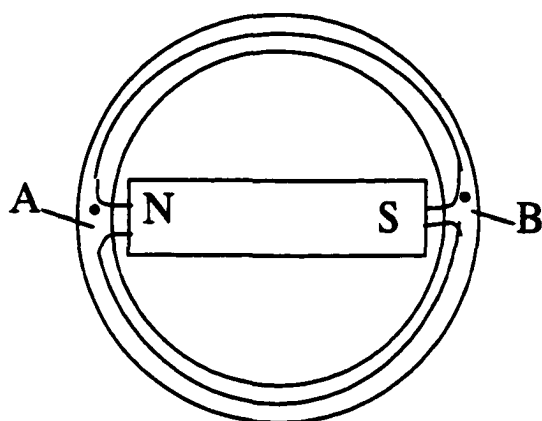


Figure 1.7. Magnetic flux due to rotated single magnet

The rotor is excited by a three phase power supply at frequency 40 Hz. The sensor coil with 10,000 turn with a dimension of 2x1x0.5 cm was used for measuring the magnetic flux density. However, this method needs a new tool design.

An alternate solution to the problem is to augment the existing procedure by examining alternate information sources available in the pig. For instance, the motion of permanent magnets relative to the pipewall generates an emf in the pipewall given in magnitude and direction by $\vec{v} \times \vec{B}$, where \vec{v} is the velocity of motion and \vec{B} is flux density [18] [19]. This motional emf generates large amount of currents in the pipewall. Since the motion of the tool inside the pipe is along the pipe axis, the motional emf due to the $\vec{v} \times \vec{B}$ term is negligible between the poles of the magnet. However, at the poles, the radially oriented magnetic fields generate a significant amount of circumferentially currents that decay away from the poles. The interaction of these motion-induced currents with axial SCC

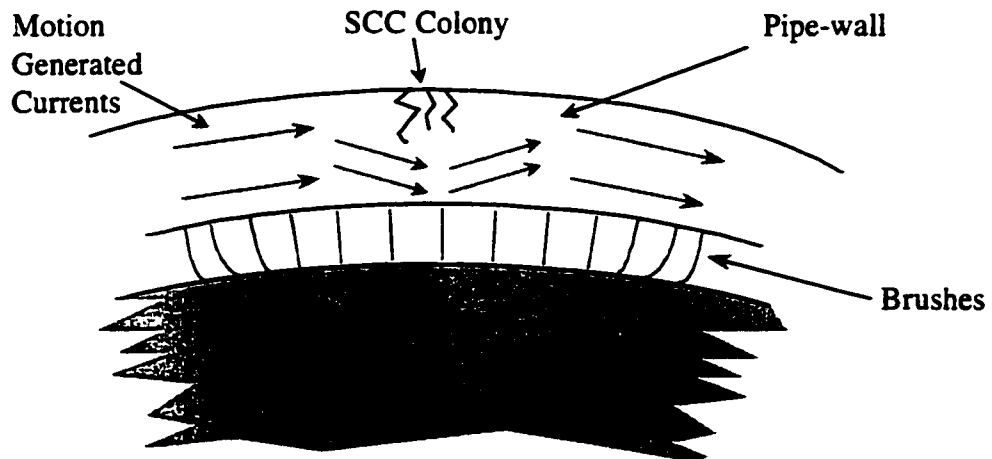


Figure 1.8. Motion-induced current

colonies results in a perturbation of the current distribution as shown schematically in figure 1.8. The fields associated with the perturbation currents carry information relating to the presence of axial SCC.

This dissertation investigates the feasibility of this idea by developing a FE model to simulate this phenomenon. To model a realistic SCC and simulate the motion-generated current in the pipewall and the current perturbation fields by the SCC, a full 3D numerical modeling is needed. The 3D modeling, however, is a significant challenge due to nonlinearity of material properties, the size of tight cracks relative to that of a magnetizer, and also the time stepping involved in modeling velocity effects. Due to these problems, the development of a full 3D model is very difficult even with the current state-of-art computer hardware and software.

Atherton and Mergelas [20] present an approach for studying the interaction between defects and eddy currents in which the defect is modeled by a combination of surface solenoidal currents and current loops at the edges on the surface. Chen and Miya [21] proposed the ring current model for describing eddy current perturbation due to a crack. The crack opening is represented by two sets of ring currents. Huang, et al [22] have used the dipole current model to solve forward and inverse problems in eddy current NDT.

The method proposed in this thesis presents a quantitative description of a tight crack in terms of perturbation currents derived from the velocity induced circumferential currents obtained in a defect free pipe. The approach used decomposes the overall task into four simpler subtasks that can be performed sequentially. In this procedure, we assume that the perturbation effect due to a defect is limited to a small region around the defect. This helps reduce the region of interest that needs to be modeled. Second, the region of interest is assumed to be in remote area from exciter and hence we can assume linearity. This also allows use of the superposition principle, where we can divide the total current into (i) background current (J_0) which is the circumferential current due to the $\vec{v} \times \vec{B}$ effect in the absence of defect and (ii) perturbation current (\vec{J}_p) due to the introduction of an SCC.

The underlying concepts of the four-step procedure can be summarized as follows:

Step 1: The velocity induced currents \vec{J}_0 in a defect-free pipe wall due to axial motion of the magnetizer relative to the pipe are calculated.

Step 2: Assuming that the defect is nonconducting, the tight crack is modeled by applying a current $-\vec{J}_0$ at the nodes i defining the SCC. The total perturbation current \vec{J}_p is then computed.

Step 3: The results obtained in step 2 are used to solve for the perturbation fields

Step 4: Measure the perturbation fields using a simple induction coil

1.4 Scope of the Dissertation

Chapter II presents the geometry and governing equation for the axisymmetric formulation of an MFL non-destructive evaluation method for the gas pipeline inspection. Velocity effect analysis and nonlinearity of the material property are discussed in chapter III. In chapter VI, the procedure for the numerical modeling of interaction between the axial oriented SCC and the motion-generated circumferential currents is presented. For modeling of the SCC colonies, a simple superposition method and double layer source model are described. Substructure method is utilized for reducing the computational complexity. Chapter V shows the numerical results due to a single SCC and SCC colonies. Parametric studies are conducted for the different defect parameters (length and depth) and different sensor positions (axial and circumferential). Chapter VI presents conclusions and direction of future works.

CHAPTER II. 2D AXISYMMETRIC MODEL

2.1. Geometry

Conventional MFL technique for gas pipeline inspection uses the inspection tool called “pig”. The pig consists of three major parts, namely a magnetic circuit, a hall sensor array and a data acquisition system. The magnetic circuit consists of magnet assembly, backing iron and brushes. The cross section of a pig is shown in figure 2.1. Detailed descriptions of the pig are given in [15].

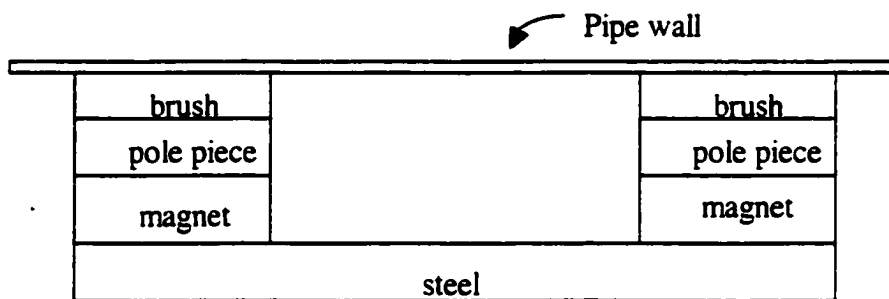


Figure 2.1. Cross section of typical MFL inspection tool

2.2 Governing Equation

The governing equations describing the MFL phenomena begin with the differential equation of Ampere’s law

$$\nabla \times \vec{H} = \vec{J} \quad (2.1)$$

where, \vec{H} is magnetic field intensity and \vec{J} is source current density. The vector magnetic potential \vec{A} is defined by

$$\nabla \times \vec{A} = \vec{B} \quad (2.2)$$

where, \vec{B} is magnetic flux density. For a homogeneous and isotropic ferromagnetic material, the magnetic flux density \vec{B} is related to magnetic field intensity by

$$\vec{B} = \mu \vec{H} \quad (2.3)$$

where μ is the permeability of the material. Substituting equations (2.2) and (2.3) into (2.1) gives the governing partial differential equation.

$$\nabla \times \frac{1}{\mu} \nabla \times \vec{A} = \vec{J} \quad (2.4)$$

This, however, does not determine \vec{A} uniquely, because if \vec{A} is a solution to equation (2.4), any function that can be written as $\vec{A}' = \vec{A} + \nabla f$ is also a solution regardless of the form of f . Hence, to determine \vec{A} uniquely, a gauge condition equation (2.5) should be imposed on its divergence. In this thesis, the Coulombs gauge is used and defined as

$$\nabla \cdot \vec{A} = 0 \quad (2.5)$$

By using the vector identity

$$\nabla \times \nabla \times \vec{A} = \nabla(\nabla \cdot \vec{A}) - \nabla^2 \vec{A} \quad (2.6)$$

and assuming μ to be constant, equations (2.4), (2.5) and (2.6) yields the vector Poisson equation.

$$\nabla^2 \vec{A} = -\mu \vec{J} \quad (2.7)$$

In the case of axisymmetric geometry, the cylindrical coordinate system (r, ϕ, z) is used where r is radial direction, ϕ is circumferential direction and z is axial direction and equation (2.7) reduces to

$$\frac{1}{\mu} \left[\frac{\partial}{\partial r} \left\{ \frac{1}{r} \frac{\partial}{\partial r} (rA) \right\} + \frac{\partial}{\partial z} \left(\frac{\partial A}{\partial z} \right) \right] = -J, \quad (2.8)$$

The magnetic vector potential A and source current J_s in axisymmetric case has only circumferential component ϕ and hence are treated as scalars.

2.3 Finite Element Formulation

Applying the weak formulation to equation (2.8) we can write

$$\int_V \delta A \left[\frac{1}{\mu} \frac{\partial}{\partial r} \left(\frac{1}{r} \frac{\partial}{\partial r} (rA) \right) + \frac{1}{\mu} \frac{\partial}{\partial z} \left(\frac{\partial A}{\partial z} \right) + J \right] dV = 0 \quad (2.9)$$

Integrating (2.9) by parts and invoking the identities

$$\frac{\partial}{\partial r} \left[\delta A \frac{1}{r} \frac{\partial rA}{\partial r} \right] = \frac{1}{r} \frac{\partial rA}{\partial r} \frac{\partial \delta A}{\partial r} + \delta A \frac{\partial}{\partial r} \left[\frac{1}{r} \frac{\partial rA}{\partial r} \right] \quad (2.10)$$

$$\frac{\partial}{\partial z} \left(\frac{\delta A}{r} \frac{\partial rA}{\partial z} \right) = \frac{\partial A}{\partial z} \frac{\partial \delta A}{\partial z} + \delta A \frac{\partial}{\partial z} \left(\frac{1}{r} \frac{\partial rA}{\partial z} \right) \quad (2.11)$$

then we obtain

$$\begin{aligned} & \int_V \frac{1}{\mu} \left[\frac{\partial}{\partial r} \left(\delta A \frac{1}{r} \frac{\partial}{\partial r} (rA) \right) + \frac{\partial}{\partial z} \left(\delta A \frac{1}{r} \frac{\partial}{\partial z} (rA) \right) \right] dV \\ & - \int_V \left[\frac{1}{\mu} \frac{1}{r} \frac{\partial}{\partial r} (rA) \frac{\partial \delta A}{\partial r} + \frac{1}{\mu} \frac{\partial A}{\partial z} \frac{\partial \delta A}{\partial z} - \delta A J \right] dV = 0 \end{aligned} \quad (2.12)$$

In order to apply the Green's theorem, we manipulate the equation (2.12) to get

$$\int_V \frac{1}{\mu} \left[\frac{\partial}{\partial r} \left(\delta A \frac{1}{r} \frac{\partial}{\partial r} (rA) \right) + \frac{1}{r} \left(\delta A \frac{1}{r} \frac{\partial}{\partial r} (rA) \right) + \frac{\partial}{\partial z} \left(\delta A \frac{1}{r} \frac{\partial}{\partial z} (rA) \right) \right] dV - \int_V \left[\frac{1}{\mu} \frac{1}{r} \frac{\partial}{\partial r} (rA) \frac{\partial \delta A}{\partial r} + \frac{1}{r} \left(\delta A \frac{1}{r} \frac{\partial}{\partial r} (rA) \right) + \frac{1}{\mu} \frac{\partial A}{\partial z} \frac{\partial \delta A}{\partial z} - \delta A J \right] dV = 0 \quad (2.13)$$

By applying Green's theorem, the first term becomes a surface integral and can be written in form

$$\oint_S \frac{1}{\mu} \delta A \left(\frac{1}{r} \frac{\partial}{\partial r} (rA) \mathbf{n}_r + \frac{\partial A}{\partial z} \mathbf{n}_z \right) dS = \oint_S \frac{1}{\mu} \delta A \frac{\partial A}{\partial n} dS \quad (2.14)$$

If the Dirichlet boundary condition is used, the value at the boundary is known, hence the variation δA is zero at the boundary nodes. If the Neumann boundary condition is known,

$\frac{\partial A}{\partial n}$ is zero. Using this result in equation (2.13) the integral equation reduces to

$$\int_V \left[\frac{1}{\mu} \frac{1}{r} \frac{\partial}{\partial r} (rA) \frac{\partial \delta A}{\partial r} + \frac{1}{r} \left(\delta A \frac{1}{r} \frac{\partial}{\partial r} (rA) \right) + \frac{1}{\mu} \frac{\partial A}{\partial z} \frac{\partial \delta A}{\partial z} - \delta A J \right] dV = 0 \quad (2.15)$$

If we arrange it as the elemental matrix form

$$\int_{V_e} \frac{1}{\mu} \left[\delta \left(\frac{\partial A}{\partial r} + \frac{A}{r} \right) \right] \left[\frac{\partial A}{\partial r} + \frac{A}{r} \right] dV - \int_{V_e} \delta A J dV = 0 \quad (2.16)$$

Using the nodal element approximation

$$A_e = \sum_{k=1}^{N_e} A_k N_k \quad (2.17)$$

where N_e is the node in each element, N_k is the shape function corresponding node k . Using the following notation

$$\nabla A_e = \begin{pmatrix} \frac{\partial A}{\partial r} + \frac{A}{r} \\ \frac{\partial A}{\partial z} \end{pmatrix} = \sum_k \begin{pmatrix} \frac{\partial}{\partial r} + \frac{1}{r} \\ \frac{\partial}{\partial z} \end{pmatrix} N_k A_k = (\nabla N)A \quad (2.18)$$

Substituting back in equation (2,16), we get

$$\int_{V_e} \delta A_e^T \left[\frac{1}{\mu} [\nabla N]^T [\nabla N] A_e - J [N]^T \right] dV = 0 \quad (2.19)$$

We can write elemental matrix equation as follow

$$[S]_e [A]_e = [Q]_e \quad (2.20)$$

where

$$[S]_e = \int_{V_e} \frac{1}{\mu} [\nabla N]^T [\nabla N] dV \quad (2.21)$$

$$[Q]_e = \int_{V_e} J [N]^T dV \quad (2.22)$$

2.4. Numerical Results

Axisymmetric formulation (2.19) is used to simulate the MFL technique to detect the defect. The cylindrical coordinate system (r – radial direction, ϕ - circumferential direction, and z – axial direction) with symmetry along ϕ is used. The detailed pig geometry is shown in figure 2.2. The pipe length is 2.515 m with thickness is 0.009 m. The reluctivity of the pipe is 15915 (m/H) and the conductivity is 6×10^6 (mho/m). In order to apply the finite element method, we first discretize the solution region into rectangular elements as shown in figure 2.2. The number of node is 77 x181 (r : 77, z : 181).

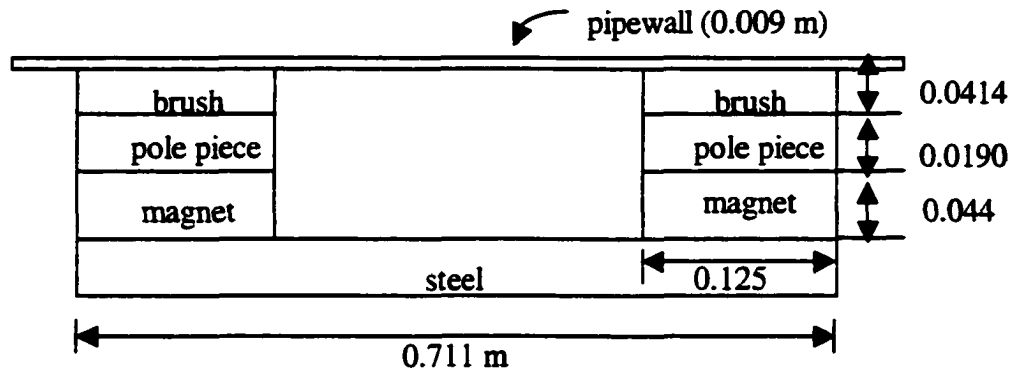


Figure 2.2. Detailed pig geometry

The length of the element size in the z-direction is 0.0191 m and varies in the r-direction. Figure 2.3 shows the mesh discretization corresponding to the geometry in figure 2.2. The defect is 8 cm in length and has a depth equal to 80% of the pipewall. Figure 2.4 shows the contour plot of the flux lines. We can clearly see from this figure that the flux line produced by magnetizer distort and leak out around the defect. Figure 2.5 shows the corresponding flux density plot (a) B_r – radial component (b) B_z – axial component, as a function of axial distance of the pig.

In the MFL inspection technique, the magnetizer moves at a high speed in the gas pipeline. At this high speed, the MFL signal distorted significantly. In the following chapter, the effect due to velocity of the pig is discussed.

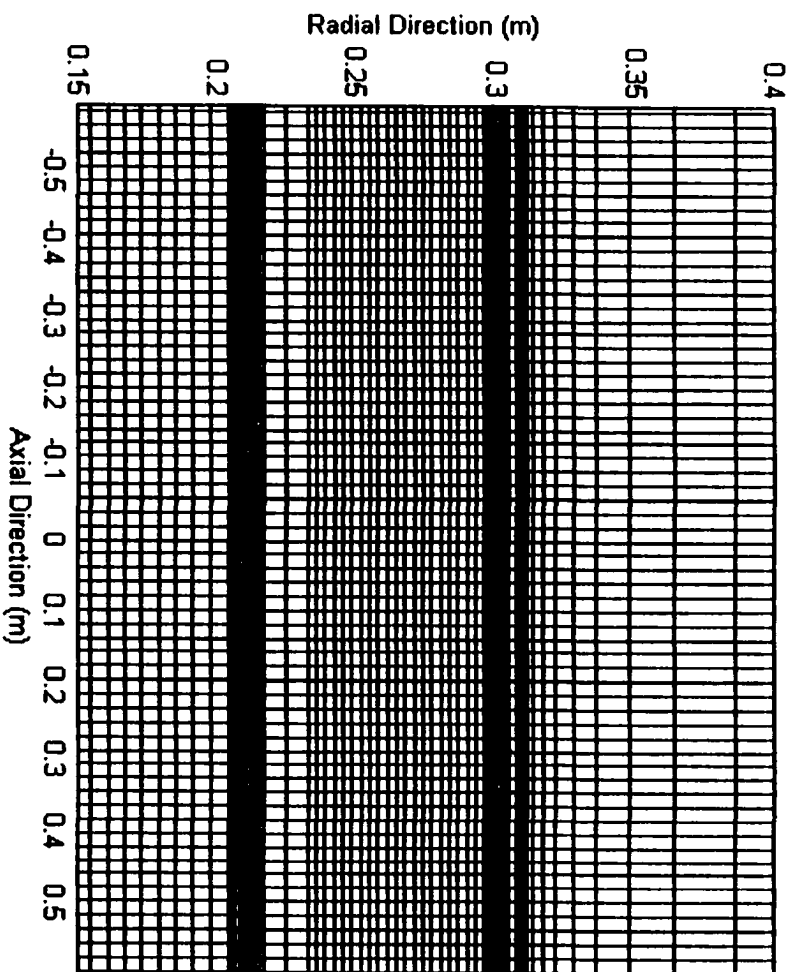


Figure 2.2. Example of mesh discretization with rectangular element

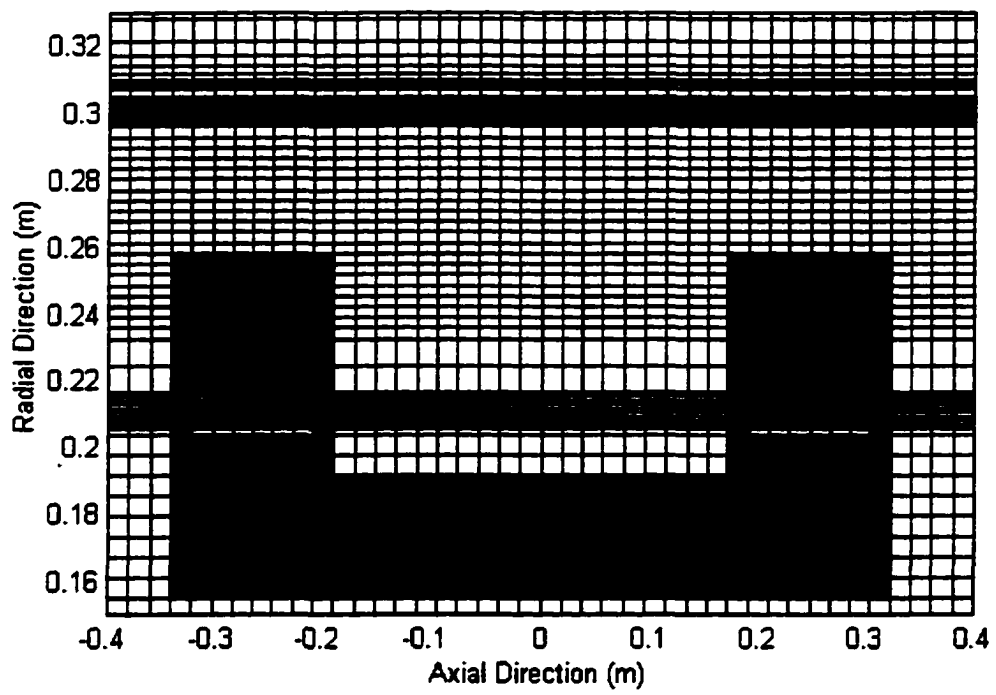


Figure 2.3. Mesh discretization around the pig

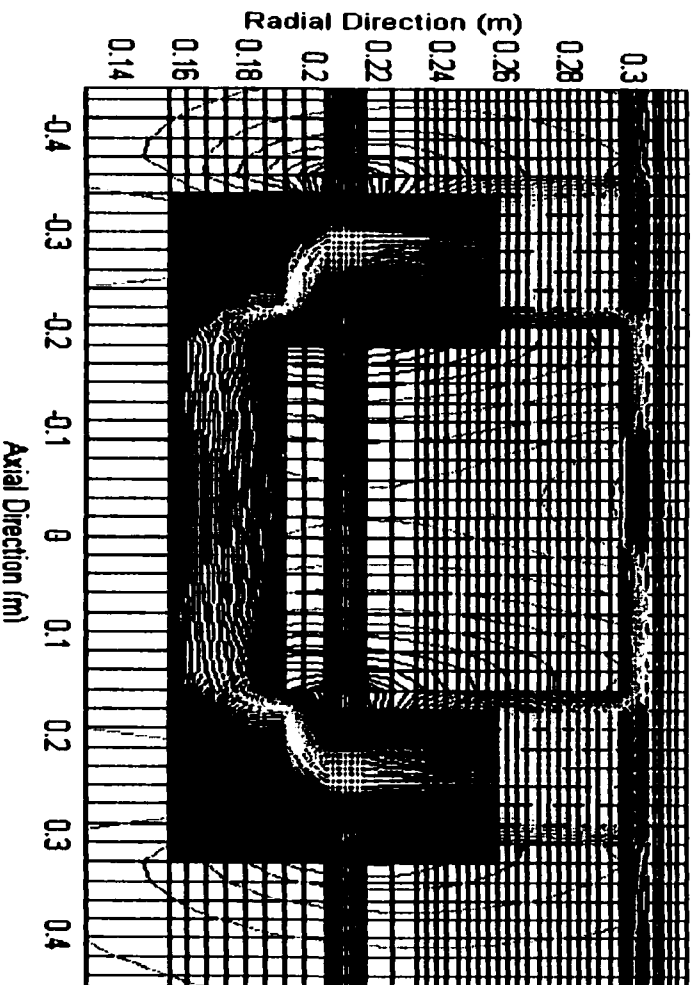
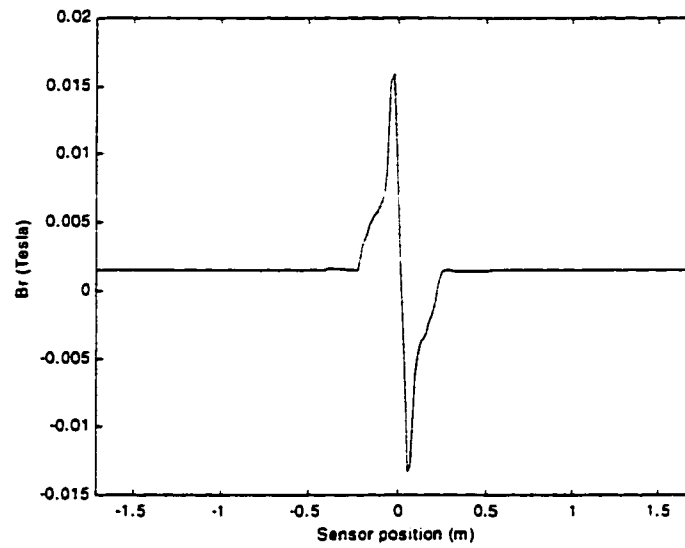
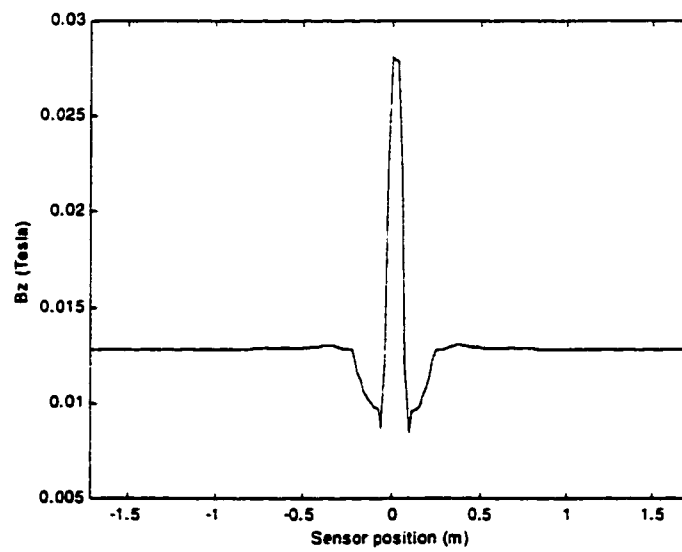


Figure 2.4. Contour plot of flux lines with 8 cm long and 80% depth defect



(a)



(b)

Figure 2.5. Flux density plot of 8 cm long and 80% depth defect (a) Radial component (B_r) (b) Axial component (B_z)

CHAPTER III. VELOCITY EFFECT AND MATERIAL NONLINEARTY

In a practical pipeline inspection, the MFL inspection tool moves in the pipe with velocities up to 25 m/s. At this high velocity, the leakage signal is significantly distorted due to motion-generated emf. The magnetizer velocity, \vec{v} , is along the pipe axis, the motional emf due to the $\vec{v} \times \vec{B}$ term is negligible between the poles of the magnet. However, at the poles, the radially oriented magnetic fields generate a significant amount of circumferentially directed currents. Figure 3.1. shows the schematic of the current induction process. Understanding the effects of velocity on the leakage field is very important in improving the accuracy and reliability of MFL inspections. A detailed mathematical formulation of this procedure is presented next.

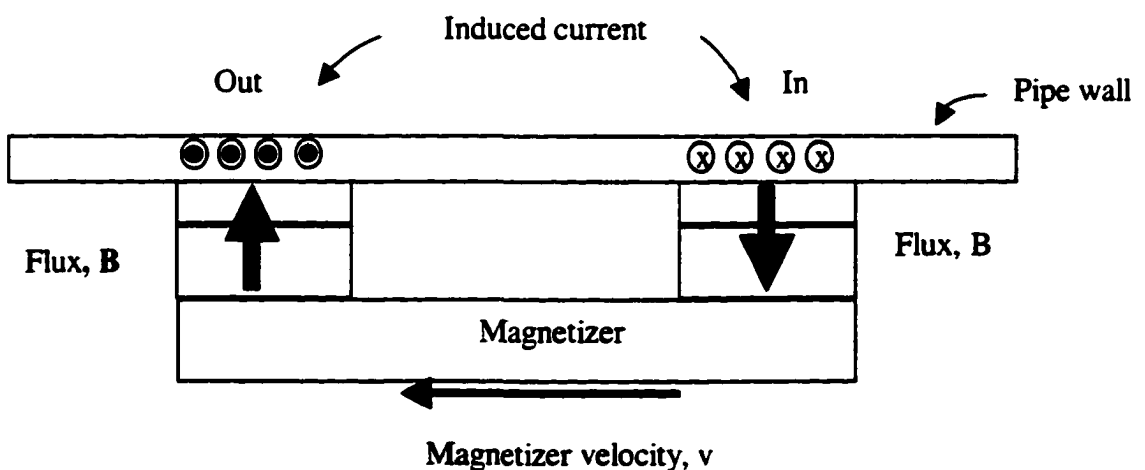


Figure 3.1. Current induction process due to interaction of magnetizer and velocity

3.1. Velocity Effect Analysis

The motion of magnetizer in the pipeline can be analyzed using a moving coordinate system [23] or a fixed coordinate system [24] [25] [26]. In the moving coordinate system, the observer is positioned on the moving object. In this case, there is no motion seen by the observer and the $\vec{v} \times \vec{B}$ term responsible for motion induced current does not appear in the governing equation. However, this method is laborious since the movement is taken into account by a moving mesh, involving extensive work in mesh regeneration. In the fixed coordinate system, the observer has fixed geometrical relation with the field source. The motion related term $\vec{v} \times \vec{B}$ is shown in the governing equation. The motion related term $\vec{v} \times \vec{B}$ results in spurious oscillations in the solution if the standard FEM methods, such as the Galerkin method, are used. However, there are several method [27] [28] [29] to overcome the spurious oscillations.

3.1.1. Fields Transformation

If we use prime variables for the moving coordinate system with a constant velocity, the differential equations in quasi-static magnetic field systems can be written as

$$\nabla \times \vec{H}' = \vec{J}' \quad (3.1)$$

$$\nabla \cdot \vec{B}' = 0 \quad (3.2)$$

$$\nabla \times \vec{E}' = -\frac{\partial \vec{B}'}{\partial t'} \quad (3.3)$$

$$\nabla \cdot \vec{D}' = 0 \text{ (no free charge)} \quad (3.4)$$

$$\vec{B}' = \mu' \vec{H}' \quad (3.5)$$

where ∇' and $\frac{\partial}{\partial t'}$ denote the space and time derivations, B' and E' are the magnetic and electric fields observed at the moving coordinate system. The equations (3.1) to (3.5) can be transformed to the equation using fixed coordinate system, that is, the coordinate system which is fixed on the field source. Before the transformation are derived, we need to derive the relationship between the two differential operators, ∇ and ∇' . Consider two inertial coordinate systems \vec{r} and \vec{r}' which are moving with a constant relative velocity \vec{v} . The time t and t' measured by observers in the two coordinate system are assumed same

$$t = t' \quad (3.6)$$

If the origin of the two coordinate systems are selected to coincide at $t=0$.

$$\vec{r} = \vec{r}' - \vec{v}t \quad (3.7)$$

For each coordinate system

$$x' = x - v_x t, \quad y' = y - v_y t, \quad z' = z - v_z t \quad (3.8)$$

Consider a scalar function $f'(x,y,z,t)$ which can be written as $f'(x',y',z',t')$ by substituting equation (3.6) and (3.7). The gradient of the primed coordinate system

$$\nabla' f = \frac{\partial f}{\partial x'} a_x + \frac{\partial f}{\partial y'} a_y + \frac{\partial f}{\partial z'} a_z \quad (3.9)$$

by the chain rule

$$\frac{\partial f}{\partial x} = \frac{\partial f}{\partial x'} \frac{\partial x'}{\partial x} + \frac{\partial f}{\partial y'} \frac{\partial y'}{\partial x} + \frac{\partial f}{\partial z'} \frac{\partial z'}{\partial x} + \frac{\partial f}{\partial t'} \frac{\partial t'}{\partial x} \quad (3.10)$$

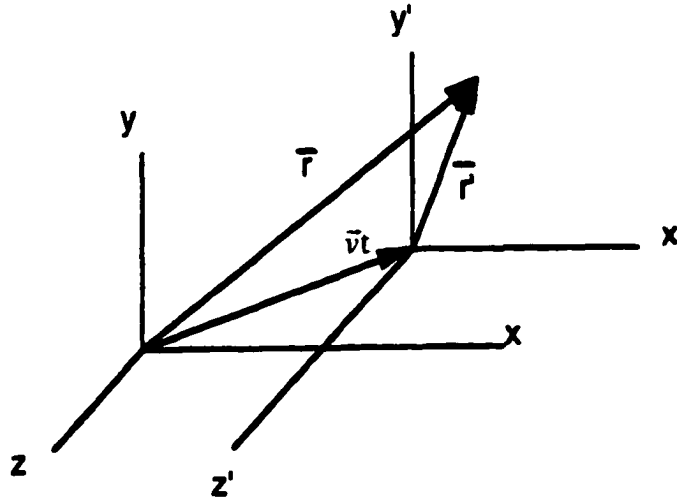


Figure 3.2. Two inertial coordinate system in relative motion

From equation (3.6) and (3.8)

$$\frac{\partial x'}{\partial x} = 1; \quad \frac{\partial y'}{\partial x} = \frac{\partial z'}{\partial x} = \frac{\partial t'}{\partial x} = 0$$

$$\frac{\partial y'}{\partial y} = 1; \quad \frac{\partial x'}{\partial y} = \frac{\partial z'}{\partial y} = \frac{\partial t'}{\partial y} = 0 \quad (3.11)$$

$$\frac{\partial z'}{\partial z} = 1; \quad \frac{\partial x'}{\partial z} = \frac{\partial y'}{\partial z} = \frac{\partial t'}{\partial z} = 0$$

Using equations (3.10) and (3.11) with (3.9)

$$\nabla' f = \nabla f \quad (3.12)$$

Similarly for vector functions \vec{B}' , we have the relation

$$\nabla \cdot \vec{B}' = \nabla \cdot \vec{B} \quad (3.13)$$

$$\nabla \times \bar{\mathbf{B}}' = \nabla \times \bar{\mathbf{B}}' \quad (3.14)$$

However, in the case of time derivative

$$\frac{\partial f}{\partial t} = \frac{\partial f}{\partial t'} \frac{\partial t'}{\partial t} + \frac{\partial f}{\partial x'} \frac{\partial x'}{\partial t} + \frac{\partial f}{\partial y'} \frac{\partial y'}{\partial t} + \frac{\partial f}{\partial z'} \frac{\partial z'}{\partial t} \quad (3.15)$$

From equation (3.6) and (3.8)

$$\frac{\partial t'}{\partial t} = 1, \quad \frac{\partial x'}{\partial t} = -v_x, \quad \frac{\partial y'}{\partial t} = -v_y, \quad \frac{\partial z'}{\partial t} = -v_z \quad (3.16)$$

Substituting equation (3.16) into (3.15)

$$\frac{\partial f}{\partial t} = \frac{\partial f}{\partial t'} - \left(v_x \frac{\partial}{\partial x'} + v_y \frac{\partial}{\partial y'} + v_z \frac{\partial}{\partial z'} \right) f = \frac{\partial f}{\partial t'} - (\bar{\mathbf{v}} \cdot \nabla') f \quad (3.17)$$

Using equation (3.12), rewrite equation (3.17)

$$\frac{\partial f}{\partial t'} = \frac{\partial f}{\partial t} + (\bar{\mathbf{v}} \cdot \nabla) f \quad (3.18)$$

If we define a vector $\bar{\mathbf{B}}'(x', y', z', t')$, using the same procedure

$$\frac{\partial \bar{\mathbf{B}}'}{\partial t'} = \frac{\partial \bar{\mathbf{B}}'}{\partial t} + (\bar{\mathbf{v}} \cdot \nabla) \bar{\mathbf{B}}' \quad (3.19)$$

By using a vector identity

$$\nabla \times (\bar{\mathbf{v}} \times \bar{\mathbf{B}}) = (\bar{\mathbf{B}} \cdot \nabla) \bar{\mathbf{v}} - (\bar{\mathbf{v}} \cdot \nabla) \bar{\mathbf{B}} + \bar{\mathbf{v}} (\nabla \cdot \bar{\mathbf{B}}) - \bar{\mathbf{B}} (\nabla \cdot \bar{\mathbf{v}}) \quad (3.20)$$

we have

$$\frac{\partial \bar{\mathbf{B}}'}{\partial t'} = \frac{\partial \bar{\mathbf{B}}'}{\partial t} - \nabla \times (\bar{\mathbf{v}} \times \bar{\mathbf{B}}') + \bar{\mathbf{v}} (\nabla \cdot \bar{\mathbf{B}}') \quad (3.21)$$

Using equation (3.13), (3.14) and (3.21), equations (3.6) to (3.8) can be expressed in the equivalent forms

$$\nabla \times \vec{H}' = \vec{J}' \quad (3.22)$$

$$\nabla \cdot \vec{B}' = 0 \quad (3.23)$$

$$\nabla \times (\vec{E}' - \vec{v} \times \vec{B}') = -\frac{\partial \vec{B}'}{\partial t} \quad (3.24)$$

$$\nabla \cdot \vec{D}' = 0 \text{ (no free charge)} \quad (3.25)$$

The differential equation of quasi-static magnetic field systems in the laboratory frame are

$$\nabla \times \vec{H} = \vec{J} \quad (3.26)$$

$$\nabla \cdot \vec{B} = 0 \quad (3.27)$$

$$\nabla \times \vec{E} = -\frac{\partial \vec{B}}{\partial t} \quad (3.28)$$

$$\nabla \cdot \vec{D} = 0 \text{ (no free charge)} \quad (3.29)$$

It has been postulated that equations (3.22) to (3.25) describe the same physical laws as equations (3.26) to (3.29). A comparison of the two sets of equations gives a consistent set of transformations which satisfies the requirements

$$\vec{H}' = \vec{H}, \quad \vec{B}' = \vec{B}, \quad \vec{D}' = \vec{D}, \quad \vec{E}' = \vec{E} + \vec{v} \times \vec{B} \quad (3.30)$$

The transformations in equation (3.30) relate the values of electromagnetic quantities in a quasi-static magnetic field system.

From the equation (3.19), it is clear that the right hand side is the rate of change with respect to time derivative of \vec{B}' for an observer moving with velocity \vec{v} . This derivative is also called convective derivative and can be written in the alternative form

$$\frac{D\vec{B}'}{Dt} = \frac{\partial \vec{B}'}{\partial t} + (\vec{v} \cdot \nabla) \vec{B}' \quad (3.31)$$

Consider a 1D movement in the z direction with a constant moving coordinate system as show in figure 3.3. The time derivative term at a point $P(Z)$ moving with the coordinate system at an instant $t + \Delta t$ can be written

$$\begin{aligned}
 \frac{\partial B^{t+\Delta t}(Z)}{\partial t} &= \frac{B^{t+\Delta t}(Z) - B^t(Z)}{\Delta t} \\
 &= \frac{B^{t+\Delta t}(z_2) - B^t(z_1)}{\Delta t} \\
 &= \frac{B^{t+\Delta t}(z_2) - B^t(z_2)}{\Delta t} + \frac{\Delta z}{\Delta t} \frac{B^t(z_2) - B^t(z_1)}{\Delta z} \\
 &= \frac{\partial B^{t+\Delta t}(z_2)}{\partial t} + v_z \frac{\partial B^t}{\partial z} \\
 &= \frac{\partial B^{t+\Delta t}(z_2)}{\partial t} + (v \cdot \nabla) A^t \equiv \frac{DA}{Dt}
 \end{aligned} \tag{3.32}$$

where z_1 and z_2 are fixed coordinate system. Again, the convective derivative in (3.31) is obtained.

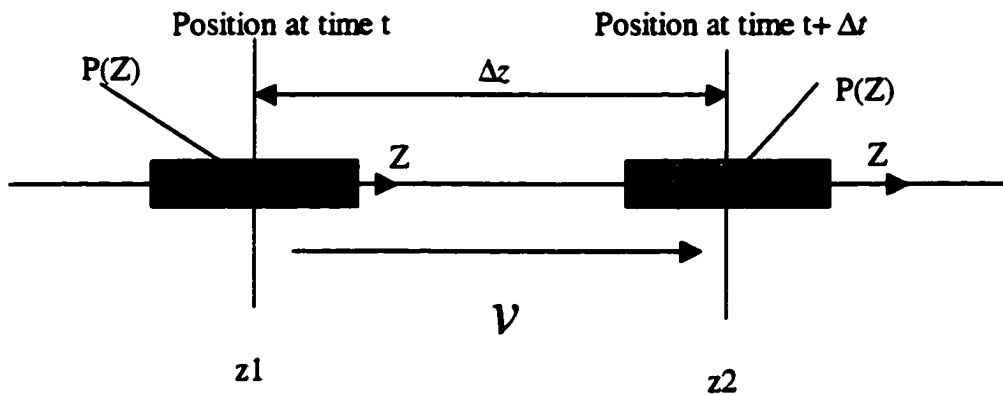


Figure 3.3. Example of 1D movement with a constant velocity

3.1.2 Governing Equation

Quasi-static magnetic field equations can be expressed as

$$\nabla \times \vec{H} = \vec{J} \quad (3.33)$$

$$\nabla \cdot \vec{B} = 0 \quad (3.34)$$

$$\nabla \times \vec{E} = -\frac{\partial \vec{B}}{\partial t} + \nabla \times (\vec{v} \times \vec{B}) \quad (3.35)$$

$$\nabla \cdot \vec{D} = 0 \quad (\text{no free charge}) \quad (3.36)$$

$$\vec{B} = \mu \vec{H} \quad (3.37)$$

In terms of the vector magnetic potential defined by

$$\nabla \times \vec{A} = \vec{B} \quad (3.38)$$

Equation (3.1), (3.5) and (3.6) can be used to derive the equation

$$\nabla \times \frac{1}{\mu} \nabla \times \vec{A} = \vec{J} \quad (3.39)$$

where $\vec{J} = \vec{J}_s + \vec{J}_e$, \vec{J}_s is equivalent source current and \vec{J}_e is induced eddy current. Substituting equation (3.38) into (3.35) results in

$$\nabla \times \left(\vec{E} + \frac{\partial \vec{A}}{\partial t} - \vec{v} \times \nabla \times \vec{A} \right) = 0 \quad (3.40)$$

Using the vector identity $\nabla \times (\nabla \cdot \vec{V}) = 0$, we can write

$$\vec{E} + \frac{\partial \vec{A}}{\partial t} - \vec{v} \times \nabla \times \vec{A} = -\nabla \cdot \vec{V} \quad (3.41)$$

For an isotropic and homogeneous conducting medium we have

$$\vec{J}_e = \sigma \vec{E} \quad (3.42)$$

Substituting equation (3.41) into (3.42)

$$\bar{\mathbf{J}}_e = -\sigma \frac{\partial \bar{\mathbf{A}}}{\partial t} + \sigma \bar{\mathbf{v}} \times \nabla \times \bar{\mathbf{A}} - \sigma \nabla V \quad (3.43)$$

For 2D axisymmetric case $\nabla V = 0$. Substituting equation (3.43) into (3.39) results in the governing equation

$$\nabla \times \frac{1}{\mu} \nabla \times \bar{\mathbf{A}} = \bar{\mathbf{J}}_s - \sigma \frac{\partial \bar{\mathbf{A}}}{\partial t} + \sigma \bar{\mathbf{v}} \times \nabla \times \bar{\mathbf{A}} \quad (3.44)$$

The above equation includes two velocity related terms. (1) $\sigma \frac{\partial \bar{\mathbf{A}}}{\partial t}$ is the current density due to a change in the magnetic vector potential with time. (2) $\sigma \bar{\mathbf{v}} \times \nabla \times \bar{\mathbf{A}}$ is the current density due to the relative motion of the magnetic field and a pipewall. To solve (3.44), there are several methods for time stepping including Donea's method [27], Zienkiewicz's method [28] and Leismann and Frind's method [29]. A detailed comparison and analysis of each method is shown in [30] and it was found that Lesimann and Frind's method results in more accurate and stable results. In the following section, Lesimann and Frind's method is used for the transient analysis.

3.1.3. Transient Analysis

For the 2D axisymmetric case, equation (3.44) reduces to:

$$\frac{1}{\mu} \left[\frac{\partial}{\partial r} \left\{ \frac{1}{r} \frac{\partial}{\partial r} (r \bar{\mathbf{A}}) \right\} + \frac{\partial}{\partial z} \left(\frac{\partial \bar{\mathbf{A}}}{\partial z} \right) \right] = \sigma \frac{\partial \bar{\mathbf{A}}}{\partial t} + \sigma \bar{\mathbf{v}} \frac{\partial \bar{\mathbf{A}}}{\partial z} - \bar{\mathbf{J}}_s \quad (3.45)$$

The term $\sigma \frac{\partial \bar{\mathbf{A}}}{\partial t}$ represents the defect-induced current density resulting from the time varying magnetic field caused by the changing spatial relation between the defect and magnetizer. In the case of a defect free pipe, this term is zero. The velocity term $\sigma \bar{\mathbf{v}} \times \nabla \times \bar{\mathbf{A}}$ is modeled

using the Leismann-Frind method [29], described below. Consider the 1D case of equation (2.2)

$$\sigma \frac{\partial A}{\partial t} = \frac{1}{\mu} \frac{\partial^2 A}{\partial z^2} - \sigma v \frac{\partial A}{\partial z} + J_s \quad (3.46)$$

In the Leismann-Frind method, an artificial diffusion term is introduced and individual time weighting factors are used for each time step. The artificial diffusion term and the weighting factors are determined during a process of error minimization.

Introducing the artificial term (D^*) in equation (3.46) and using separate time weighting

factors $\frac{\partial A}{\partial t} = \frac{A^{n+1} - A^n}{\Delta t}$, we have

$$\begin{aligned} \sigma \frac{A^{n+1} - A^n}{\Delta t} = & \theta_d \frac{1}{\mu} \frac{\partial^2 A^{n+1}}{\partial z^2} + (1 - \theta_d) \frac{1}{\mu} \frac{\partial^2 A^n}{\partial z^2} - \theta_v \sigma v \frac{\partial A^{n+1}}{\partial z} \\ & - (1 - \theta_v) \sigma v \frac{\partial A^n}{\partial z} + \theta_a D^* \frac{\partial^2 A^{n+1}}{\partial z^2} + (1 - \theta_a) D^* \frac{\partial^2 A^n}{\partial z^2} \end{aligned} \quad (3.47)$$

here, θ_d , θ_v , and θ_a are the weighting factors and D^* is artificial diffusion term.

Using the central difference method $t = t_n + \frac{\Delta t}{2}$ for the time stepping.

$$A(t) = A\left(t_n + \frac{\Delta t}{2}\right)$$

Taylor series expansion for magnetic vector potential at old and new times, with the central difference scheme, is derived as

$$\begin{aligned} A^{n+1} &= A\left[\left(t_n + \frac{\Delta t}{2}\right) + \frac{\Delta t}{2}\right] \\ &= A\left(t_n + \frac{\Delta t}{2}\right) + \frac{\Delta t}{2} \frac{\partial A\left(t_n + \frac{\Delta t}{2}\right)}{\partial t} + \frac{\Delta t^2}{8} \frac{\partial^2 A\left(t_n + \frac{\Delta t}{2}\right)}{\partial t^2} + \mathcal{O}(\Delta t^3) \end{aligned} \quad (3.48)$$

$$\begin{aligned}
A^n &= A \left[\left(t_n + \frac{\Delta t}{2} \right) - \frac{\Delta t}{2} \right] \\
&= A \left(t_n + \frac{\Delta t}{2} \right) - \frac{\Delta t}{2} \frac{\partial A \left(t_n + \frac{\Delta t}{2} \right)}{\partial t} + \frac{\Delta t^2}{8} \frac{\partial^2 A \left(t_n + \frac{\Delta t}{2} \right)}{\partial t^2} + \mathcal{O}(\Delta t^3)
\end{aligned} \tag{3.49}$$

Substituting equations (3.48) and (3.49) into equation (3.47) gives

$$\begin{aligned}
\sigma \frac{\partial A}{\partial t} &= \frac{1}{\mu} \frac{\partial^2 A}{\partial z^2} - \sigma v \frac{\partial A}{\partial z} + J_s \\
&+ \left(\theta_d - \frac{1}{2} \right) \Delta t \frac{1}{\mu} \frac{\partial^2}{\partial z^2} \frac{\partial A}{\partial t} + \left(\frac{1}{2} - \theta_v \right) \sigma v \Delta t \frac{\partial}{\partial z} \frac{\partial A}{\partial t} \\
&+ D^* \frac{\partial^2 A}{\partial z^2} + \left(\theta_a - \frac{1}{2} \right) D^* \Delta t \frac{\partial^2}{\partial z^2} \frac{\partial A}{\partial t} + \mathcal{O}(\Delta t^2)
\end{aligned} \tag{3.50}$$

The first line of equation (3.50) is the same as equation (3.46) and hence the remaining term is error term. Rewriting the error terms

$$(1 - \theta_d - \theta_v) v \Delta t \frac{1}{\mu} \frac{\partial^3 A}{\partial z^3} + \left[D^* - \left(\frac{1}{2} - \theta_d \right) \sigma v^2 \Delta t \right] \frac{\partial^2 A}{\partial z^2} + \left(\theta_a - \frac{1}{2} \right) D^* \Delta t \frac{1}{\mu} \frac{\partial^2 A}{\partial z^2} \tag{3.51}$$

In order to make the coefficient matrix symmetric, the velocity term is evaluated at the old time which requires that θ_v be zero. In order to reduce the error term to zero, all the individual coefficients must equal zero. This results in $\theta_d = 1$ and $D^* = \frac{\sigma v^2 \Delta t}{2}$. The unknown

value θ_a is decided by stability requirements. It is shown that stability can be guaranteed if

$\theta_a \geq \frac{1}{2}$ and unlimited stability is achieved when $\theta_a \geq \frac{1}{3}$. Finally, substituting these

weighting factors and the artificial diffusion term into equation (3.50) we get the Leismann-

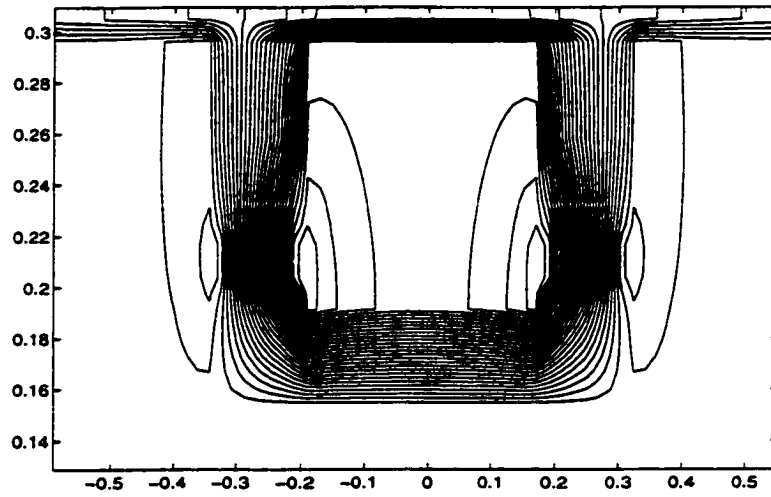
Frind equation for the 1D case as

$$\begin{aligned}
& \left[\frac{\sigma}{\Delta t} - \frac{1}{\mu} \frac{\partial^2}{\partial z^2} - \theta_a \frac{\sigma v^2 \Delta t}{2} \frac{\partial^2}{\partial z^2} \right] A^{n+1} \\
& = J_s + \left[\frac{\sigma}{\Delta t} + (1 - \theta_a) \frac{\sigma v^2 \Delta t}{2} \frac{\partial^2}{\partial z^2} - \sigma v \frac{\partial}{\partial z} \right] A^n
\end{aligned} \tag{3.52}$$

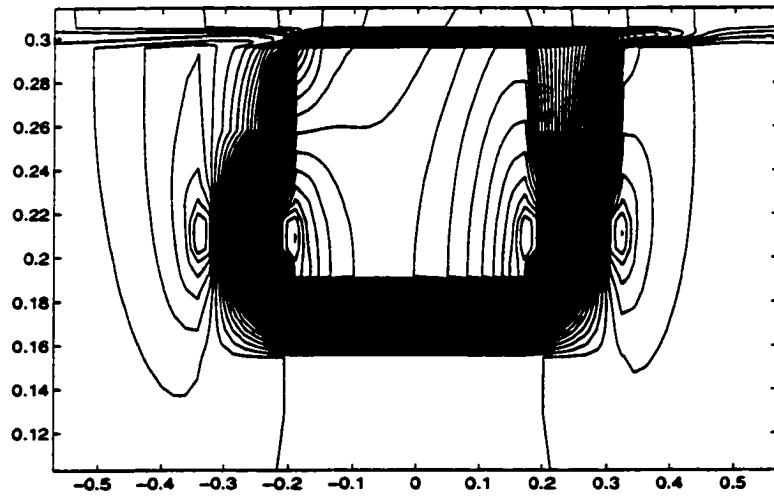
The above equation computes the solution, A^{n+1} , at the $(n+1)^{\text{th}}$ time from a known set of solution values A^n at the n^{th} time step. Figure 3.4 shows the flux plot (a) with 10^{-6} m/s (zero velocity) and (b) with 5 m/s. It is seen that the flux lines are distorted significantly due to velocity effect. Figure 3.5 shows the induced current of (a) 10^{-6} m/s and (b) 5 m/s. Motion induced current at zero velocity is almost negligible when compared to the induced current at 5 m/s. Figure 3.6. shows the comparison of the MFL signal with static case and velocity (5 m/s)

3.2 Nonlinear Analysis

A second issue in this model is the nonlinear magnetic characteristics of the pipewall. In the linear problem, the operating points of ferromagnetic material assumed to be in the linear region of the B-H curve. In the reality, however, high magnetization levels drive the pipewall and backing iron to saturation. The operating point of the ferromagnetic material varies considerably. Detailed investigation and modeling of the nonlinear permeability of the pipewall and backing iron is shown in [15]. Figure 3.7 shows the B-H characteristic of the pipewall (1) and backing iron (2). The initial value of B is obtained from figure 3.7 to calculate the initial value of reluctivity $\nu = \frac{H}{B}$ which is the input to the FEM code. The magnitude of B is then calculated using the FEM code. The magnitude of B is then calculated

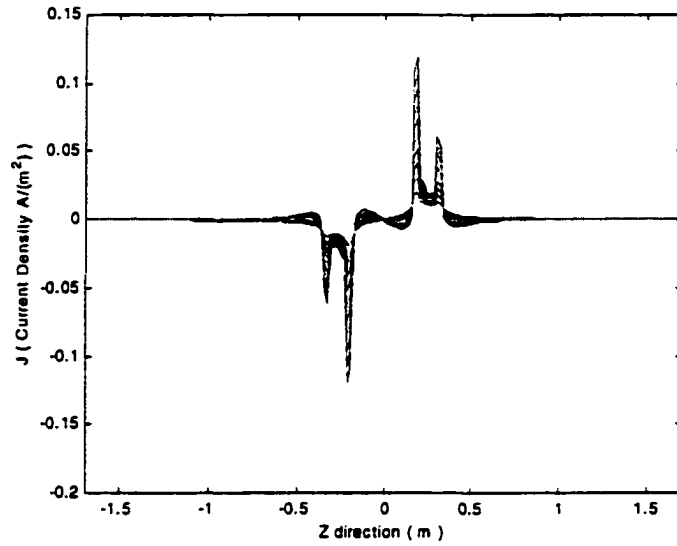


(a)

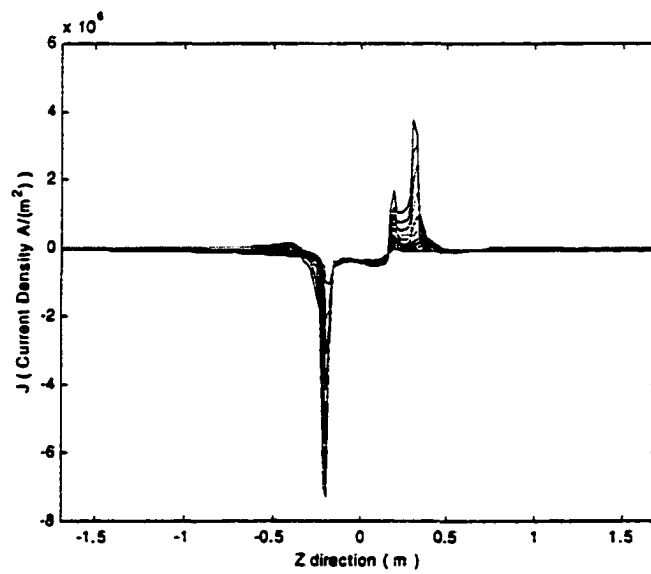


(b)

Figure 3.4. Velocity effect on the flux line at (a) zero m/s and (b) 5 m/s

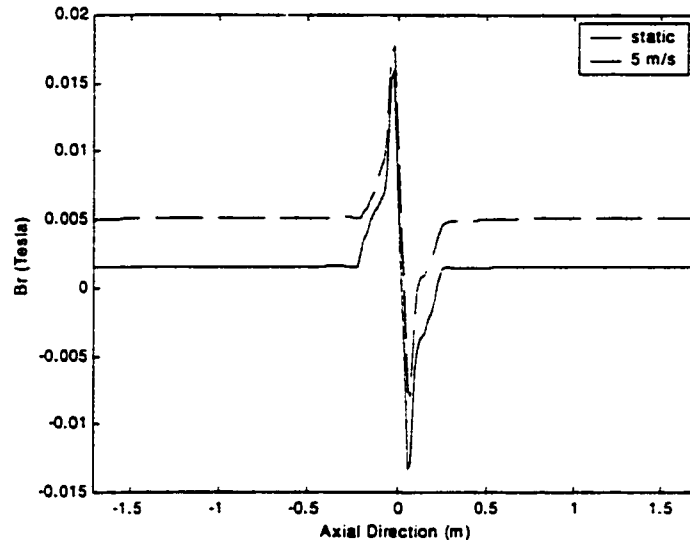


(a)

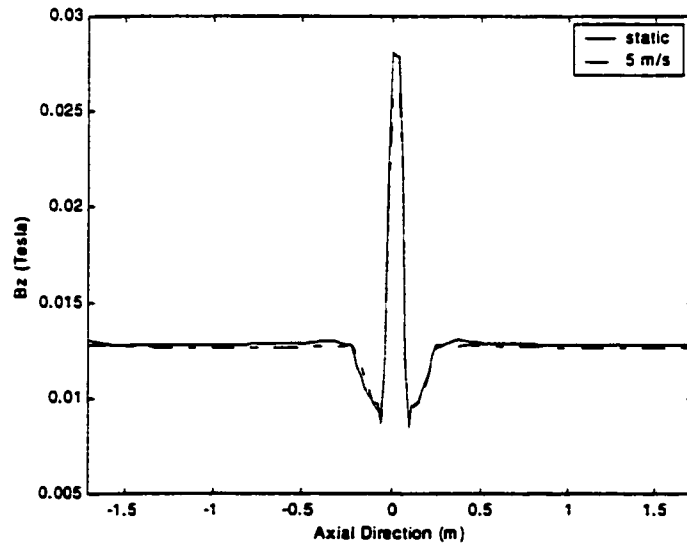


(b)

Figure 3.5. Induced currents in the pipewall at velocity (a) zero m/s and (b) 5 m/s



(a)



(b)

Figure 3.6. MFL signal with velocity (zero and 5 m/s)

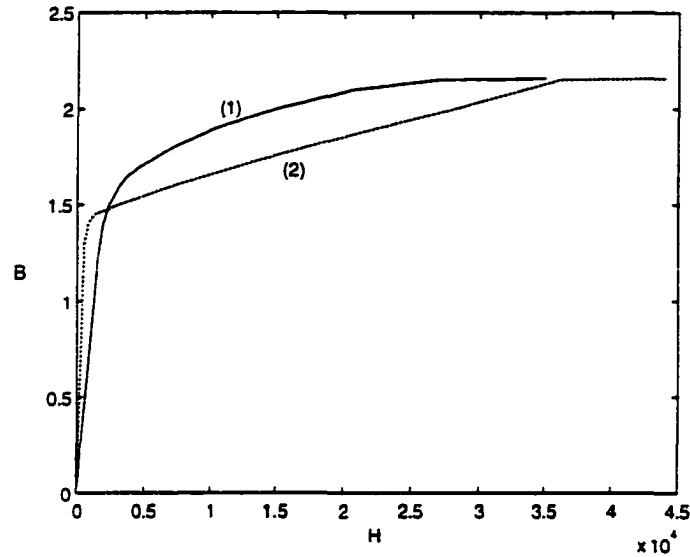


Figure 3.7. B-H characteristic of pipewall (1) and backon iron (2)

using the FEM code. The magnitude H is calculated using two sampling points on the B-H curve close to the calculated magnitude of B as follows:

$$H = H_1 + \frac{[H_2 - H_1]}{[B_2 - B_1]} [B - B_1] \quad (3.53)$$

B_1 , B_2 are the sampling points close to B . H_1 and H_2 are the sampling points close to calculated magnitude of H . Figure 3.8 shows this linear interpolation scheme. The reluctivity ν is calculated in each element as follow:

$$\nu = \frac{H}{B} \quad (3.54)$$

The new reluctivity values are calculated for the next step as follows:

$$\nu_{\text{new}} = (\nu - \nu_{\text{old}}) * fac + \nu_{\text{old}} \quad (3.55)$$

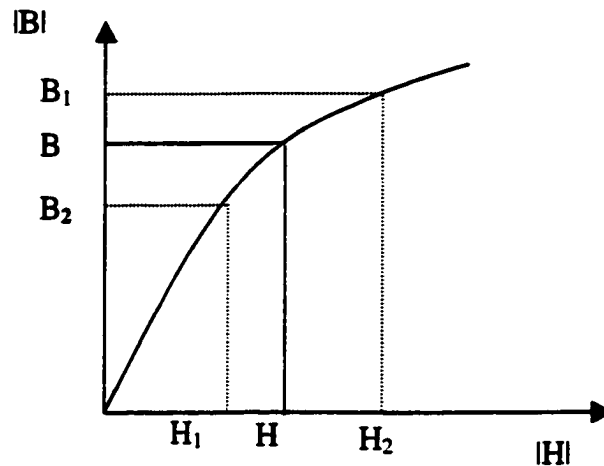


Figure 3.8. Operating point on the B-H curve

where fac is a damping factor to control the convergence. For the transient case, the nonlinear procedure includes two steps. The first step is the nonlinear step which consists of an iterative process within a certain time step (t_k). The second step is the time step which calculates both old and new values of the unknown function A_{t_k} and $A_{t_{k+1}}$.

The nonlinear algorithm with the time stepping scheme is as follows:

1. Initialize the reluctivity value ν to a certain constant.
2. Run with the fixed reluctivity value with time stepping
3. Increment time step $k=k+1$. Reset B , $A_{new t_k}$
4. Calculate the reluctivity value, B and $A_{new t_k}$ using FEM formulation with time stepping.

5. Compare A_{old, t_k} and A_{new, t_k} . If the difference is not less than a threshold, then $A_{old, t_k} = A_{new, t_k}$ and go to step 3. Otherwise, it is considered that the iteration has converged to the reluctivity value ν corresponding to the B-H curve.
6. $A_{t_{k-1}} = A_{t_k}$. If all time steps are done, then stop. Otherwise go to step 3.

Figure 3.9 shows the flow chart of the overall nonlinear procedure with time stepping. Figure 3.10 shows the current density plots in the pipe-wall for the (a) linear case and (b) nonlinear case, in the absence of any defects. The pig velocity is 5 m/s. The profile with the maximum amplitude corresponds to the innermost pipe-wall layer. These results show that there is a significant difference between linear and nonlinear models and a full nonlinear model needs to be used for more accurate simulation of the underlying physics.

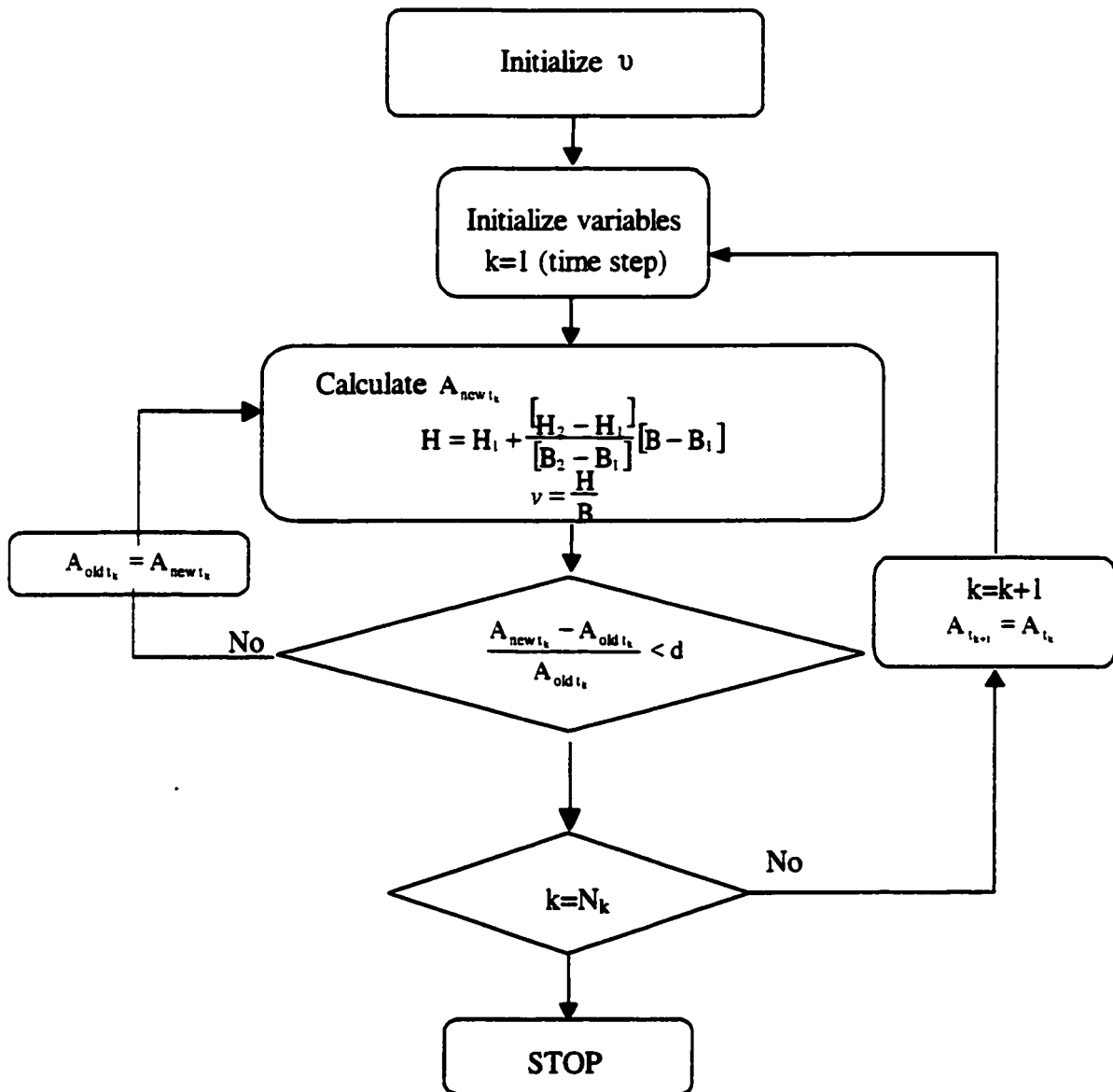
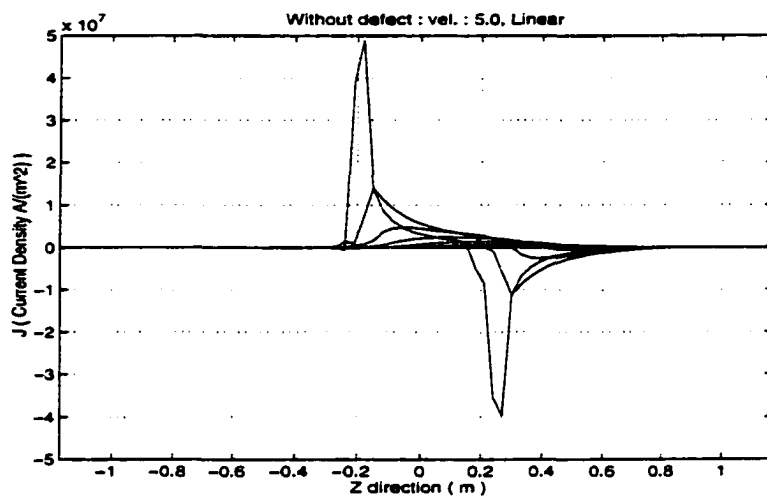
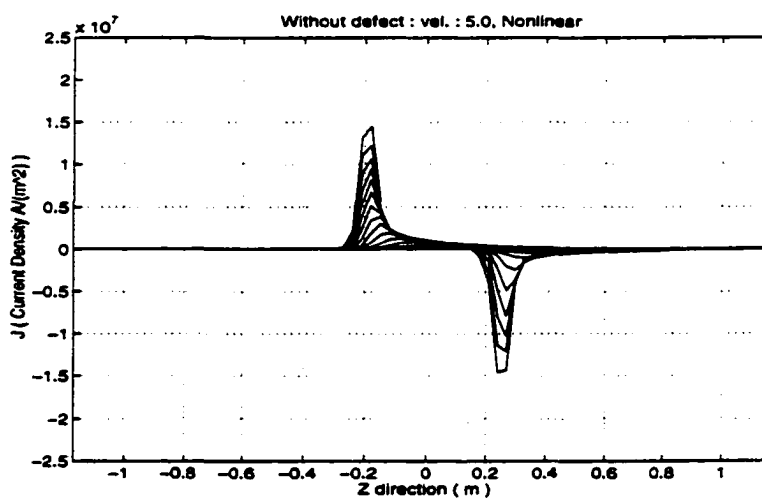


Figure 3.9. Flow chart of overall nonlinear procedure with time stepping



(a)



(b)

Figure 3.10. Current density plot in pipe-wall (a) Linear (b) Nonlinear

CHAPTER IV. MODELING OF CURRENT PERTURBATION METHOD

4.1. Introduction

The conventional MFL tool generates axial magnetic flux and cannot effectively detect and characterize axially oriented stress corrosion cracks. However, as mentioned in chapter 3, due to tool velocity, conventional MFL tools also generate strong circumferentially oriented currents. These currents are perpendicular to the SCC, and can be used to detect the presence of axially oriented SCC. The interaction of these currents with axially oriented SCC results in a perturbation of the current distribution. The fields associated with the perturbation currents carry information relating to the presence of axial SCC.

Stress corrosion cracks are in general extremely tight and in order to model a tight crack with infinitesimal width as shown in figure 4.1 and simulate the motion induced current in the pipe wall and the current perturbation fields, a full three dimension (3D) numerical modeling is needed.

The development of a 3D model is a significant challenge in terms of both computational time and memory requirement. The challenges arise due to nonlinear material property, the size of tight cracks relative to that of the pipe and magnetizer dimensions, and also due to time stepping involved in modeling velocity effects.

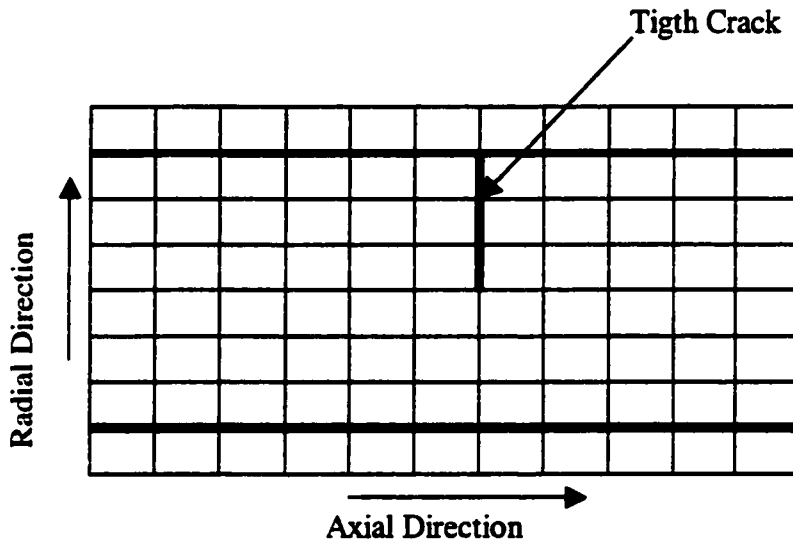


Figure 4.1 Tight crack

The modeling approach proposed in this thesis addresses these problems by decomposing the overall task into four simpler subtasks that can be performed sequentially. In this procedure, first, we assume that the perturbation effect due to defect is limited to a small region around the defect. This helps in reducing the region of interest that needs to be modeled. Second, the region of interest is assumed to be located remote from the magnetizer where the fields are significantly smaller and hence we can assume linearity. This allows the use of the superposition principle, where the total current is divided into (i) background current (\vec{J}_0) which is the circumferential current due to the velocity effect in the absence of defect and (ii) perturbation current (\vec{J}_p) due to the introduction of an SCC. Figure 4.2 shows the decomposition of the total current into background current and perturbation current. The details of each step are described next.

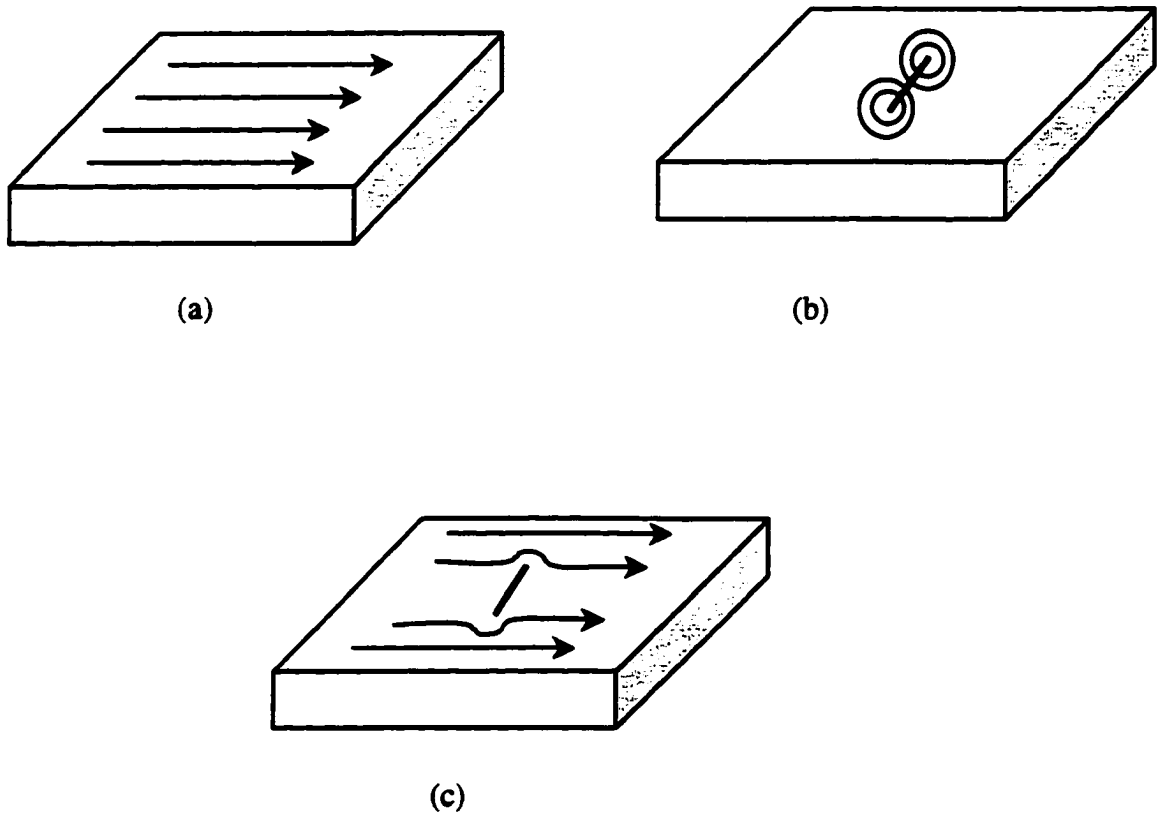


Figure 4.2. Current decomposition (a) background current (b) perturbation current (c) total current

4.2. Single Layer Source Model

4.2.1. Step1: Calculation of Velocity Induced Currents

In this step, a defect free pipe with a magnetizer moving at a fixed velocity is modeled. The governing equation for this step is

$$\nabla \times \frac{1}{\mu} \nabla \times \vec{A} = \vec{J}_s - \sigma \frac{\partial \vec{A}}{\partial t} + \sigma \vec{v} \times \nabla \times \vec{A} \quad (4.1)$$

where, \vec{A} is magnetic vector potential, μ is magnetic permeability, \vec{v} is velocity, σ is electrical conductivity and \vec{J}_s is source current density. Figure 4.3 shows the geometry of

step 1. The term $\sigma \frac{\partial \vec{A}}{\partial t}$ represents the defect-induced current density by the changing spatial relation between the defect and magnetizer. In the case of a defect free pipe, this term is zero.

The velocity term $\sigma \vec{v} \times \nabla \times \vec{A}$ is modeled using the Leismann-Frind method. Since the defect free geometry is completely axisymmetric the equation (4.1) reduces to the two dimensional form in the cylindrical coordinate system. The velocity-induced current \vec{J}_0 in the defect free pipewall is calculated using the relation.

$$\vec{J}_0 = -\sigma \vec{v} \frac{\partial \vec{A}}{\partial z} \quad (4.2)$$

Motion induced current distribution in the pipe wall without defect at a velocity of 5 m/s is shown in figure 4.4 (a). The axial distribution of currents on the inner surface (1) middle of pipe wall (2) and outer surface of the pipe wall (3) show that in the vicinity of the magnetizer, the current decays from the ID to the OD of the pipe. Figure 4.3. (b) shows the current distribution in the remote field region where the current decays from OD to ID. The current \vec{J}_0 is used as the source term in step 2, which models a section of the pipe wall in the remote field region.

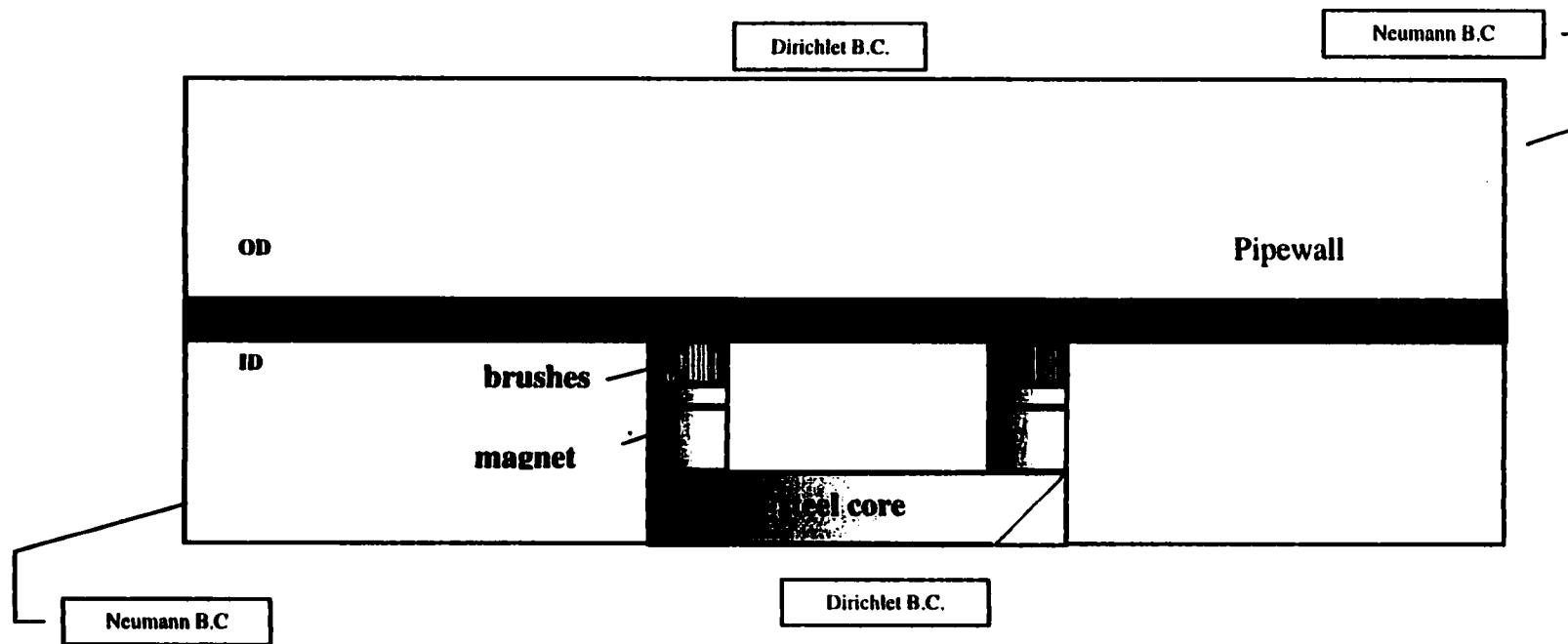
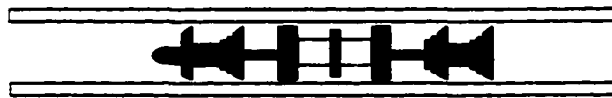
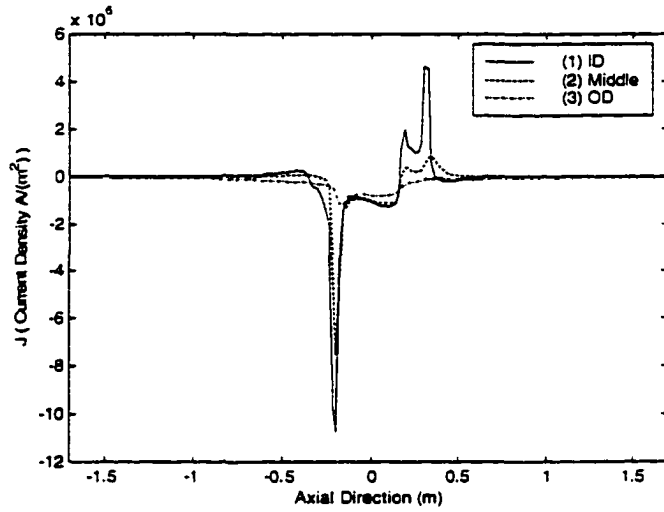
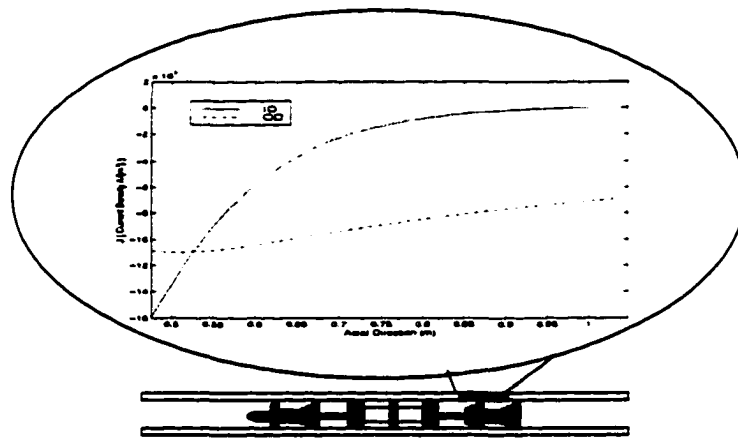


Figure 4.3. . Geometry of step 1



(a)



(b)

Figure 4.4. Motion induced current distribution in the pipe wall (velocity :5 m/s),
 (a) whole pipewall, (b) remote region

4.2.2. Step2: Calculation of Perturbation Current by SCC

A tight crack of zero volume Ω_{defect} is now introduced in the remote field region of the pipe as shown in figure 4.5. Assuming symmetry about the defect plane, only half the geometry is modeled. The basic assumption in this step is linearity of constitutive relations in the remote field region, so that the total current \bar{J} in the presence of SCC is the sum of the background current \bar{J}_0 in the defect free pipe and the anomalous perturbation current \bar{J}_p introduced by the SCC. Let Ω_{defect} be the SCC domain characterized by a set of nodes. Then we can define

$$\bar{J}_p = \begin{cases} -\bar{J}_0 & \text{in } \Omega_{\text{defect}} \\ \text{unknown} & \text{in } \Omega^c_{\text{defect}} \end{cases} \quad (4.3)$$

where Ω^c_{defect} is the complements of Ω_{defect} . The total current is given by:

$$\bar{J} = \bar{J}_0 + \bar{J}_p \quad (4.4)$$

On Ω_{defect} we have

$$\bar{J}_p = -\bar{J}_0 = \sigma \left(\frac{\partial \bar{A}}{\partial t} + \nabla V \right) \quad (4.5)$$

where V is the electric scalar potential.

Ignoring the contribution of the term $\sigma \frac{\partial \bar{A}}{\partial t}$, at first, we apply the Neumann boundary

conditions on the defect nodes i

$$\left. \frac{\partial V}{\partial n} \right|_i = - \left. \frac{\bar{J}_0}{\sigma} \right|_i \quad (4.6)$$

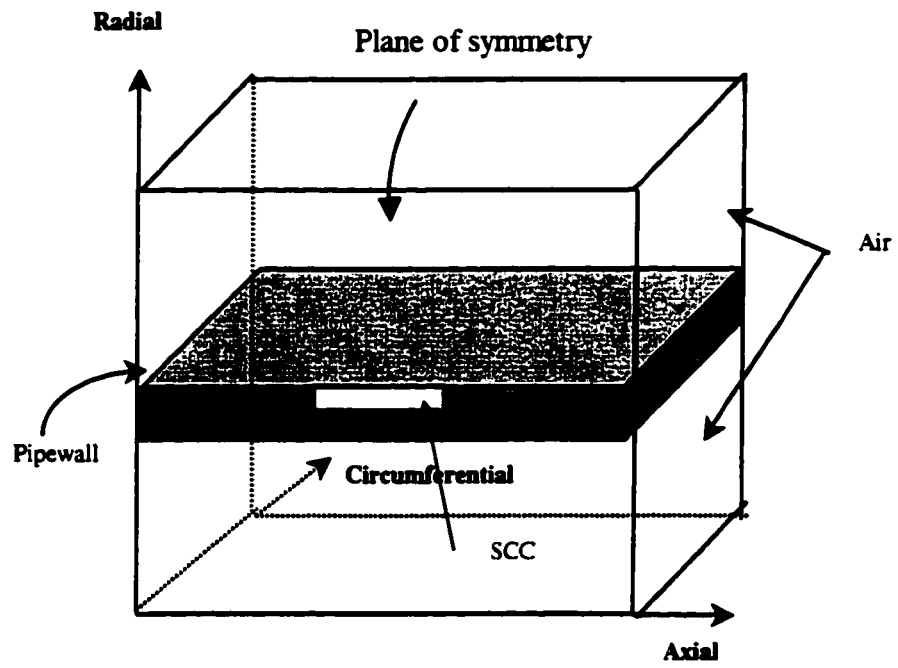


Figure 4.5. Geometry of step 2.

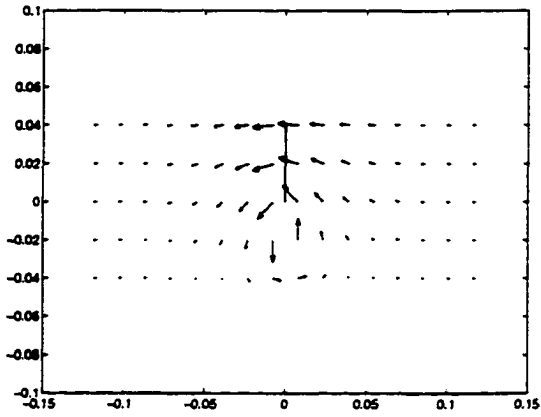
where \bar{J}_0 is the current distribution obtained in step 1. The solution of the governing Laplace Equation $\nabla^2 V = 0$ gives as a first approximation, the perturbation currents \bar{J}_p in the pipe wall section with an axial SCC. The perturbation currents \bar{J}_p due to a SCC are shown in figure 4.6, (a) side view and (b) top view. Total current \bar{J} is shown in figure 4.6, (c) side view and (d) top view.

4.2.3. Step 3: Calculation of Current Perturbation Fields

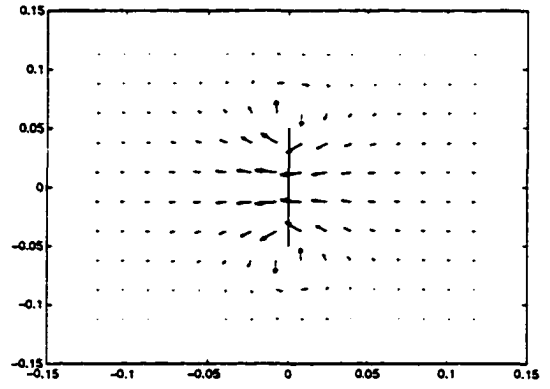
The fields associated with the perturbation currents are calculated in this step. The governing equation for this step in terms of the vector magnetic potential is the three dimensional equation

$$\nabla \times \frac{1}{\mu} \nabla \times \bar{A} = \bar{J}_p \quad (4.7)$$

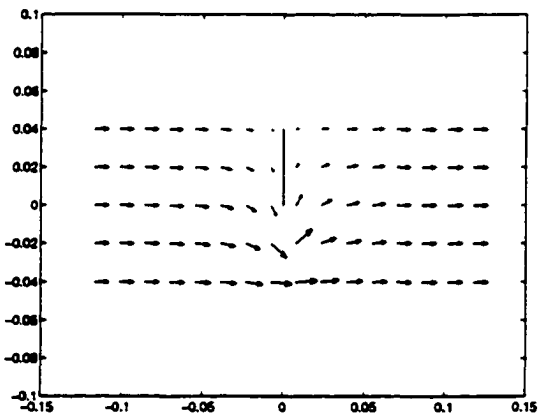
where \bar{J}_p is the current distribution obtained in step 2. This solution of the above equation is a first approximation of \bar{A} . The solution is used in equation (4.5) in the term $\sigma \frac{\partial \bar{A}}{\partial t}$ to correct the defect free current distribution and steps 2 and 3 are iterated until convergence is obtained. The final solution \bar{A} is used for computing the flux density $\bar{B} = \nabla \times \bar{A}$ associated with the perturbation currents. The fields obtained at the lift off of 0.1 cm in step 3 are plotted in figure 4.7. The defect signal is obtained by measuring the voltage induced in a coil held perpendicular to the circumferential component B_z of the flux.



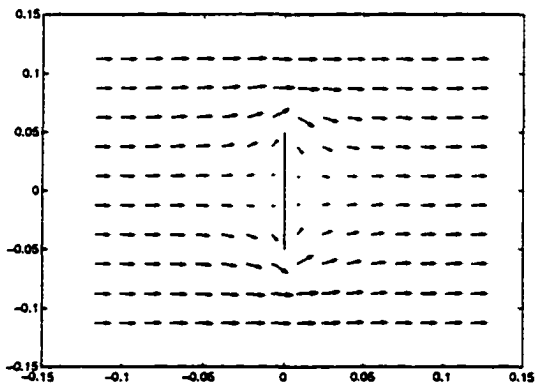
(a)



(b)

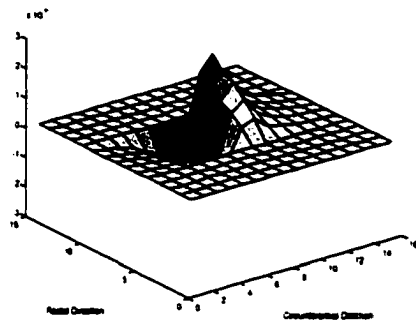


(c)

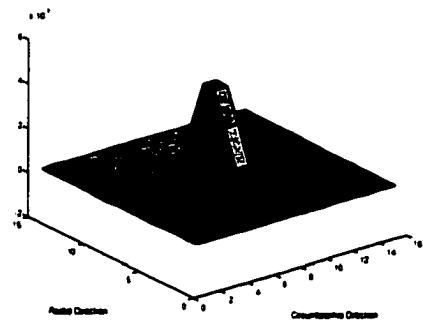


(d)

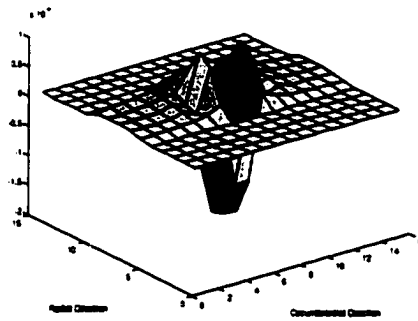
Figure 4.6. Step 2 results, perturbation current, (a) side view (b) top view, total current (background + perturbation current) (c) side view (d) top view



(a)



(b)



(c)

Figure 4.7. Fields of step 3. (a) Circumferential (b) Radial (c) Axial component

4.2.4. Step 4: Measurement of perturbation fields using a coil

The motion of the tool is modeled by implementing steps 2 and 3 for each position of the defect relative to the pig and sensor coil, which are kept fixed. For each position of the magnetizer, the flux ϕ calculated using axial field components as follow:

$$\phi_i = \int B_z \cdot ds \quad (4.8)$$

The induced voltage in the sensor coil is then computed using the following equation:

$$V_i = -N \frac{d\phi_i}{dt}, \quad i = 1, 2, \dots, n \quad (4.9)$$

where, V_i is the signal due to each axial component of the current perturbation fields and N is number of turns of coil.

4.3. Double Layer Source Model

The modeling of a single SCC allows the use of symmetry about the crack plane. However SCC usually occurs in groups or colonies. In the multiple SCC case, the symmetry is no longer guaranteed. A simple example of a group of SCCs oriented parallel to each other is shown in figure 4.8. In this case each crack must be modeled in entirety using two layers of source nodes. Double layer source models are widely used in the boundary integral method [31]. The following section describes this approach in detail.

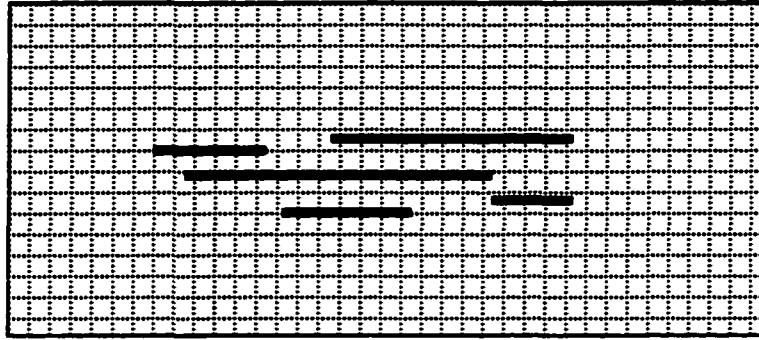


Figure 4.8. Example of SCC colony

4.3.1. Single layer charge distribution

It is known that if the charge is distributed on a surface S with density ρ_s , which is a bounded and piecewise continuous function of position S , the potential at any point not on S is

$$V(\mathbf{r}) = \frac{1}{4\pi\epsilon_0} \int_S \frac{\rho_s(\mathbf{r}')}{R} dS' \quad (4.10)$$

where $V(\mathbf{r})$ is a continuous function. The potential produced by a surface charge distribution is a bounded, continuous function of position of all points both on and off the surface, and is therefore continuous across the surfaces.

$$V_+ = V_- = V_s \text{ on } S \quad (4.11)$$

The subscripts '+' and '-' denote the potential just outside and inside of the surface, respectively. On the other hand the field intensity

$$\mathbf{E}(\mathbf{r}) = -\nabla V = \frac{1}{4\pi\epsilon_0} \int_S \rho_s(\mathbf{r}') \nabla \left(\frac{1}{R} \right) dS' \quad (4.12)$$

is continuous and has continuous derivative at all points not on the surface. The field intensity, however, undergoes an abrupt change across the surface S . The interface condition on the electric flux density D or field intensity E are

$$(D_+ - D_-) \cdot \mathbf{n} = \rho_s, \quad (4.13)$$

$$\mathbf{E}_+ - \mathbf{E}_- = \frac{\rho_s}{\epsilon} \mathbf{n} \quad (4.14)$$

where, '+' and '-' denote outside and inside the surface, \mathbf{n} is the outward unit vector normal to S . Figure 4.9 shows the field discontinuity along the single layer source.

If the surface charge density is modeled as a single layer source, it is equivalent to an inhomogeneous Neuman boundary condition (boundary condition of the second kind). In other words, the boundary value problems with inhomogeneous boundary conditions of the second kind are identical to those of a single layer source on the boundary surface.

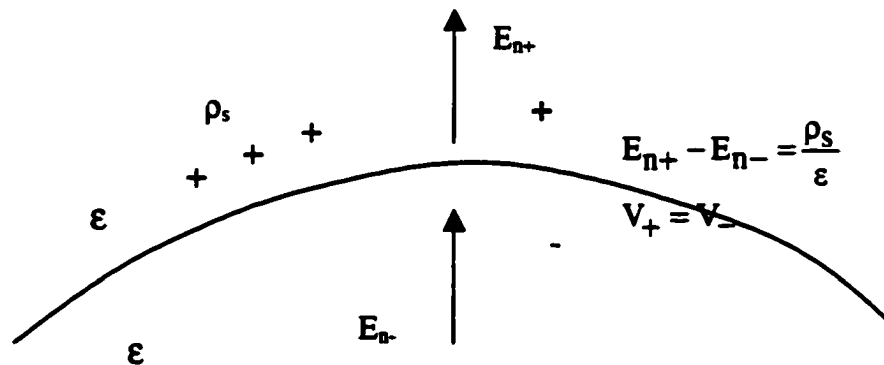


Figure 4.9 Field discontinuity along the single layer source

4.3.2. Double layer source distribution

Consider a double layer charge distribution, where the positive charges are distributed on the positive side of a closed surface S and the negative charges are distributed on the opposite side. The double layer charge distribution is separated by the infinitesimal distance dl which is shown in figure 4.10

The dipole moment per unit area is defined as

$$\tau = n \lim_{\substack{\rho_s \rightarrow \infty \\ dl \rightarrow 0}} (\rho_s dl) \quad (4.15)$$

The potential induced by the double layer source at a point $P(\mathbf{r})$ not on the surface S is

$$dV(\mathbf{r}) = \frac{1}{4\pi\epsilon_0} \frac{\tau \cos\theta}{R^2} dS' = \frac{1}{4\pi\epsilon_0} \tau \cdot \nabla \left(\frac{1}{R} \right) dS' \quad (4.16)$$

$\frac{\cos\theta}{r^2} ds$ is proportional to the solid angle $d\omega$ subtended at point $P(\mathbf{r})$, hence

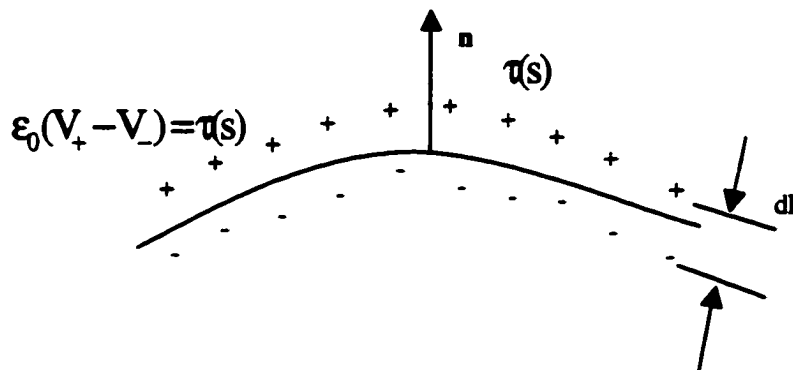


Figure 4.10. Double layer source distribution

$$V(\mathbf{r}) = \frac{1}{4\pi\epsilon_0} \int_S \tau(\mathbf{r}') \cdot \nabla \left(\frac{1}{r} \right) dS = \pm \frac{1}{4\pi\epsilon_0} \int_S \tau d\omega \quad (4.17)$$

where $d\omega$ is the solid angle subtended at point $P(\mathbf{r})$ by surface dS , as show in figure 4.11. The sign \pm depends on which side of the surface S the observation point lies. The main characteristic of the double layer distribution is that the potential is discontinuous across the surfaces. If the surface S is closed and the charge density is uniform then τ can be taken out from the integral. The positive charge lies on the outer side of S in which case τ has the same direction as the positive normal of the surface. As the property of the solid angle

$$\oint d\omega = \begin{cases} 4\pi & P \text{ inside the surface} \\ 0 & P \text{ outside the surface} \end{cases} \quad (4.18)$$

thus

$$V_+ = 0 \quad V_- = -\frac{\tau}{\epsilon_0} \quad (4.19)$$

and

$$V_+ - V_- = \frac{\tau}{\epsilon_0} \quad (4.20)$$

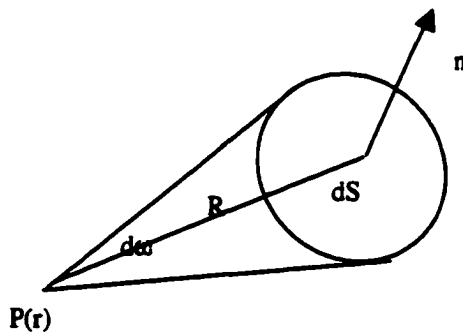


Figure 4.11. Solid angle

The potential undergoes an abrupt change of τ/ϵ_0 when the observation point moves from the inner side to the outer side of a double layer source. The boundary value problem with inhomogeneous boundary conditions of the first kind can be represented by an appropriate distribution of the dipole layer source. The normal component of the field strength is continuous from one side to the other.

$$(\mathbf{E}_+ - \mathbf{E}_-) \cdot \mathbf{n} = 0 \quad \text{or} \quad \frac{\partial V_+}{\partial n} = \frac{\partial V_-}{\partial n} = \frac{\partial V}{\partial n} \Big|_S \quad (4.21)$$

However, the tangential component of \mathbf{E} may be discontinuous, because the potentials undergo an abrupt change on both sides as shown in figure 4.12.

$$V_2 - V_3 = \frac{\tau}{\epsilon_0} \quad (4.22)$$

$$V_4 - V_1 = -\frac{1}{\epsilon_0}(\tau + \nabla \tau \cdot \mathbf{db}) \quad (4.23)$$

$$V_2 - V_1 = \Delta V_+ \quad (4.24)$$

$$V_3 - V_4 = \Delta V_- \quad (4.25)$$

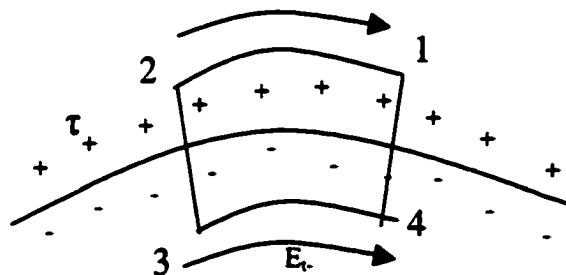


Figure 4.12 Discontinuity of E_t around a double layer source

db is a small length along the surface. Since the sum of the potentials around the loop is zero

$$\sum V_i = 0 \quad (4.26)$$

$$\frac{\tau}{\epsilon_0} - \frac{(\tau + \nabla\tau \cdot db)}{\epsilon_0} + \Delta V_+ - \Delta V_- = 0 \quad (4.27)$$

then

$$\frac{\Delta V_+}{db} - \frac{\Delta V_-}{db} = -\frac{\nabla\tau}{\epsilon_0} \quad (4.28)$$

and

$$E_{t+} - E_{t-} = -\nabla \frac{\tau}{\epsilon_0} \quad (4.29)$$

The abrupt change of E_t produces an abrupt change in E , since the normal component of E is continuous.

$$E_+ - E_- = -\nabla \frac{\tau}{\epsilon_0} \quad (4.30)$$

$\nabla\tau$ is the gradient of τ along the surface. If τ is uniform then E is continuous.

4.3.3. Application of double layer source model to SCC in pipe

In a double layer source model, steps 1 and 3 are the same as in the case of a single layer source model. In step 2, the single layer current source is now replaced by the double layer source model as described in the previous section.

Step 1. Calculation of Velocity Induced Currents

The velocity-induced currents \bar{J}_0 in a defect-free pipe wall due to axial motion of the magnetizer relative to the pipe is calculated, by solving the 2D governing equation

$$\nabla \times \frac{1}{\mu} \nabla \times \bar{\mathbf{A}} = \bar{\mathbf{J}}_s - \sigma \frac{\partial \bar{\mathbf{A}}}{\partial t} + \sigma \bar{\mathbf{v}} \times \nabla \times \bar{\mathbf{A}} \quad (4.31)$$

Step 2. Calculation of Perturbation Current by SCC

This step models a 3D region with an SCC. The SCC is characterized by a double layer source. In the double layer source model, the defect is represented by 2 layers of equal and opposite charges. The tight crack of infinitesimal width is modeled by using the same physical coordinates for the nodes on the two surfaces of crack, A and B shown in figure 4.13. Neuman boundary conditions are applied on the two sides of the crack as

$$\left. \frac{\partial V}{\partial n} \right|_i = -\frac{\bar{\mathbf{J}}_0}{\sigma} \text{ on A} \quad \left. \frac{\partial V}{\partial n} \right|_i = \frac{\bar{\mathbf{J}}_0}{\sigma} \text{ on B} \quad (4.32)$$

The Laplace equation $\nabla^2 V = 0$ is solved to give a first approximation of the perturbation currents $\bar{\mathbf{J}}_p$ in the pipe wall section with an axial SCC. The perturbation currents due to two parallel SCCs is shown in figure 4.14, (a) side view and (b) top view. Total current (background + perturbation current) is shown in figure 4.14, (c) side view and (d) top view.

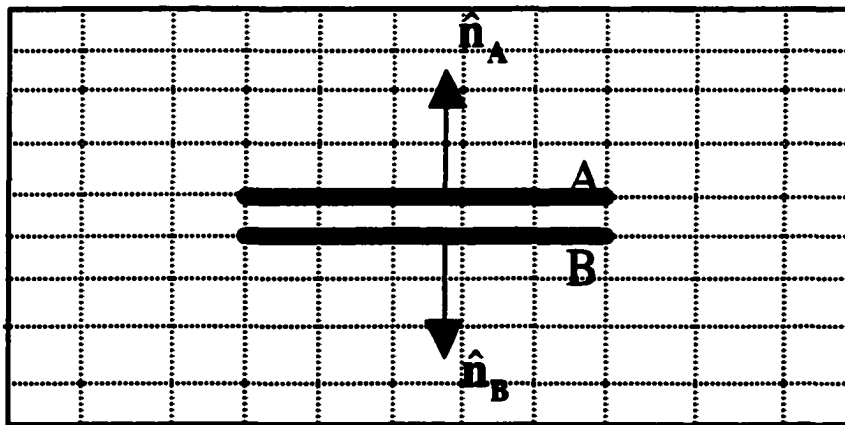


Figure 4.13. Double layer source model

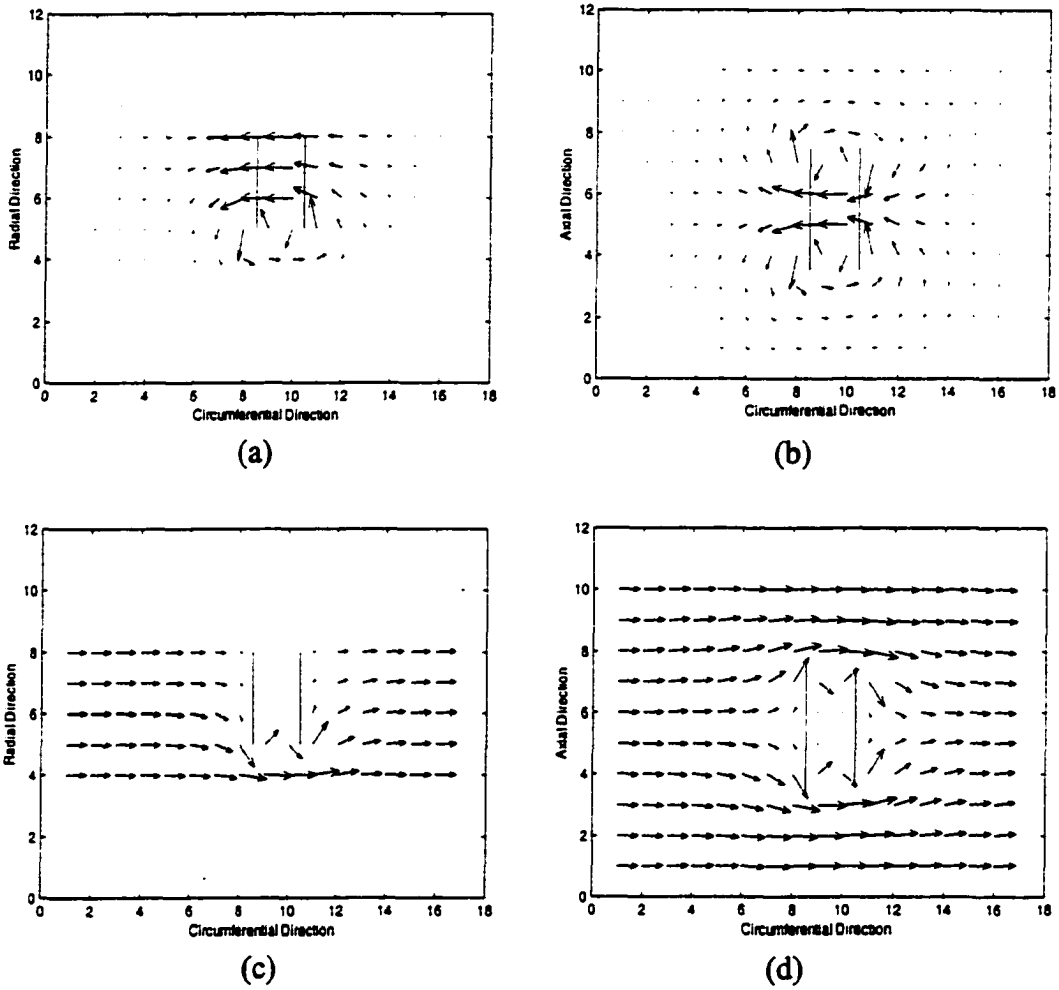


Figure 4.14. Step 2 results using double layer source model, perturbation current
(a) side view (b) top view, total current (background + perturbation current) (c) side view (d) top view

Step3. Calculation of Current Perturbation Fields

The results obtained in step 2 are used to solve for the perturbation fields that can then be measured using a coil. The governing equation in this step is

$$\nabla \times \frac{1}{\mu} \nabla \times \bar{A} = \bar{J}_p \quad (4.33)$$

Multiple and arbitrary SCCs can be modeled by the double layer source model. However, the double layer source model uses the full geometry. Hence, it is computationally intensive. In the following section, a numerical method will be discussed which reduces the computation time and storage requirement.

4.4 Substructure Method

In general, a three dimensional finite element method of a field problem is extremely computation intensive. The problem arises due to the large area of the geometry and small region of the crack that has to be meshed appropriately. In this work, the geometry consists of a 24 inch diameter pipe of wall thickness 0.34 inch in which narrow cracks are introduced. With a mesh discretization of 20x20x16 and bandwidth of 464, the matrix size to be inverted at each time step is 3276273. Computation time for each run is around 3.5 hours. Hence there is a need for optimizing the computational procedure. In the substructure method [32] [33], first the entire domain is divided into several parts which are connected to each other by a finite number of nodes. The elements of the matrices of each sub part are assembled into a submaster matrix. These submaster matrices for each part are similar to the matrices for an element and in fact, each part can be viewed as a superelement or a substructure [34]. The decomposition of the region into subregions so that changes at each time step is restricted to

a single subregion, significant computational savings can be achieved. The details of implementation are given below:

STEP 1. Suppose a region of interest, Ω is divided into two regions, Ω_I and Ω_{II} as shown in figure 4.15, where Ω_{II} consist of all the areas where the material property parameters have to be modified in successive solution steps and where the calculation result at each step should be recorded, Ω_I is the complement of Ω_{II} . C denotes the interface between the two regions. In mesh generation for Ω , element numbers are obtained by first numbering the elements of Ω_I then the elements in Ω_{II} .

The local matrices for the substructures Ω_I and Ω_{II} can be written as

$$K_I = \begin{bmatrix} K_{I I} & K_{I C} \\ K_{C I} & K_{C C}^I \end{bmatrix}_{N_I \times N_I} \quad (4.34)$$

$$K_{II} = \begin{bmatrix} K_{II CC} & K_{C II} \\ K_{II C} & K_{II II} \end{bmatrix}_{N_{II} \times N_{II}} \quad (4.35)$$

where $K_{I I}$ and $K_{II II}$ are the submatrices corresponding to Ω_I and Ω_{II} excluding the nodes on the interface C . $K_{C C}^I$ and $K_{C C}^{II}$ are the submatrices for the nodes on the interface C from the side of Ω_I and Ω_{II} respectively. The corresponding right hand terms are:

$$P_I = \begin{bmatrix} P_{I0} \\ P_C^I \end{bmatrix}_{N_I} \quad (4.36)$$

$$P_{II} = \begin{bmatrix} P_C^{II} \\ P_{II0} \end{bmatrix}_{N_{II}} \quad (4.37)$$

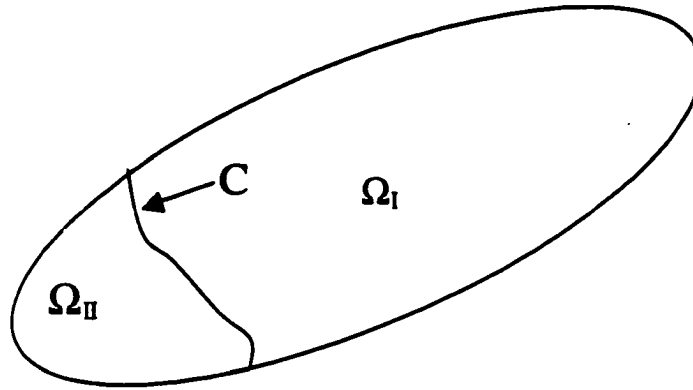


Figure 4.15, Sub-region Ω_I and Ω_{II} .

where P_{I0} and P_{II0} are loading vectors for nodes corresponding to Ω_I and Ω_{II} excluding the nodes on C . P_C^I and P_C^{II} are loading vectors for nodes on C assembled from the side of Ω_I and Ω_{II} . The global matrix for the entire region is of the following form:

$$\begin{bmatrix} K_{II} & K_{Ic} & 0 \\ K_{cI} & K_{cc} & K_{cII} \\ 0 & K_{IIc} & K_{IIII} \end{bmatrix}_{N \times N} \begin{bmatrix} V_{I0} \\ V_c \\ V_{II0} \end{bmatrix}_N = \begin{bmatrix} P_{I0} \\ P_c \\ P_{II0} \end{bmatrix}_N \quad (4.38)$$

where V_{I0} , V_{II0} and V_c are the unknowns in Ω_I , Ω_{II} and C respectively. N is the total number of equations ($N=N_I+N_{II}+N_C$).

$$K_{cc} = K_{cc}^I + K_{cc}^{II} \quad (4.39)$$

$$P_c = P_c^I + P_c^{II} \quad (4.40)$$

However, in the substructure method it is not necessary to assemble the global matrix in each step.

STEP 2. Eliminating V_{10} result in equation 4.38, we get

$$\begin{bmatrix} I & K_{II}^{-1}K_{IC} & 0 \\ 0 & K_{CC}^i + K_{CC}^{\Pi} & K_{C\Pi} \\ 0 & K_{\Pi C} & K_{\Pi\Pi} \end{bmatrix}_{N \times N} \begin{bmatrix} V_{10} \\ V_C \\ V_{\Pi 0} \end{bmatrix}_N = \begin{bmatrix} K_{II}^{-1}P_{10} \\ P_C^i + P_C \\ P_{\Pi 0} \end{bmatrix}_N \quad (4.41)$$

where

$$K_{CC}^i = K_{CC}^I - K_{IC}^T K_{II}^{-1} K_{IC} \quad (4.42)$$

$$P_C^i = P_C^I - K_{IC}^T K_{II}^{-1} P_{10} \quad (4.43)$$

The equation (4.41) can be written as two equations.

$$I V_{10} + K_{II}^{-1} K_{IC} V_C = K_{II}^{-1} P_{10} \quad (4.44)$$

$$\begin{bmatrix} K_{CC}^i + K_{CC}^{\Pi} & K_{C\Pi} \\ K_{\Pi C} & K_{\Pi\Pi} \end{bmatrix}_{N_{II} \times N_{II}} \begin{bmatrix} V_C \\ V_{\Pi 0} \end{bmatrix}_{N_{II}} = \begin{bmatrix} P_C^i + P_C \\ P_{\Pi 0} \end{bmatrix}_{N_{II}} \quad (4.45)$$

STEP 3. Store K_{CC}^i and P_C^i in the secondary storage for further usage, since these matrices do not change with changes in Ω_{II} .

This substructure method can reduce both computational resource and time. In the next chapter, numerical results of implementation are discussed with both single layer source models and the double layer source model with a substructure method.

CHAPTER V. RESULTS AND DISCUSSION

5.1. Single Layer Source Model

5.1.1. Single SCC

The overall implementation of the four step procedure is described in figure 5.1. The inspection geometry used in the implementation of the FE model is shown in figure 5.2. The magnetizer and the pick-up sensor move at a fixed velocity of 5 m per second inside a pipe of wall thickness 9 mm. In the absence of defects, the geometry is axisymmetric and, hence, a 2D model is used in implementing step 1 to calculate the velocity-induced currents in each time step.

In steps 2 and 3, the boxed section around the axial SCC is modeled in three dimensions using the source currents obtained in step 1. The sensor is a single turn coil of dimension $2.45\text{cm} \times 6.25\text{cm}$, located in the remote field (30 cm behind the magnetizer) and 0.1 cm below the inner pipe wall. The plane of the coil is perpendicular to the axis of pipe. The resulting defect signals are calculated in terms of the voltage induced in a single turn coil by the axial component of the perturbation fields. Parametric studies are conducted for the different defect parameters (length and depth) and different sensor positions (axial and circumferential).

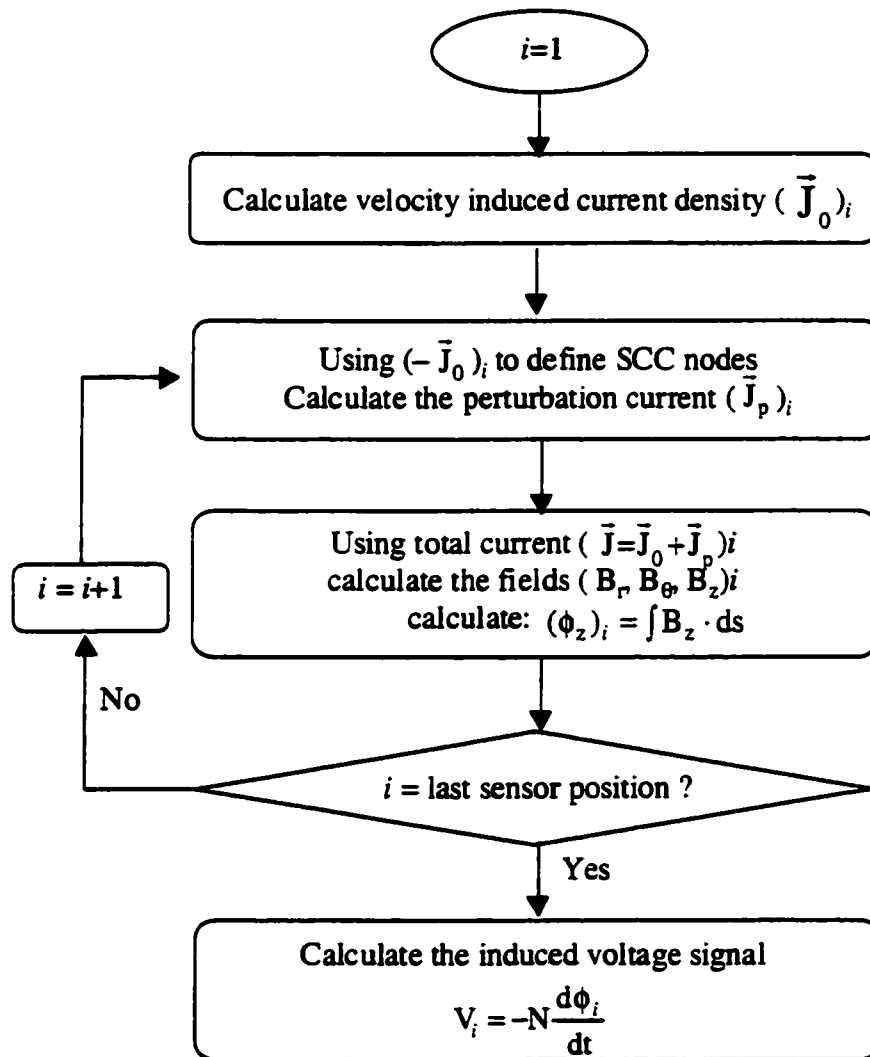


Figure 5.1. Flow chart of the four-step procedure

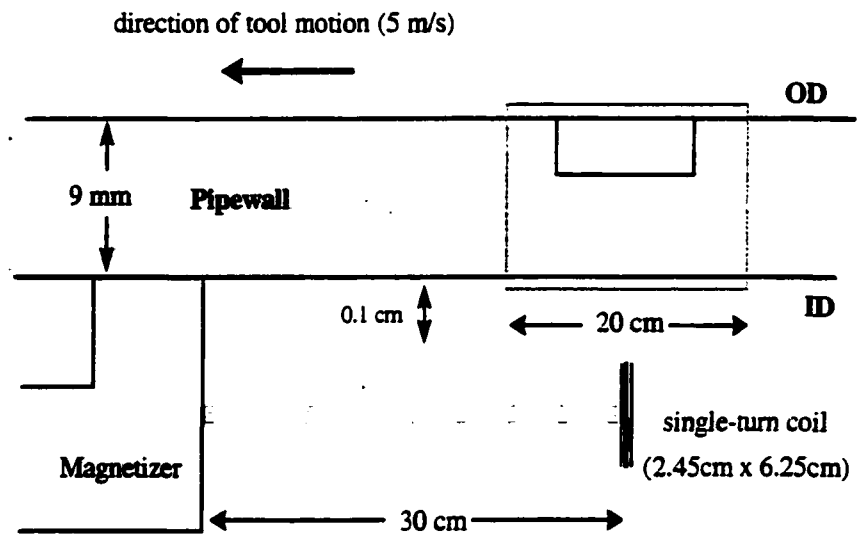


Figure 5.2. Geometry used in the simulation

(a) Signal variation with defect depth

The signal due to a defect depth with a fixed defect length (8 cm) and varying depths was calculated. The defect depths were 20 %, 40 %, 60% and 80% of pipewall thickness. The voltage signal, as a function of depth of the SCC is shown in figure 5.3. The peaks occur at the SCC edges. The peak-to-peak value plotted as a function of flaw depth in figure 5.4, show an exponential variation.

(b) Signal variation with defect length

The effect of varying defect lengths with a fixed defect depth (60% of pipewall) were calculated. Four different defect lengths (2 cm, 4 cm, 6 cm, and 8 cm) were chosen. The voltage signals obtained with various axial lengths of SCC are plotted in Figure 5.5. The peak-to-peak value plotted as a function of defect length in figure 5.6. The results show a monotonic increase in the peak value of the signal with defect length.

(c) Signal variation with circumferential sensor position

The max signals due to a defect size are obtained when the sensor coil is directly under the flaw. The voltage signals obtained at other circumferential positions of the coil show a reduction in magnitude. The voltage signals at 0° , 7.9° , 15.8° , and 23.7° are plotted in figure 5.7. The peak-to-peak value plotted in figure 5.8 as a function of the angular distance between the defect and coil position show a reduction in the peak amplitude of the signal.

(d) Signal variation with axial sensor position

The axial sensor position in the above parametric studies was 30 cm behind the magnetizer. The voltage signals obtained at different axial sensor positions of 10 cm, 20 cm, 30 cm and 40 cm behind the magnetizer are plotted in figure 5.9. The voltage signal is larger when the sensor is close to the magnetizer. However, the signal due to the sensor position at 10 cm is distorted significantly, due to an interaction with the primary fields of the magnets.

(e) Signal comparison due to different velocity

The effects of tool velocity on signals due to different defect depths and different circumferential sensor positions were calculated. The peak-to-peak values of the signal due to different defect depths with velocity 3 m/s and 5 m/s are plotted in figure 5.10. The signal magnitude is seen to be higher at velocity. Since the velocity induced currents are higher. Figure 5.11 shows the peak-to-peak value as a function of circumferential sensor position with different velocity.

The parametric studies show that the peaks occur at the edges of the defect and the sensor has maximum sensitivity when it is positioned directly under the defect. It is also shown that the sensitivity of the sensor is increased as the velocity is increased. These results should be taken into consideration in the tool design.

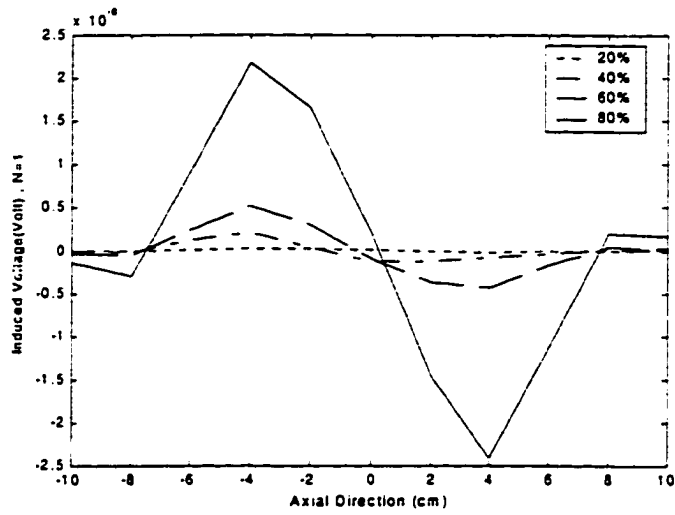


Figure 5.3. Induced voltage measured for defects of different depths

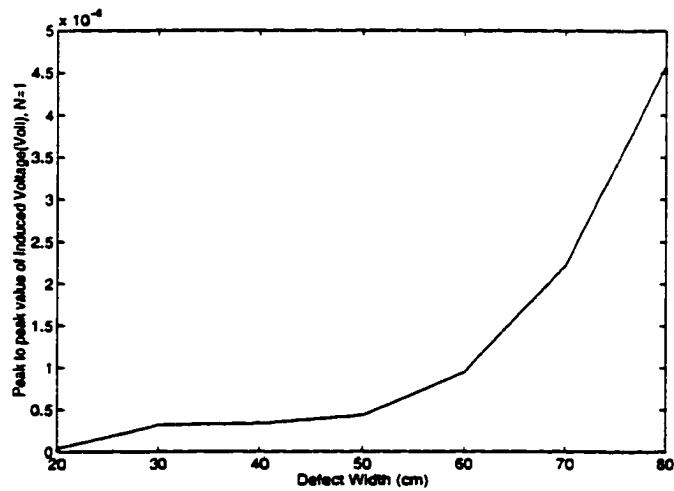


Figure 5.4. Peak to peak value of induced voltage as a function of defect depths

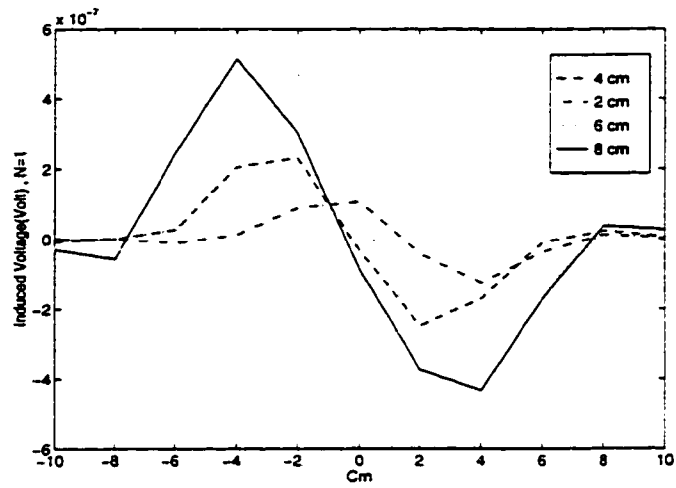


Figure 5.5. Induced voltage measured for defects of different lengths (60% depth)

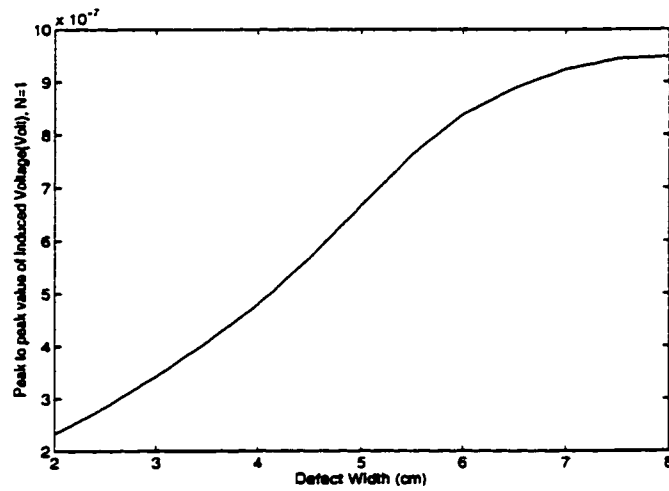


Figure 5.6. Peak to peak value of induced voltage as a function of defect lengths (60% depth)

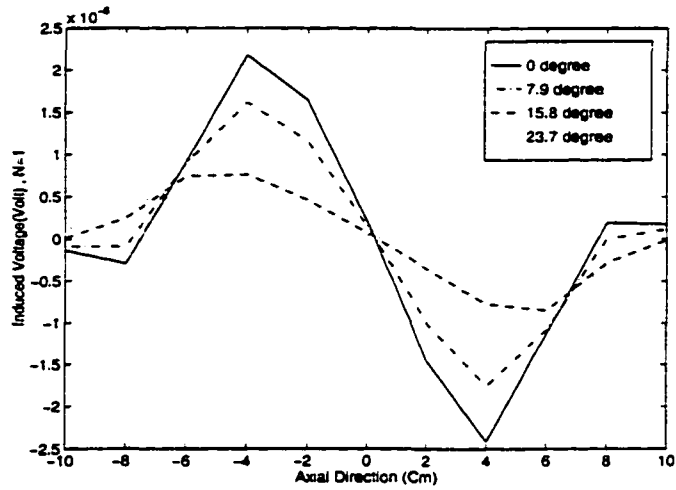


Figure 5.7. Induced voltage measured at different circumferential coil position (60% depth)

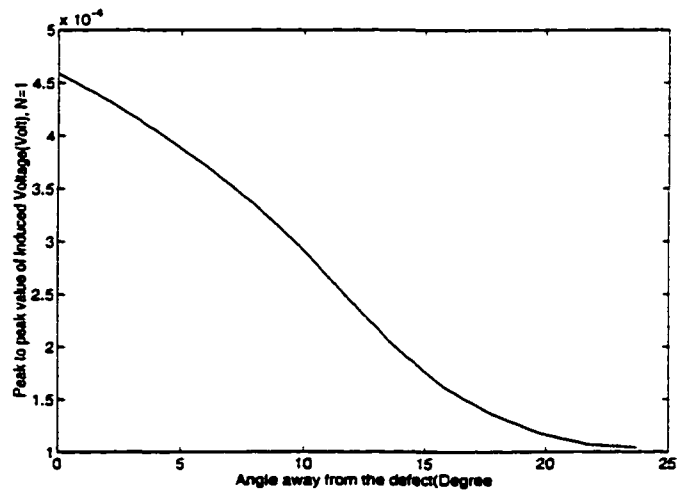


Figure 5.8. Peak to peak value of induced voltage as a function of different circumferential coil position (60% depth)

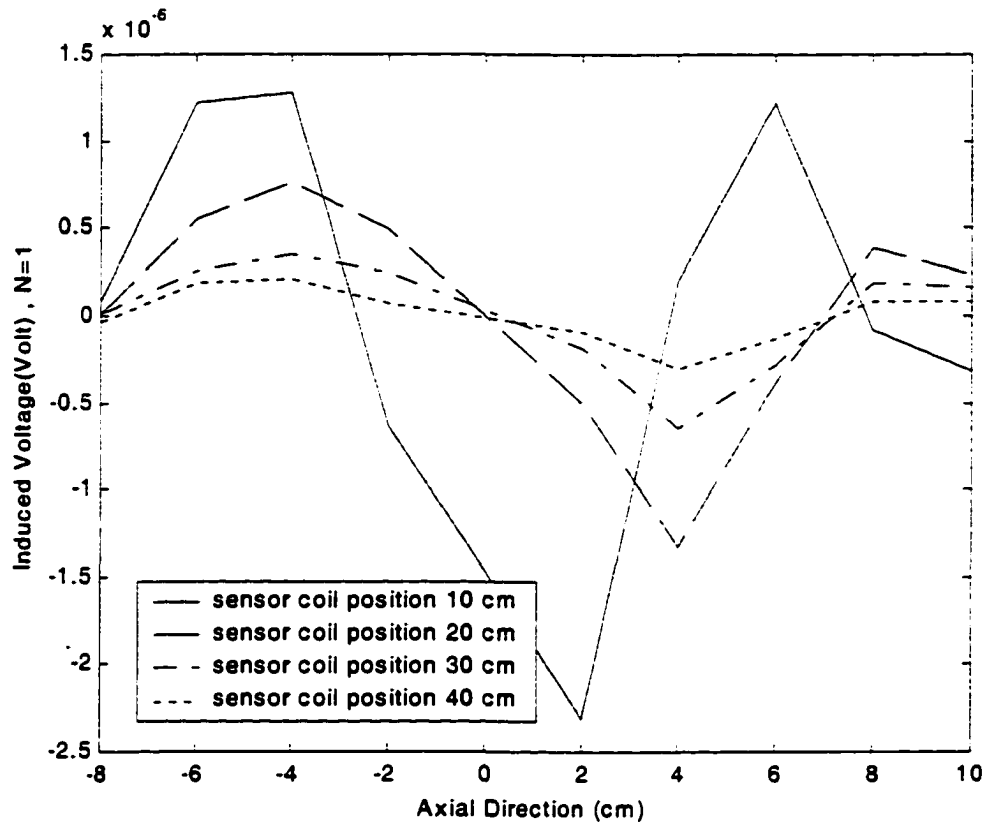


Figure 5.9. Peak to peak value of induced voltage as a function of different axial coil position (60% depth, 8cm length)

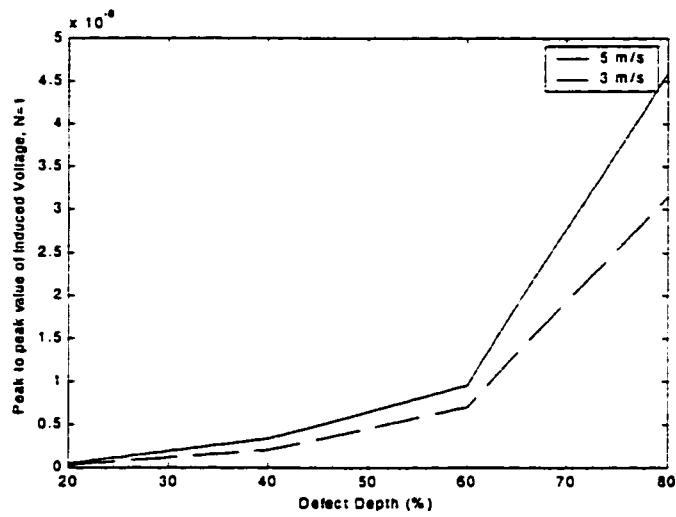


Figure 5.10. Peak to peak value of induced voltage as a function of defect depths with velocity (3 m/s and 5 m/s)

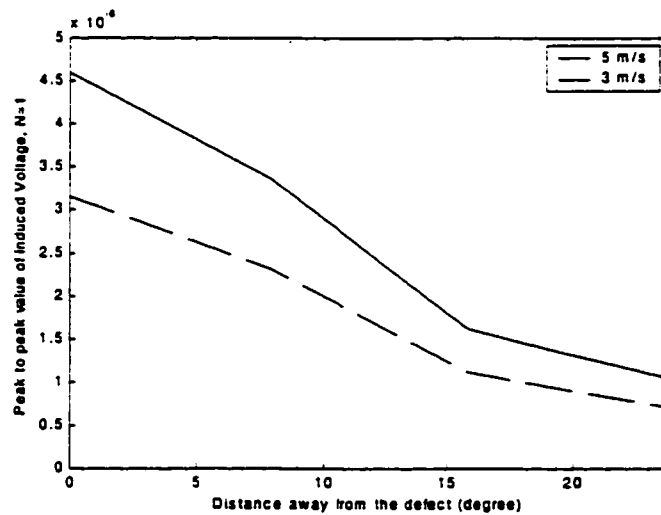


Figure 5.11. Peak to peak value of induced voltage as a function of different circumferential coil position (60% depth) with velocity (3 m/s and 5 m/s)

5.1.2. Multiple SCC by Superposition method

Results presented in the previous section are due to a single defect. The SCC, however, generally occur in colonies. The simplest way to model multiple defects is to utilize the superposition principle. The current perturbation method discussed in chapter 4 is modeled in the remote region where linearity assumed. In this case, the superposition method was used to approximate the multiple defect case. Two parallel defects (8cm long, 80 % depth) are used in the simulation of the superposition method. Figure 5.12 shows the signal due to two parallel defects as a function of circumferential distance between the defects. The signal due to two parallel defects with both circumferential distance and axial distance are shown in figure 5.13. Finally a colony of parallel SCCs were simulated. In the first example, 7 defects all of the same depth (60%) and different length (two 2 cm, three 4 cm, one 6 cm and one 8 cm) as shown in figure 5.14 (a) were modeled and the resulting signal is shown in figure 5.14 (b). In the second example, six different defects in figure 5.15 (a) were chosen and all defect dimensions are summarized in table 5.1. Figure 5.15 (b) shows the resulting signal. Figure 5.16 (a) shows a colony with 7 defects with dimensions summarized in table 5.1. Figure 5.16 (b) shows the resulting signal.

5.2. Double Layer Source Model

This section presents results of implementing the double layer source model described in chapter 4.3 for multiple SCCs. The inspection geometry used in the implementation of the double layer source model is the same as the single layer source model which is shown in figure 5.2.

Table 5.1. Defect profile for each case of the superposition method

| Case | Defect No. | Defect Length (cm) | Defect Depth (%) | Location | |
|--------|------------|--------------------|------------------|------------------------------|---------------------|
| | | | | Circumferential position (m) | Axial position (cm) |
| Case 1 | 1 | 4 | 60 | 0.0625 | -4 ~ 0 |
| | 2 | 4 | 60 | 0.03125 | 2 ~ 6 |
| | 3 | 8 | 60 | 0 | -4 ~ 4 |
| | 4 | 2 | 60 | 0 | 6 ~ 8 |
| | 5 | 6 | 60 | -0.03125 | -6 ~ 0 |
| | 6 | 2 | 60 | -0.03125 | 2 ~ 4 |
| | 7 | 4 | 60 | -0.0625 | 0 ~ 4 |
| Case 2 | 1 | 8 | 60 | 0.0625 | -8 ~ 0 |
| | 2 | 2 | 60 | 0.03125 | 4 ~ 6 |
| | 3 | 2 | 60 | 0 | -6 ~ -4 |
| | 4 | 4 | 60 | 0 | -2 ~ 2 |
| | 5 | 4 | 60 | -0.03125 | -8 ~ -4 |
| | 6 | 6 | 60 | -0.0625 | 0 ~ 6 |
| Case 3 | 1 | 4 | 60 | 0.0625 | -8 ~ -4 |
| | 2 | 2 | 60 | 0.0625 | 6 ~ 8 |
| | 3 | 2 | 60 | 0.03125 | -8 ~ -6 |
| | 4 | 4 | 80 | 0.03125 | -4 ~ 4 |
| | 5 | 2 | 60 | 0 | 0 ~ 2 |
| | 6 | 6 | 60 | -0.03125 | -8 ~ -2 |
| | 7 | 4 | 60 | -0.03125 | 4 ~ 8 |

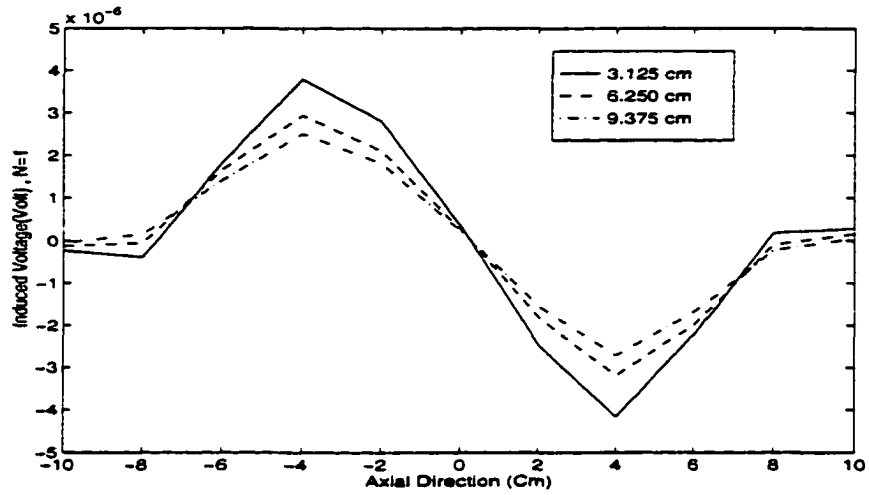


Figure 5.12. Signal due to two parallel defect as a function of circumferential distance (8 cm long, 80% depth)

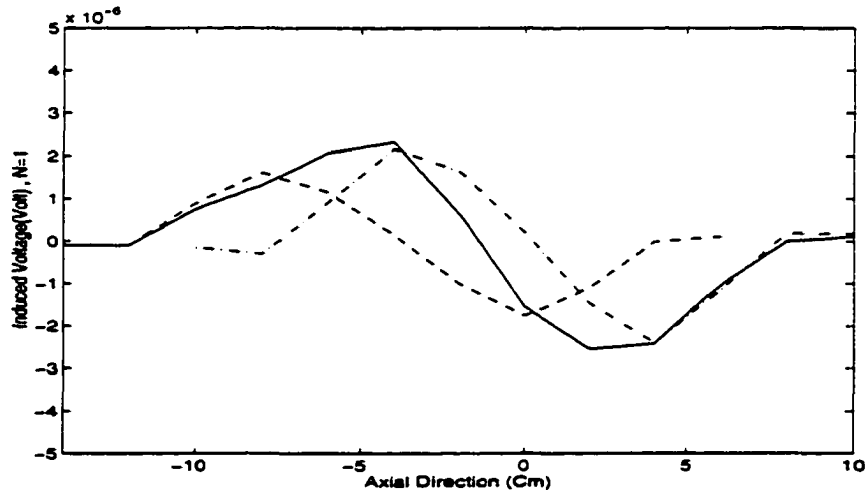
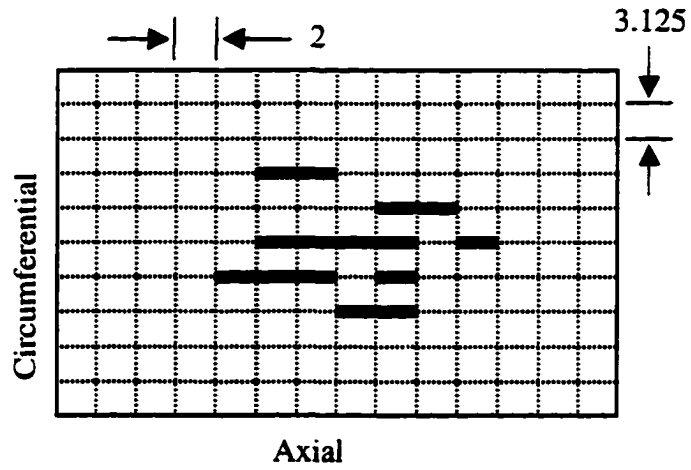
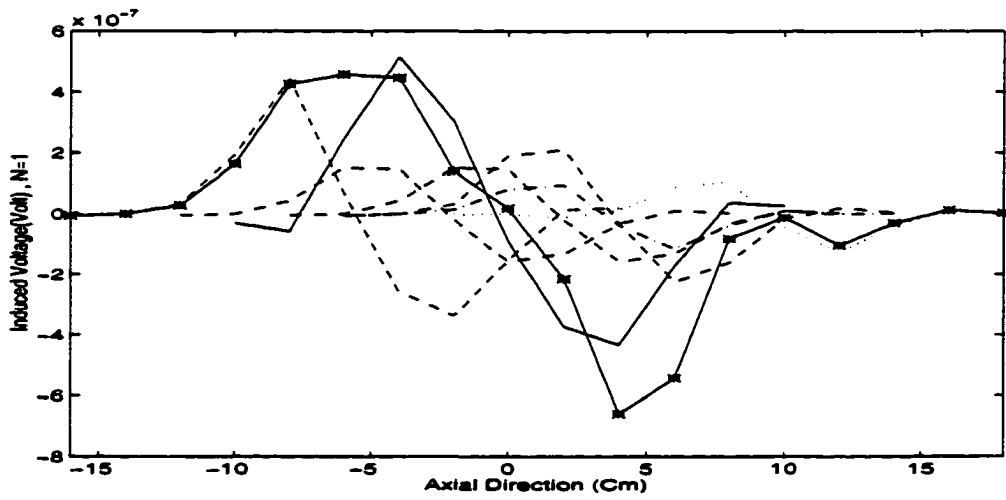


Figure 5.13. Signal due to two parallel defect with distance of both circumferential and axial (8 cm long, 80 % depth)

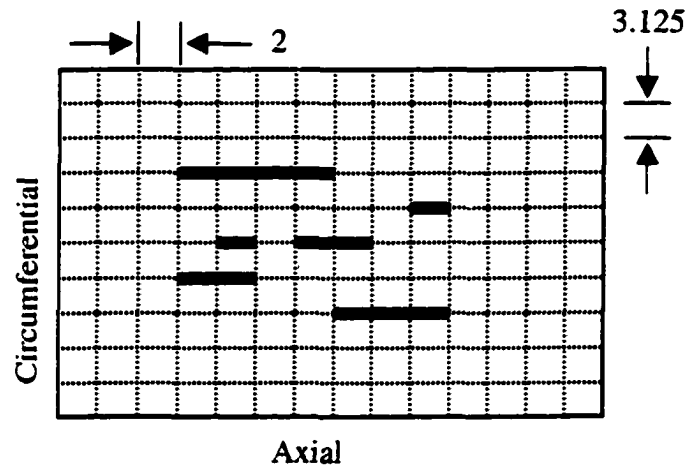


(a)

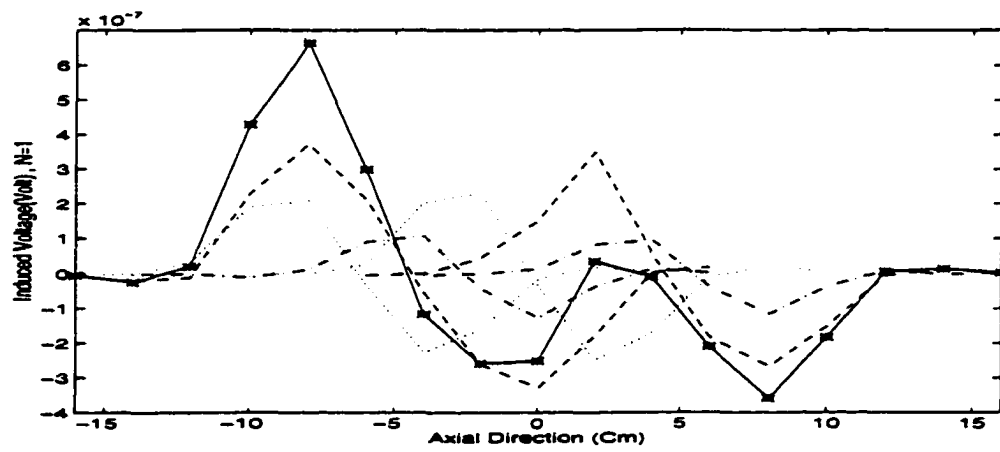


(b)

Figure 5.14. Case 1 defect profile (a) and resulting signal (b)

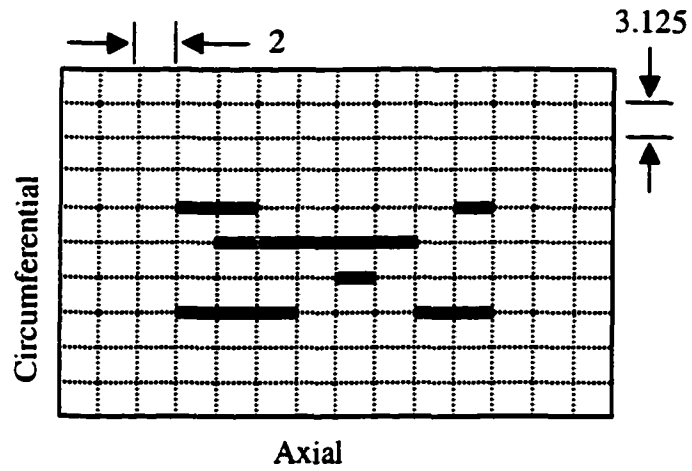


(a)

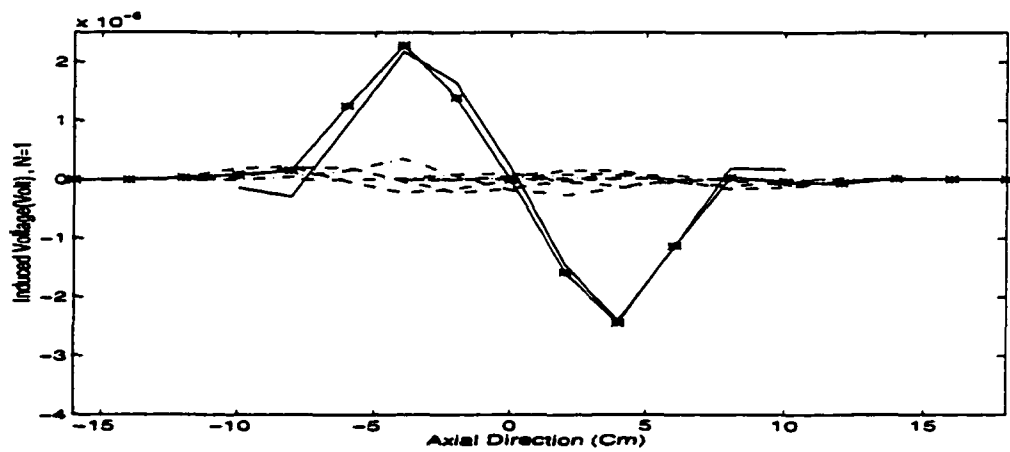


(b)

Figure 5.15. Case 2 defect profile (a) and resulting signal (b)



(a)



(b)

Figure 5.16. Case 3 defect profile (a) and resulting signal (b)

(a) Comparison of single and double layer source model

In order to validate the double layer source model, the signal from a single SCC was compared to that obtained from single layer source model. Figure 5.17 shows the resulting signals of symmetric model (solid line) and double layer source model (dotted line) due to an SCC of 8 cm length and 60% depth. The peaks of the signal occur at the SCC edges. The two predictions are seen to be identical indicating the equivalence of the two models.

(b) Nonparallel SCC

One of the limitations of the single layer source model with superposition is the inability to model defects at angle to each other. The double layer source model is asymmetric and can be used for simulating arbitrary defect colonies. In the first example, we next consider a single SCC at an angle to the pipe axis. In this case, the Neuman boundary conditions are given as follow.

$$\left. \frac{\partial V}{\partial n} \right|_i = -\frac{\bar{J}_0}{\sigma} \cos\theta \quad (5.1)$$

where θ shown in figure 5.18 is the angle between the normal direction \mathbf{n} and projected normal direction \mathbf{n}' . The mesh for the angular defect is shown in figure 5.19. In this case, the defect is at an angle of 26 degrees. Figure 5.20 shows the reduction in the induced voltage due to the angle. The solid line is the signal from the defect exactly orthogonal to current and the dotted line is a signal from the angled crack. Figure 5.21 shows the signals as a function of different angles.

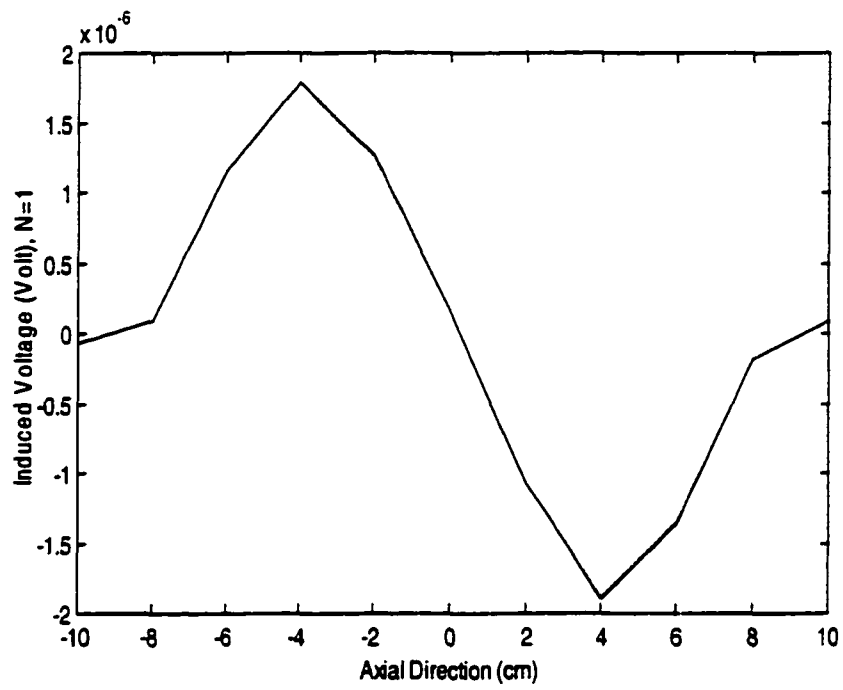


Figure 5.17. Comparison of symmetric model and double layer source model

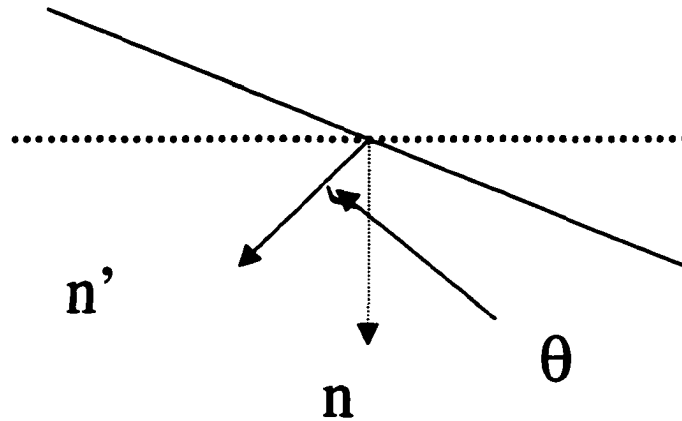


Figure 5.18. Angle θ between the normal direction n to the parallel defect and normal direction n' to the angular defect

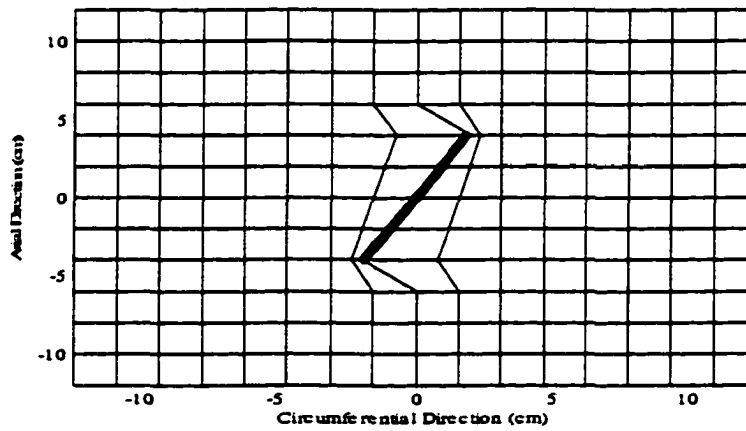


Figure 5.19. Mesh for angular defect

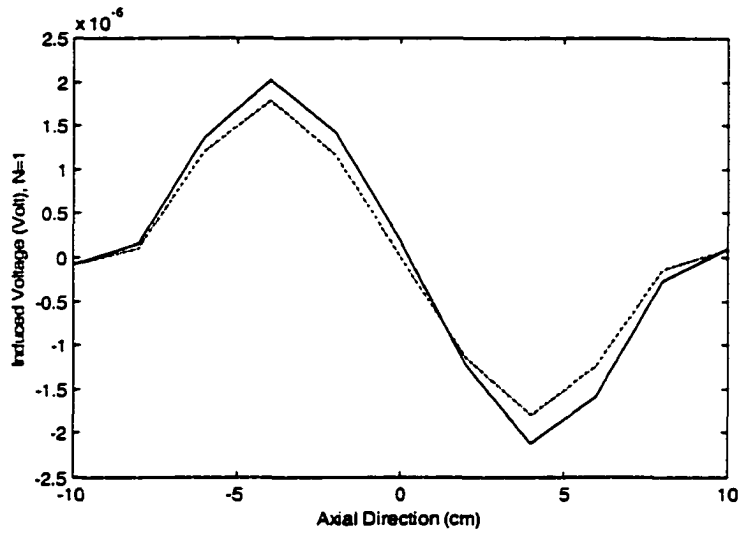


Figure 5.20. Induced voltage for parallel and angular defect

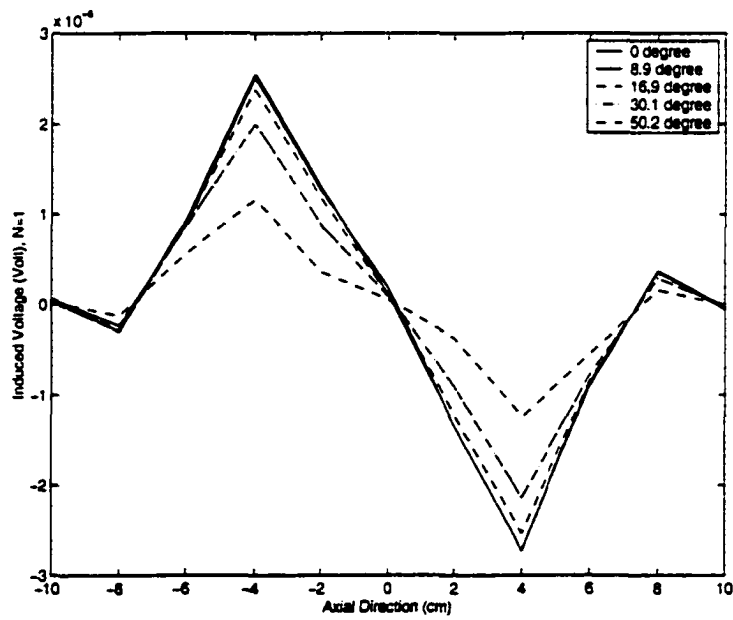


Figure 5.21. Induced voltage signals as a function of different angles

(c) Comparison of superposition model and double layer source model

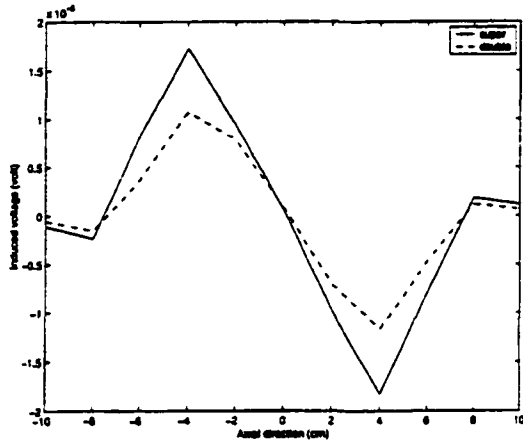
The results of the superposition model and double layer source model is compared for two parallel defects each of 60% depth and 8 cm length. The models were compared for the case of different circumferential defect distances separating the two cracks. The resulting signals with different distance (4mm, 8mm, 2.4 cm and 4 cm) are shown in figure 5.22 (a), (b), (c) and (d) respectively. The signal differences between superposition model and double layer source model decreases as the distance between the defects is increased, indicating that the superposition model is only valid when the two cracks are at least 4 cm apart.

(d) Mutual interactions between the cracks

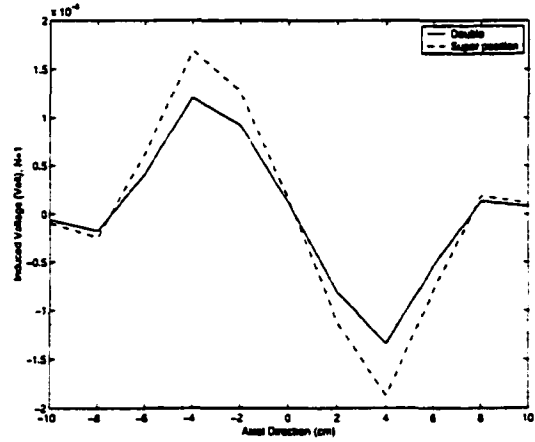
In the double layer source model, the resulting signals for the two parallel defects are calculated by using the same Neuman boundary condition in step2 at both defect nodes. However, we need to consider the mutual interactions between the cracks. To do this, first, perturbation currents are calculated for one of the two parallel defects. The resulting perturbation current is given as Neuman boundary condition for the second defect. Figure 5.23 shows the resulting signal for two parallel defects with circumferential distances (8 mm and 4 cm) between the defects. Each defect is 8 cm length and 60% depth of the pipewall. The mutual interactions effects are higher when the distance between the defects is small. However, the mutual interactions effect is quite negligible and can be ignored.

(e) Multiple SCCs

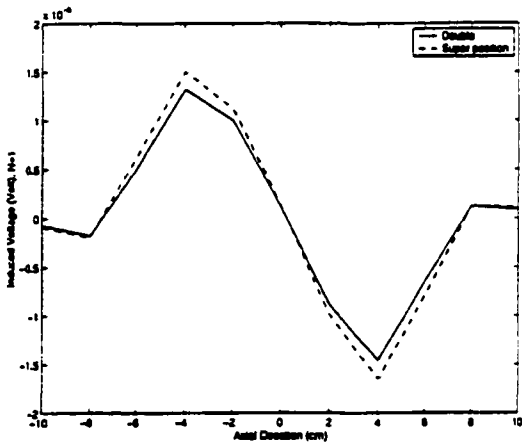
Four different SCC colony cases were tested. Table 5.2 shows the defect profile for each case. In case1, there are four defects as shown in figure 5.24 (a) and the resulting signal



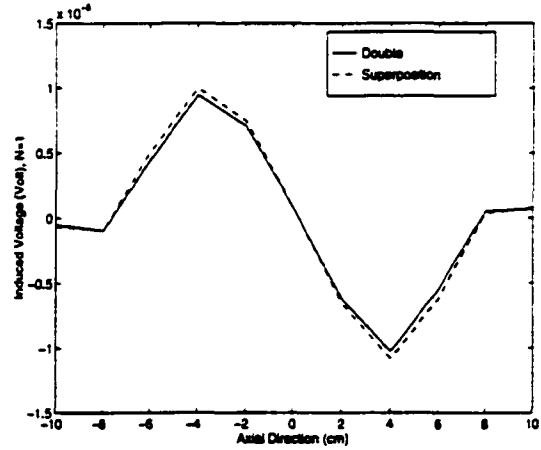
(a)



(b)

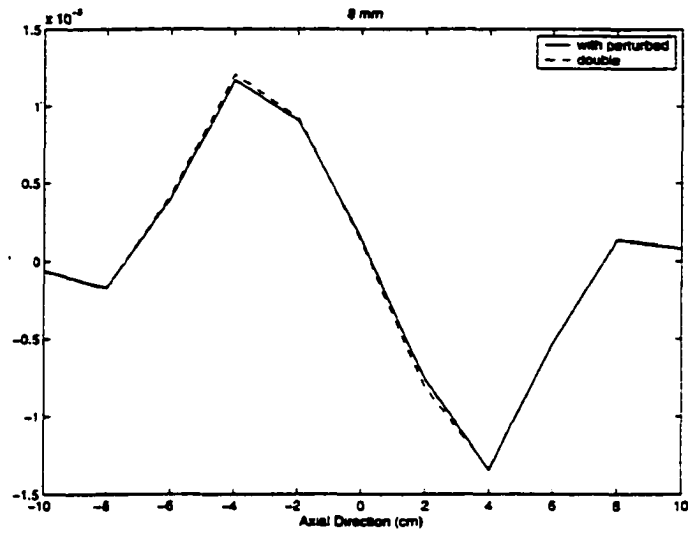


(b)

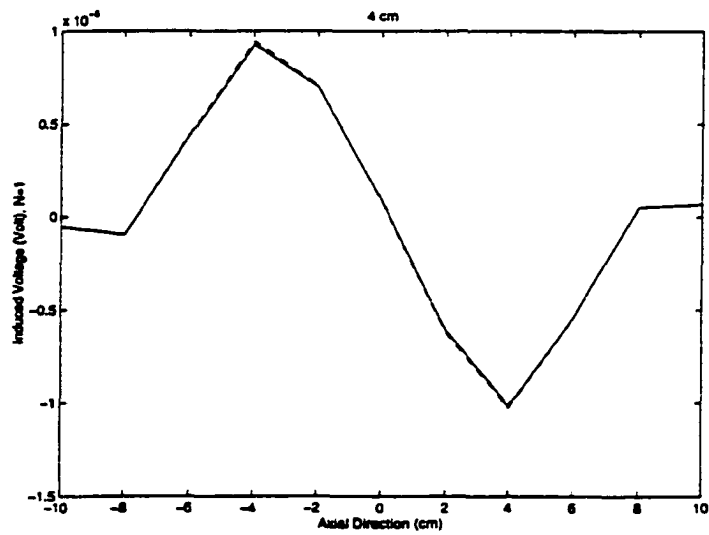


(d)

Figure 5.22. Comparison between superposition model and double layer source model with the different circumferential distance between the two parallel defects
 (a) 4 mm (b) 8 mm (c) 2.4 cm and (d) 4 cm



(a)



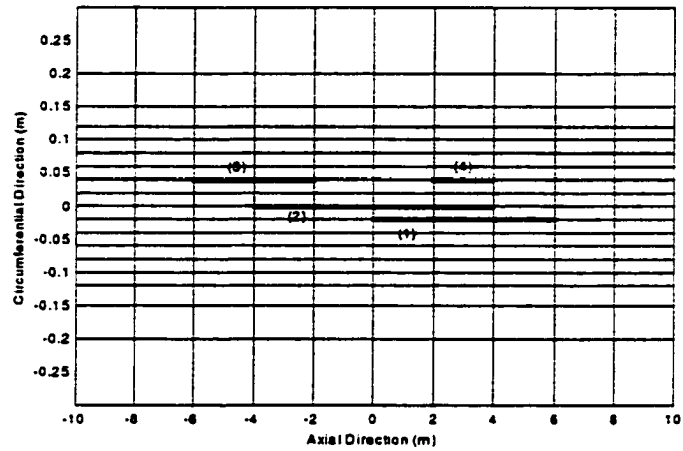
(b)

Figure 5.23. Mutual interaction effect between the two parallel cracks at circumferential distance (a) 8 mm and (b) 4 cm

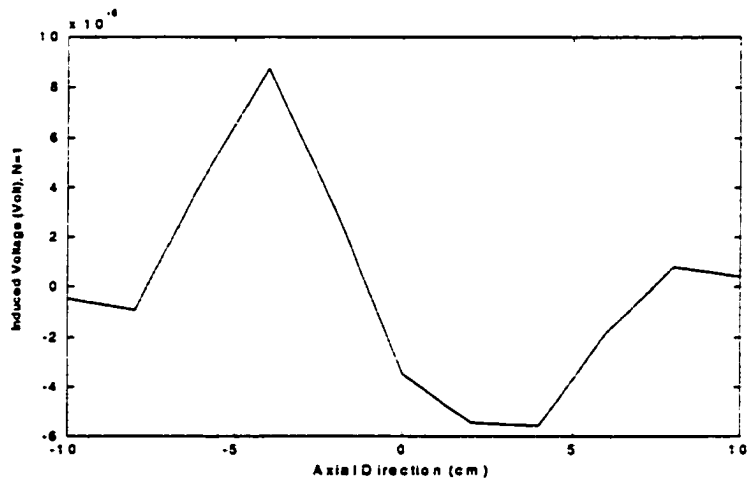
is shown in figure 5.24 (b). Eight defects are shown in figure 5.25 (a) for case 2 and the resulting signal is shown in figure 5.25 (b). Unlike cases 1 and 2 which have only defects parallel to the pipe axis, case 3 has defects at angle to the pipe axis as shown in figure 5.26 (a). The resulting signal is shown in figure 5.26 (b). Case 4 has a combining of angular defect and two parallel defects as shown in figure 5.27 (a). The resulting signal is shown in figure 5.27 (b).

Table 5.2. Defect profile for each case

| Case | Defect No. | Defect Length (cm) | Defect Depth (%) | Defect Angle (degree) | Location | |
|--------|------------|--------------------|------------------|-----------------------|-----------------------------|---------------------|
| | | | | | Circumferential Positon (m) | Axial Position (cm) |
| Case 1 | 1 | 6 | 20 | 0 | -0.02 | 0 ~ 6 |
| | 2 | 8 | 60 | 0 | 0.0 | -4 ~ 4 |
| | 3 | 4 | 40 | 0 | 0.004 | -6 ~ -2 |
| | 4 | 2 | 80 | 0 | 0.004 | 2 ~ 4 |
| Case 2 | 1 | 8 | 60 | 0 | -0.04 | -2 ~ 6 |
| | 2 | 4 | 40 | 0 | -0.02 | 2 ~ 6 |
| | 3 | 4 | 40 | 0 | 0.0 | -4 ~ 0 |
| | 4 | 2 | 80 | 0 | 0.0 | 2 ~ 4 |
| | 5 | 6 | 60 | 0 | 0.002 | -2 ~ 4 |
| | 6 | 8 | 60 | 0 | 0.004 | -6 ~ 2 |
| Case 3 | 1 | 8 | 60 | 11.31 | 0.0 | -4 ~ 4 |
| | 2 | 4 | 60 | 14.03 | 0.0 | 0 ~ 4 |
| Case 4 | 1 | 4 | 60 | 16.7 | -0.02 | 0 ~ 4 |
| | 2 | 8 | 40 | 0 | 0.0 | -4 ~ 4 |
| | 3 | 6 | 60 | 0 | 0.002 | 0 ~ 6 |

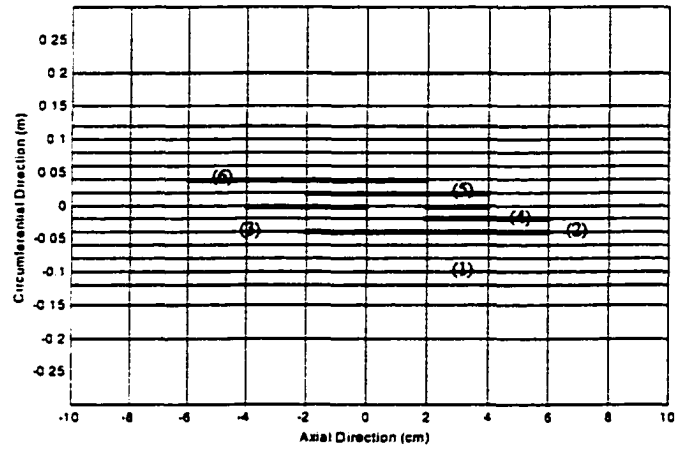


(a)

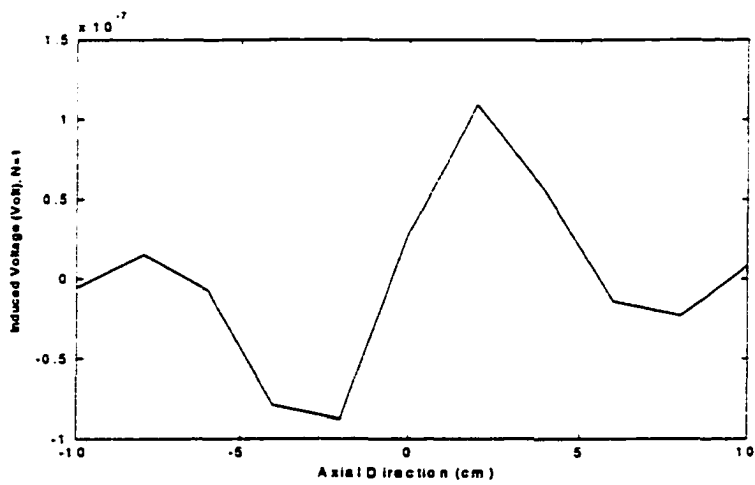


(b)

Figure 5.24. Case 1 (a) defect profile and (b) induced voltage signal

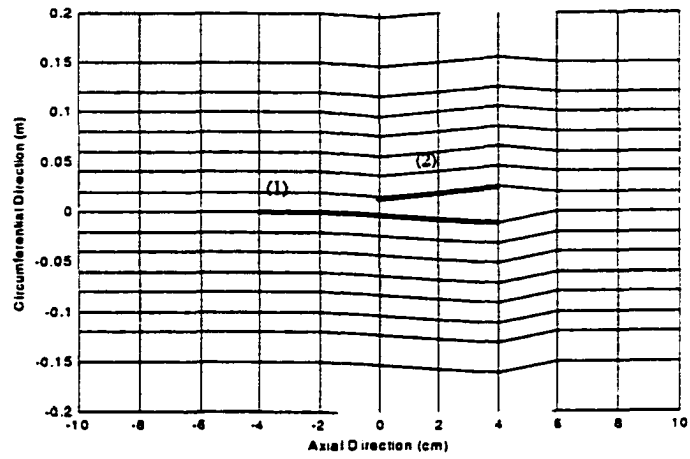


(a)

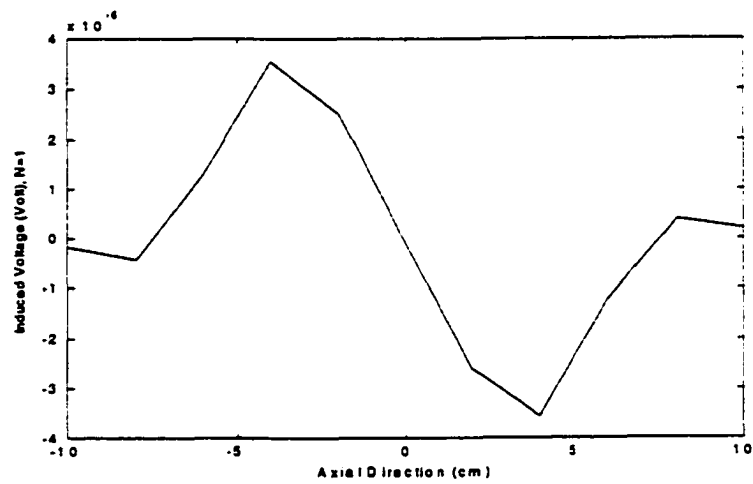


(b)

Figure 5.25. Case 2 (a) defect profile and (b) induced voltage signal

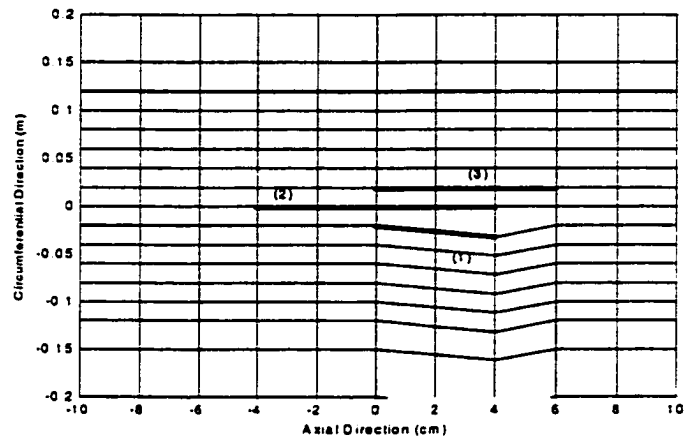


(a)

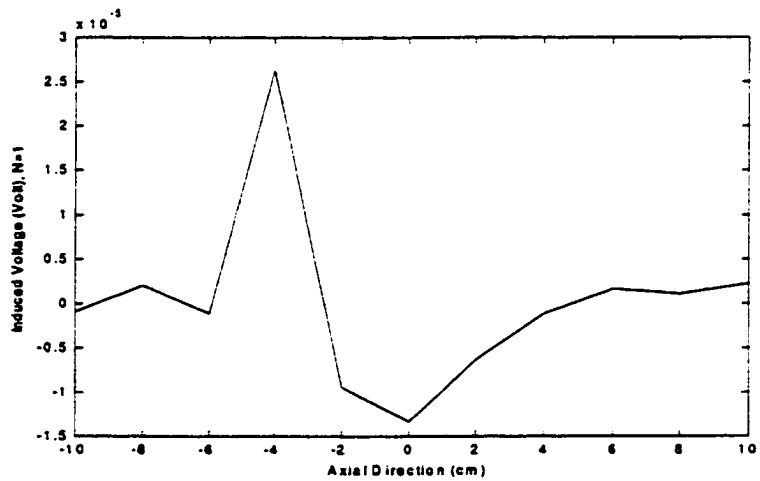


(b)

Figure 5.26. Case 3 (a) defect profile and (b) induced voltage signal



(a)



(b)

Figure 5.27. Case 4 (a) defect profile and (b) induced voltage signal

CHAPTER VI. CONCLUSIONS

This work was motivated by the need for finding an effective method for detecting axial cracks. Conventional MFL inspection tools generate axially oriented flux in the pipewall and hence can detect circumferential defects but are insensitive to axially oriented SCC. In this dissertation, the circumferential currents generated by the axial velocity of the magnetizer relative to the pipe are calculated. The circumferential currents are perturbed by the axial SCC. This dissertation investigates the feasibility of using fields associated with the perturbation currents for detection of SCC.

6.1. Summary of Accomplishments

The problem of modeling the overall current perturbation phenomena is decomposed into simpler tasks for the sake of computational feasibility. A four step procedure for modeling the interaction of axial SCC with circumferential currents has been developed. The overall problem is broken into four sequential tasks in order to simplify the model. The tasks involve the calculation of:

- (1) the velocity induced currents
- (2) current perturbation due to presence of SCC
- (3) the flux associated with the perturbation fields and the voltage induced by the perturbation current
- (4) Measurement of perturbation field using a coil

Numerical simulation of single and multiple SCC were performed. Parametric studies were done with respect to varying defect geometry. Double layer source model is utilized for the simulation of SCC colonies with arbitrary orientations. Results of numerical studies are very promising and indicate feasibility of the current perturbation method in detecting SCC. The signals predicted by the model are significant and should be measurable. Experimental validation of the method needs to be carried out. However, this requires the facility to run a pig at high velocities and the design of new sensors in the conventional pig. Besides investigating the feasibility of a new method for detecting axial SCC in the pipewall, the work developed in this dissertation also provides a potential method for modeling tight crack interaction with currents. The model can therefore be applied in modeling eddy current inspections of tight cracks.

6.2. Future Work

Apply the modeling procedure to eddy current NDE methods of a sample with tight crack (zero volume). One application is in the modeling of a crack under a fastener (CUFs) in the eddy current inspection of a aircraft part. The geometry is shown in figure 6.1. A small fatigue crack on the aluminum plate can develop after an extended period of service due to the numerous pressurization cycles. Cracks emanating from the fastener holes in the aircraft frames are a major source of failures and detecting of these cracks especially close to the fastener holes is very difficult.

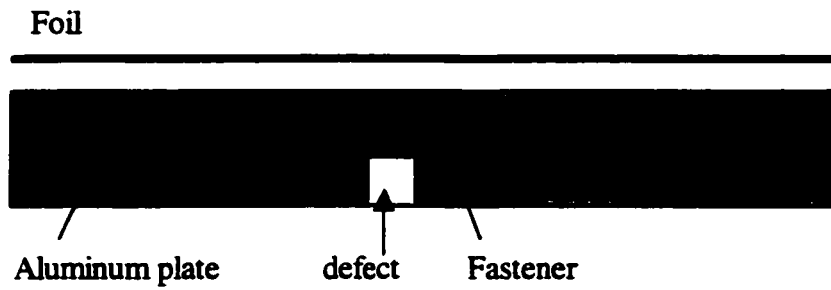


Figure 6.1. Defect under the fastener

The current perturbation method can be applied as follows. First, calculate the background current in the aluminum plate without defect and fastener by applying the current in the foil. Perturbation currents can be calculated by applying Neuman boundary conditions on the fastener and defect nodes. The resulting fields due to the perturbation currents can be calculated for further analysis.

APPENDIX. FINITE ELEMENT FORMULATION OF STEP 2

The governing equation of step 2 is

$$\nabla \cdot (\sigma \nabla V) = 0 \quad (\text{A.1})$$

The boundary problem is defined by the second order differential equation

$$\frac{\partial}{\partial x} \left(\sigma_x \frac{\partial V}{\partial x} \right) + \frac{\partial}{\partial y} \left(\sigma_y \frac{\partial V}{\partial y} \right) + \frac{\partial}{\partial z} \left(\sigma_z \frac{\partial V}{\partial z} \right) = f(x, y, z) \text{ on } \Omega \quad (\text{A.2})$$

where V is electric scalar potential. σ_x , σ_y , and σ_z are the conductivity. The boundary conditions are

$$V = p \text{ on } S_1 \quad (\text{A.3})$$

$$\left(\sigma_x \frac{\partial V}{\partial x} + \sigma_y \frac{\partial V}{\partial y} + \sigma_z \frac{\partial V}{\partial z} \right) \cdot \hat{n} + \gamma V = q \text{ on } S_2 \quad (\text{A.4})$$

where $S = S_1 + S_2$ denotes the surface enclosing the volume Ω as shown in figure A.1 and \hat{n} is its outward normal unit vector.

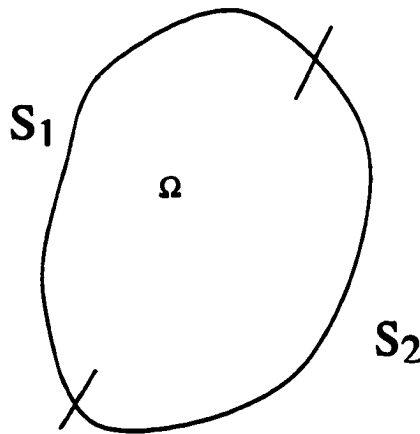


Figure A.1.

A.1. Domain Discretization and Shape Function

Let us consider eight nodes hexahedral element as shown in figure A.2. Here, each shape function N_i is one at node i and zero at other nodes of the elements. The shape function for the local coordinate system can be written as

$$N_1 = (1-\xi)(1-\eta)(1-\zeta)$$

$$N_2 = \xi(1-\eta)(1-\zeta)$$

$$N_3 = \xi\eta(1-\zeta)$$

$$N_4 = (1-\xi)\eta(1-\zeta)$$

(A.5)

$$N_5 = (1-\xi)(1-\eta)\zeta$$

$$N_6 = \xi(1-\eta)\zeta$$

$$N_7 = \xi\eta\zeta$$

$$N_8 = (1-\xi)\eta\zeta$$

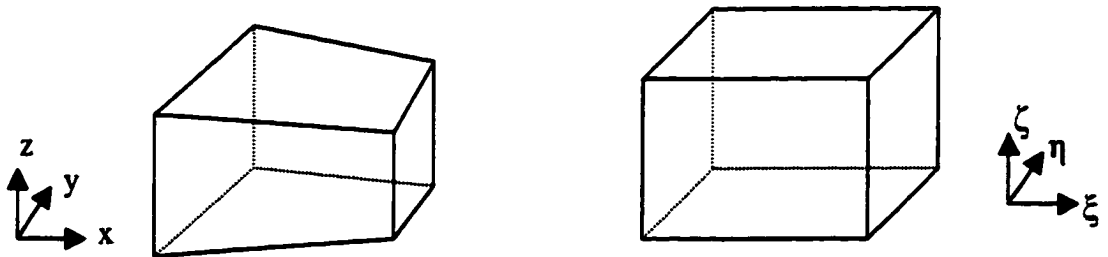


Figure A.2. Hexadral element in (a) xyz coordinate system and (b) local coordinate system

A.2. Evaluation of Elemental Matrices

The equivalent variational problem for the boundary value problem (A.2, A.3 and A.4) can be given as following

$$F(V) = \frac{1}{2} \iiint_{\Omega} \left[\sigma_x \left(\frac{\partial V}{\partial x} \right)^2 + \sigma_y \left(\frac{\partial V}{\partial y} \right)^2 + \sigma_z \left(\frac{\partial V}{\partial z} \right)^2 + 2fV \right] d\Omega + \iint_{S_2} \left(\frac{\gamma}{2} V^2 - qV \right) dS \quad (A.6)$$

The variational principle requires

$$\delta F(V) = 0 \quad (A.7)$$

Let the solution domain divide into M elements and each element has r node. The unknown field in each element can be expressed as

$$V^e = \sum_{i=1}^r N_i V_i = [N]^T [V^e] \quad (A.8)$$

where V_i is the nodal value of V at node i. Then the functional F(V) can be expressed as

$$F(V) = \sum_{e=1}^M F^e(V^e) \quad (A.9)$$

where

$$F^e(V^e) = \frac{1}{2} \iiint_{\Omega} \left[\sigma_x \left(\frac{\partial V^e}{\partial x} \right)^2 + \sigma_y \left(\frac{\partial V^e}{\partial y} \right)^2 + \sigma_z \left(\frac{\partial V^e}{\partial z} \right)^2 + 2fV \right] d\Omega + \iint_{S_2} \left(\frac{\gamma}{2} V^{e2} - qV^e \right) dS \quad (A.10)$$

Substitute (A.8) into (A.9) and taking the derivative of F^e with respect to V_i^e then we have

$$\begin{aligned} \frac{\partial F^e}{\partial V_i^e} &= \sum_{j=1}^r V_j^e \iiint_{\Omega} \left[\sigma_x \frac{\partial N_i^e}{\partial x} \frac{\partial N_j^e}{\partial x} + \sigma_y \frac{\partial N_i^e}{\partial y} \frac{\partial N_j^e}{\partial y} + \sigma_z \frac{\partial N_i^e}{\partial z} \frac{\partial N_j^e}{\partial z} \right] d\Omega + \iint_{\Omega} f N_i^e d\Omega \\ &+ \iint_{S_2} V_j^e [\gamma N_i^e N_j^e] dS - \iint_{S_2} q N_i^e dS \end{aligned} \quad (A.11)$$

This can be write in matrix form as

$$\frac{\partial F^e}{\partial V_i^e} = ([K^e] + [K_{S_z}^e])\{V^e\} - \{b^e\} \quad (A.12)$$

where

$$K_{ij}^e = \iiint_{\Omega} \left[\sigma_x \frac{\partial N_i^e}{\partial x} \frac{\partial N_j^e}{\partial x} + \sigma_y \frac{\partial N_i^e}{\partial y} \frac{\partial N_j^e}{\partial y} + \sigma_z \frac{\partial N_i^e}{\partial z} \frac{\partial N_j^e}{\partial z} \right] d\Omega \quad (A.13)$$

$$K_{S_z,ij}^e = \iint_{S_z} V_j^s [\gamma N_i^s N_j^s] dS \quad (A.14)$$

$$b_i^e = \iiint_{\Omega} f N_i^e d\Omega - \iint_{S_z} q N_i^s dS \quad (A.15)$$

The hexahedral element in the xyz coordinate system can be transformed into cubic element in the ξ, η, ζ coordinate system by following transform equation

$$\begin{aligned} x &= \sum_{i=1}^8 N_i(\xi, \eta, \zeta) x_i \\ y &= \sum_{i=1}^8 N_i(\xi, \eta, \zeta) y_i \\ z &= \sum_{i=1}^8 N_i(\xi, \eta, \zeta) z_i \end{aligned} \quad (A.16)$$

To perform the integration in the ξ, η, ζ system, all the integrands need to be converted in term of ξ, η and ζ . The derivative of shape function in the local coordinate system can be obtained by using chain rule

$$\begin{bmatrix} \frac{\partial N_i}{\partial \xi} \\ \frac{\partial N_i}{\partial \eta} \\ \frac{\partial N_i}{\partial \zeta} \end{bmatrix} = [J] \begin{bmatrix} \frac{\partial N_i}{\partial x} \\ \frac{\partial N_i}{\partial y} \\ \frac{\partial N_i}{\partial z} \end{bmatrix} \quad (\text{A.17})$$

where $[J]$ is Jacobian matrix as follow

$$[J] = \begin{bmatrix} \frac{\partial x}{\partial \xi} & \frac{\partial y}{\partial \xi} & \frac{\partial z}{\partial \xi} \\ \frac{\partial x}{\partial \eta} & \frac{\partial y}{\partial \eta} & \frac{\partial z}{\partial \eta} \\ \frac{\partial x}{\partial \zeta} & \frac{\partial y}{\partial \zeta} & \frac{\partial z}{\partial \zeta} \end{bmatrix} \quad (\text{A.18})$$

The derivative of shape function in xyz coordinate systems are

$$\begin{bmatrix} \frac{\partial N_i}{\partial x} \\ \frac{\partial N_i}{\partial y} \\ \frac{\partial N_i}{\partial z} \end{bmatrix} = [J]^{-1} \begin{bmatrix} \frac{\partial N_i}{\partial \xi} \\ \frac{\partial N_i}{\partial \eta} \\ \frac{\partial N_i}{\partial \zeta} \end{bmatrix} \quad (\text{A.19})$$

After calculate the Jacobian matrix, the derivative of shape function in the local coordinate system can easily be transformed to the global coordinate system. It can also be shown that the element of volume in the xyz coordinate system can be transformed into the ξ, η, ζ system as

$$d\Omega = dx dy dz = \det[J] d\xi d\eta d\zeta \quad (\text{A.20})$$

A.3. Implementation of Neuman Boundary Condition

The evaluation of A.13 is straightforward. However, evaluation of integral in A.14 and $\iint_{S_2} qN_i^s dS$ in A.15 is needed surface integral. The surface integral can be carried numerically on one of the hexahedral element plane ($\xi-\eta, \eta-\zeta$ or $\zeta-\xi$). If we choose $\xi-\eta$ plane as surface 1 then a surface integrals are

$$K_{S,ij}^e = \iint_{S_2} [\gamma N_i^s N_j^s] dS = \int \gamma N_i N_j |J| du dv \quad (A.21)$$

$$\iint_{S_2} q N_i^s dS = \int q N_i^s |J| du dv \quad (A.22)$$

where $i, j = 1, 2, \dots, 8$ and J is Jacobian Matrix

$$J = \begin{bmatrix} \frac{\partial \alpha}{\partial u} & \frac{\partial \beta}{\partial u} \\ \frac{\partial \alpha}{\partial v} & \frac{\partial \beta}{\partial v} \end{bmatrix} \quad (A.23)$$

where $\alpha - \beta$ represent for $x-y$, $y-z$ or $z-x$ and $u-v$ represent for $\xi-\eta$, $\eta-\zeta$ or $\zeta-\xi$. For a quadrilateral element in $\alpha - \beta$ space, the mapping from a unit square in $u-v$ space is given by

$$\alpha = \sum_{i=1}^4 N_i^{(2)} u_i \quad (A.24)$$

$$\beta = \sum_{i=1}^4 N_i^{(2)} v_i \quad (A.25)$$

where

$$N_1^{(2)} = (1-u)(1-v)$$

$$N_2^{(2)} = u(1-v)$$

$$N_3^{(2)} = uv \quad (\text{A.26})$$

$$N_4^{(2)} = (1-u)v$$

Consider the $\eta - \zeta$ plane of the hexahedral element as a surface 1 ($\xi = 0$). Then A.5 become

$$N_1 = (1-\eta)(1-\zeta)$$

$$N_2 = 0$$

$$N_3 = 0$$

$$N_4 = \eta(1-\zeta) \quad (\text{A.27})$$

$$N_5 = (1-\eta)\zeta$$

$$N_6 = (1-\eta)\zeta$$

$$N_7 = 0$$

$$N_8 = \eta\zeta$$

Thus surface 1 in $\alpha - \beta$ plane can be considered as a mapping from a unit square in $\eta - \zeta$ plane. From A.27, we see that N_1, N_4, N_5, N_8 are corresponds to $N_1^{(2)}, N_2^{(2)}, N_3^{(2)}, N_4^{(2)}$. The other surface integral can be evaluated in similar way.

For the step 2, $f(x,y,z)$ is zero

$$\frac{\partial}{\partial x} \left(\sigma_x \frac{\partial V}{\partial x} \right) + \frac{\partial}{\partial y} \left(\sigma_y \frac{\partial V}{\partial y} \right) + \frac{\partial}{\partial z} \left(\sigma_z \frac{\partial V}{\partial z} \right) = 0 \quad (\text{A.28})$$

The Neuman boundary condition is

$$\sigma \frac{\partial V}{\partial n} = -J \quad \text{on } S_2 \quad (\text{A.29})$$

which is

$$\sigma \nabla V \hat{n} + J = 0 \quad (\text{A.30})$$

Thus, the overall problem can be stated as

$$\frac{\partial}{\partial x} \left(\sigma_x \frac{\partial V}{\partial x} \right) + \frac{\partial}{\partial y} \left(\sigma_y \frac{\partial V}{\partial y} \right) + \frac{\partial}{\partial z} \left(\sigma_z \frac{\partial V}{\partial z} \right) = 0$$

$$V = p \quad \text{on } S_1$$

$$\sigma \nabla V \hat{n} + J = 0 \quad \text{on } S_2$$

BIBLIOGRAPHY

- [1] A.E. Crouch, "In-line inspection of natural gas pipelines," Topical Report, GRI, May 1993.
- [2] L. Udpa, S. Mandayam, S. Udpa, Y. Sun, and W. Lord, "Developments in gas pipeline technology," *Materials Evaluation*, Vol. 54, No. 4, April 1996, pp. 467-472.
- [3] A.E. Crouch, C.M. Teller, J.L. Fisher, and G. M. Light, "Assesment of technology for detection of stress corrosion cracking in gas pipelines," Topical Report, GRI, April 1994.
- [4] T.A. Bubenik, D.R. Stephens, B.N. Lies, and R.J. Eiber, " Stress corrosion cracks in pipelines: characteristics and detection considerations, " Topical Report, GRI, April 1995.
- [5] H.J. Bezer, "Magnetic methods of non-destructive testing," *British Journal of Non-Ddestructive Testing*, Vol. 6, no. 3, September 1964, pp. 85-93
- [6] J. F. Hinsley, *Non-destructive testing*, London, Macdonald & Evans, 1959.
- [7] W. Lord and D. J. Oswald, "Leakage field methods of defect detection," *International Journal of Nondestructive Testing*, Vol. 4, 1972, pp. 249-274
- [8] N. N. Zatsepin and V. E. Shcherbinin, "Calculation of the magnetostatic field of surface defects. I. Field topography of defect models," *Defectoscopyiya*, No. 5, September-October 1966, pp. 50-59
- [9] V. E. Shcherbinin and N. N. Zatsepin, "Calculation of the magnetostatic field of surface defects. II. Experimental verification of the principal theoretical relationships," *Defectoscopyiya*, No. 5, September-October 1966, pp. 59-65

- [10] V. E. Shcherbinin and A. I. Pashagin, "Polarization of cracks in nonuniformly magnetized parts," *Defectoscopya*, No. 3, May-June 1974, pp. 17-23
- [11] V. E. Shcherbinin and A. I. Pashagin, "On the volume polarization of cracks," *Defectoscopya*, No. 4, July-August 1974, pp. 106-110
- [12] J. H. Hwang and W. Lord, "Finite element modeling of magnetic field/defect interactions," *Journal of Testing and Evaluation*, Vol. 3, No. 1, January 1975, pp. 21-25
- [13] W. Lord and J. H. Hwang, "Defect characterization from magnetic leakage fields," *British Journal of NDT*, Vol. 30, January 1977, pp. 14-18
- [14] W. Lord, J. M. Bridges, W. Yen and R. Palanisamy, "Residual and active leakage fields around defects in ferromagnetic materials," *Material Evaluation*, Vol. 36, July 1978, pp. 47-54
- [15] G. Katragadda, "Application of state-of-art FEM techniques to magnetostatic NDE," Ph.D. Dissertation, Iowa State University, Ames, IA, 1995.
- [16] G. Kobidze, "Numerical modeling of tight (stress corrosion) cracks for the development of new electromagnetic NDT pipeline tools," Ph.D. Dissertation, Iowa State University, Ames, IA, 1998
- [17] R Gollamudi, "Rotating magnetic field technology for flaw detection in gas pipe lines," M.S.Thesis, Iowa State University, Ames, IA, 1998
- [18] Y. S. Sun, W. Lord, G. Katragadda and Y. K. Shin, "Motion induced remote field eddy current effect in a magnetostatic non-destructive testing tool: A finite element prediction," *IEEE Trans. Mag.*, Vol. 30, NO. 5, September 1994, pp. 3304-3307.
- [19] Y. K. Shin, "Numerical modeling of probe velocity effects for electromagnetic NDE," Ph.D. Dissertation, Iowa State University, Ames, IA, 1992

- [20] B. J. Mergelas and D. L. Atherton, "Discontinuity interaction and anomalous source models in through transmission eddy current testing," *Material Evaluation*, Vol. 54, January 1996, pp. 87-92
- [21] Z. Chen and K. Miya, "A new approach for optimal design of eddy current testing probes," *Journal of Nondestructive Evaluation*, Vol. 17, No. 3, 1998, pp. 105-116
- [22] Haoyu Huang, Toshiyuki Takagi, Hiroyuki Fukutomi and Junji Tani, "Forward and inverse analysis of ECT signals based on reduced vector potential method using a database," *Studies in Applied Electromagnetics and Mechanics*, Vol. 14, 1998, pp. 313-321
- [23] S. Niikuar and A. Kameari, "Analysis of eddy current and force in conductors with motion," *IEEE Trans. Mag.*, Vol. 28, No. 2, 1992, pp. 1450-1453
- [24] K. Muramatsu, T. Nakata, N. Takahashi and K. Fujiwara, "Comparison of coordinate systems for eddy current analysis in moving conductors," *IEEE Trans. Mag.* Vol. 28, No. 2, 1995. pp. 1186-1189
- [25] S. Y. Hahn, J. Bignon and J. C. Sabonnadiere, "An upwind finite element method for electromagnetic field problems in moving media," *International Journal for Numerical Methods in Engineering*, Vol. 24, 1987
- [26] Y. Jizo, T. Yamada and M. Iwamoto, "Analysis of lift and drag forces in electromagnetic levitation system," *Trans. IEE of Japan*, Vol. 97-B, No. 4, 1977, pp. 215-222
- [27] J. Donea, "A Taylor-Galerkin method for convective transport problems," *International Journal of Numerical Methods in Engineering*, Vol. 20, 1984, pp. 101-119

- [28] O. C. Zienkiewicz, R. Loehner, Kmorgan and S. Nakazawa, "Finite elements in fluid mechanics – a decade of progress," *Finite Elements in Fluids*, Vol. 5, 1984, pp. 1-26
- [29] H. M. Lesimann and E. O. Friend, " A Symmetric- Matrix Time Integration Scheme for the Efficient Solution of Advection-Dispersion Problems," *Water Resource Research*, Vol. 25,pp. 1133-1139, 1989
- [30] Young-Kil Shin, Yushi Sun and W. Lord, "Numerical techniques for solving magnetostatic problems involving motion and nonuniform geometry," *IEEE Trans. Mag.*, Vol. 33, NO. 2,1997, pp. 1161-1166
- [31] P.b. Zhou, Numerical Analysis of Electromagnetic Fields, Springer-Verlag
- [32] Z.Q. You, Z.W. Jiang, Y.S. Sun and L. Udpa, "Application of the substructure-frontal method for repeated solution of large sparse matrix equation to field problems," *IEEE Trans. Mag.*, Vol. 24, NO. 1, January 1988, pp. 326-329
- [33] Y.S. Sun, G.S. Zhang and W. Chen, "A data base method for 3-D open boundary field computation," *IEEE Trans. Mag.*, Vol. 26, NO. 2, March 1990, pp. 807-811
- [34] Pin Tong, John N. Rossettos, Finite element method, Basic technique and implementation, The MIT press, 1977

ACKNOWLEDGMENTS

I would like to express my sincere appreciation to the following people who encouraged me with continual enthusiasm to complete this study.

I would like to express my sincere gratitude to my co-major professors, Dr. Lalita Udpa and Dr. William Lord, for introducing me to the world of numerical modeling and for providing me the opportunity to perform research and pursue my Ph.D at ISU. Their continuous encouragement, patience, moral and financial support, were of great help to me during my research.

I would like to thank Dr. Yushi Sun, from whom I have acquired all my knowledge of numerical modeling. I am grateful to him for his guidance and invaluable help during this research. I would also like to thank Dr. Satish Udpa for his valuable discussions and help.

I owe much thanks to Dr. Paul Sacks and Dr. Julie Dickerson for being the committee members of my program and for their advice.

Finally, I would like to thank my family. I am deeply obligated to my beloved parents for their unconditional love and encouragement. To my wife, Sunja, and son, Jungwook, I owe special thanks for their love and support.